

1 **Supplementary Information**

2

3 ***Homo sapiens* in Arabia by 85,000 years ago**

4

5 Huw S. Groucutt^{1,2*}, Rainer Grün^{3,4}, Iyad S.A. Zalmout⁵, Nick A. Drake⁶, Simon J.
6 Armitage^{7,8}, Ian Candy⁷, Richard Clark-Wilson⁷, Julien Louys³, Paul S. Breeze⁶, Mathieu
7 Duval^{3,9}, Laura T. Buck^{10,11}, Tracy L. Kivell^{12,13}, Emma Pomeroy^{10,14}, Nicholas B. Stephens¹³,
8 Jay T. Stock^{10,15}, Mathew Stewart¹⁶, Gilbert J. Price¹⁷, Leslie Kinsley⁴, Wing Wai Sung¹⁸,
9 Abdullah Alsharekh¹⁹, Abdulaziz Al-Omari²⁰, Muhammad Zahir²¹, Abdullah M. Memesh⁵,
10 Ammar J. Abdulshakoor⁵, Abdu M. Al-Masari⁵, Ahmed A. Bahameem⁵, Khaled S.M. Al
11 Murayyi²⁰, Badr Zahrani²⁰, Eleanor M.L. Scerri^{1,2} & Michael D. Petraglia^{2,22*}

12

13 ¹ School of Archaeology, Research Laboratory for Archaeology and the History of Art, Hayes House,
14 75 George Street, University of Oxford, Oxford, OX1 2BQ, UK.

15 ² Department of Archaeology, Max Planck Institute for the Science of Human History, Kahlaische
16 Stasse 10, D-07743, Jena, Germany.

17 ³ Australian Research Centre for Human Evolution (ARCHE), Environmental Futures Research
18 Institute, Griffith University, Nathan, QLD 4111, Australia.

19 ⁴ Research School of Earth Sciences, The Australian National University, Canberra ACT, 0200,
20 Australia.

21 ⁵ Saudi Geological Survey, Sedimentary Rocks and Palaeontology Department, Jeddah 21514, Saudi
22 Arabia.

23 ⁶ Department of Geography, King's College London, Strand, London WC2R 2LS, UK

24 ⁷ Department of Geography, Royal Holloway, University of London, TW20 0EX UK

25 ⁸ SFF Centre for Early Sapiens Behaviour (SapienCE), University of Bergen, Post Box 7805, 5020,
26 Bergen, Norway.

27 ⁹ Geochronology, Centro Nacional de Investigación sobre la Evolución (CENIEH), Paseo Sierra de
28 Atapuerca, 3, 09002 Burgos, Spain

29 ¹⁰ PAVE Research Group, Dept. of Archaeology, University of Cambridge, Cambridge, CB2 3QG,
30 UK.

31 ¹¹ Earth Sciences Department, Natural History Museum, Cromwell Road, London, SW7 5BD, UK.

32 ¹² Skeletal Biology Research Centre, School of Anthropology and Conservation, University of Kent,
33 Canterbury, CT2 7NR, UK.

34 ¹³ Department of Human Evolution, Max Planck Institute for Evolutionary Anthropology, Deutscher
35 Platz 6, 04103, Leipzig, Germany.

36 ¹⁴ School of Natural Sciences and Psychology, Liverpool John Moores University, Liverpool, L3 3AF,
37 UK.

38 ¹⁵ Department of Anthropology, University of Western Ontario, London, Ontario, N6A 3K7, Canada.

39 ¹⁶ Palaeontology, Geobiology and Earth Archives Research Centre, School of Biological, Earth and
40 Environmental Science, University of New South Wales, Sydney 2052, Australia.

41 ¹⁷ School of Earth and Environmental Sciences, The University of Queensland, St Lucia 4072,
42 Queensland, Australia.

43 ¹⁸ Department of Life Sciences, The Natural History Museum, Cromwell Road, London SW7 5BD,
44 UK.

45 ¹⁹ Department of Archaeology, King Saud University, Riyadh, 12372 Saudi Arabia.

46 ²⁰ Saudi Commission for Tourism and National Heritage, Riyadh 11586, Saudi Arabia.

47 ²¹ Department of Archaeology, Hazara University, Mansehra, 21300, Pakistan.

48 ²² Human Origins Program, National Museum of Natural History, Smithsonian Institution,
49 Washington, DC, 20560, USA.

50

51 Corresponding authors: HSG (huw.groucutt@rlaha.ox.ac.uk) and MDP (petraglia@shh.mpg.de)

52 **SI 1. Description and comparison of the of Al Wusta-1 phalanx.**

53

54 **1.1 Pathology**

55

56 The Al Wusta-1 (AW-1) phalanx shows evidence of pathological changes to the bone
57 surface. Additional pathological bone formation affects the proximal half of the shaft,
58 covering approximately one quarter of the dorsal surface, measuring 11.9 mm proximo-
59 distally and 5.9 mm radio-ulnarly, and projecting approximately 2.5 mm from inferred
60 'normal' bone surface. Micro-CT scanning confirms that the additional bone is continuous
61 with the cortical bone of the shaft, but there is no evidence of a fracture or other trauma (Fig.
62 2B, C). Its irregular, angular morphology suggests that this additional bone may be due to the
63 ossification of the central slip of the extensor digitorum muscle (i.e., a "bony spur" or
64 enthesophyte), which attaches to the intermediate phalanx in this region. The unusual,
65 relatively circular cross-sectional shape of AW-1 may also reflect these pathological changes.

66

67 **1.2 Linear metric analysis of the Al Wusta-1 intermediate phalanx**

68

69 Linear measurements of AW-1 are presented in Supplementary Table 1. We conducted an
70 analysis of nine linear measurements of intermediate phalanx shape across a sample of extant
71 primates and fossil hominins (Supplementary Table S2). For extant non-human primates,
72 intermediate phalanges (IPs) from all rays (2-5) of one side (either left or right) were included
73 as it is possible that all non-human primate IPs may show similar morphology to human
74 IPs^{1,2}. However, human and fossil hominin IPs from the fifth ray (IP5) show a distinctive,
75 asymmetrical shape that is not present in AW-1 and thus all *H. sapiens* IP5 specimens and
76 potential IP5 fossil hominin specimens were excluded from the analysis. Although data from

77 multiple IPs from a single individual are not independent, without knowing the exact ray to
78 which AW-1 belongs, nor the exact ray or number of individuals associated with several of
79 the comparative fossil hominin intermediate phalanges, it is more conservative to include the
80 range of morphological variation across multiple rays.

81

82 Linear measurements included the maximum proximo-distal length of the phalanx (i.e. total
83 length), maximum dorso-palmar height of the proximal base, the dorso-palmar height and
84 radio-ulnar breadth of the proximal articular facet, radio-ulnar breadth of the proximal shaft,
85 and dorso-palmar height and radio-ulnar breadth of the midshaft and distal shaft, all of which
86 could be confidently measured on AW-1.

87

88 All metrics were assessed and compared as a ratio of the total length of the phalanx.

89 Comparisons across extant taxa, Neandertals and *H. sapiens* (i.e. all taxonomic groups with
90 large enough sample sizes) were evaluated using Mann-Whitney U pairwise comparisons
91 with a Bonferroni correction for multiple comparisons (Supplementary Table 3). Relative
92 comparisons of AW-1 and other fossil specimens were visually assessed via box-and-whisker
93 plots (Supplementary Figure 1).

94

95 Comparative analyses reveal that there is substantial overlap across most taxa in all shape
96 ratios. For any given shape ratio, AW-1 falls within the range of variation of cercopiths,
97 *Gorilla*, *A. afarensis*, *A. sediba*, Neanderthals and *H. sapiens*. However, AW-1 is most
98 similar to the median value or falls within the range of variation of recent and early *H.*
99 *sapiens* for all shape ratios (Supplementary Figure 1), confirming its affiliation with *H.*
100 *sapiens* revealed by the 3D geometric morphometric analyses (see main text and below).
101 More specifically, AW-1 is very similar to the *H. sapiens* median value in the relative

102 radioulnar breadth of the proximal base and the proximal shaft, and the dorso-palmar height
103 at midshaft. AW-1 falls within the lower range of variation of *H. sapiens*, and outside or at
104 the extreme of the Neanderthal range of variation, in its dorso-palmar height and radioulnar
105 breadth proximal facet, and its radioulnar breadth at midshaft and the distal shaft.

106

107 Note that published values for the controversial *H. sapiens* specimen Cueva Victoria CV-0
108 specimen are included in the proximal base breadth and midshaft breadth and height shape
109 ratios (Supplementary Figure 1). This specimen is always the most extreme outlier in the
110 box-and-whisker plots, and falls in the direction of the cercopithecoid median value,
111 suggesting that this specimen is indeed that of *Theropithecus*, and not *H. sapiens*, supporting
112 Martínez-Navarro and colleagues^{1,2}.

113

114 **1.3 Geometric morphometric comparison of non-human primate, fossil hominin and AI** 115 **Wusta-1 phalanges**

116

117 To provide a broader interpretive context for AW-1, we provide a principal components
118 analysis of geometric morphometric landmark data (Supplementary Table 4, Supplementary
119 Figure 2) on a sample of phalanges from a range of primates including fossil hominins
120 (Supplementary Table 5). In Figure 3 (main text) and Supplementary Figure 3, PC1 and PC2
121 together account for 61% of group variance in shape. AW-1 is separated on these two shape
122 vectors from the non-human primates and most of the Neanderthals by a shorter, wider
123 diaphysis and palmarly flatter proximal base. It shares a proximal head that is higher to the
124 right (dorsal view) with *H. sapiens*, although this may be a function of the proportion of left
125 and right sides in each sample. AW-1 falls closest to the Holocene and early *H. sapiens* and is
126 well differentiated from all non-human primates. This is shown by the Procrustes distances

127 from AW-1 to the mean shapes of each taxonomic group (Figure 3, Supplementary Figure 3
128 and Supplementary Table 6).

129

130 **1.4 Geometric morphometric analysis restricted to AW-1 and hominin phalanges of** 131 **known side and digit numbers**

132

133

134 Details of the sample are given in Supplementary Table 7. Methods and Results for pooled
135 left and right hands are given in the main text (see Figure 4 and also Supplementary Tables 8-
136 9.)

137

138 **1.4.1 Left and right 2nd, 3rd and 4th intermediate phalanges separated.**

139

140 The results showing AW-1 compared separately to right and to left phalanges
141 (Supplementary Figure 4, Supplementary Tables 10-11) are very similar to the pooled sample
142 (see main text, Figure 4 and Supplementary Tables 8-9), such that AW-1 is closest to
143 Holocene *H. sapiens* 3rd rays for both right and left hand, although Pleistocene *H. sapiens*
144 configurations fall almost completely inside the scatter for the Holocene *H. sapiens* sample.
145 AW-1 is most distinct from the Neanderthal phalanges of both the left and right hands. The
146 greatest separation between AW-1 and other groups is described by PC2 for both the right
147 and left phalanges. These vectors describe the shape difference between shorter and stockier
148 vs. longer and narrower configurations. AW-1 is taller and narrower (in all directions: dorso-
149 palmarly, proximo-distally and radio-ulnarly) than shapes towards the other end of the PC2s,
150 which describe most of the Neanderthal phalanges. Again, these analyses suggest that AW-1
151 is likely to be a 3rd intermediate phalanx from a *H. sapiens* individual.

152

153 **1.5 Cross sectional geometry analyses**

154

155 **1.5.1 Materials and Methods**

156

157 Cross-sectional geometry (CSG) of bones examines the amount and distribution of cortical
158 bone in the cross section, which reflects primarily the impacts of body size, body shape, and
159 activity on the skeleton³⁻⁶. CSG of AW-1 and the comparative 2nd-4th phalanges
160 (Supplementary Table S7) were calculated in ImageJ⁷ using the BoneJ plugin⁸ and using the
161 same microCT data as for the GMM analyses. Slices at 54% of total AW-1 phalanx length
162 (measured from the proximal end) were analysed to avoid the influence on cross-sectional
163 properties of the pathological bone formation on the shaft. Total area (TA) of the cross
164 section was calculated by filling the medullary cavity with the 'fill holes' function of ImageJ
165 and rerunning the slice through BoneJ. Percent cortical area (%CA) reflecting cortical bone
166 thickness was calculated as $100 * \text{cortical area} / \text{TA}$. J , a measure of torsional and twice
167 average bending rigidity, was calculated as the sum of maximum and minimum bending
168 rigidities (I_{max} and I_{min} respectively)⁹.

169

170 GMM analyses suggest that AW-1 is a 3rd intermediate phalanx, but plots were generated for
171 each of manual rays 2-4 in case these analyses suggested otherwise. Where left and right
172 sides were present for the same ray of the same individual, the mean was used.

173

174 As body size and activity are both important determinants of bone cross-sectional properties
175 (see above), CA and J were plotted against bone length to examine whether the cross-
176 sectional properties relative to body size could differentiate Neanderthal, Pleistocene *H.*
177 *sapiens* and Holocene *H. sapiens* and thus be informative regarding the taxonomic affiliation

178 of AW-1. However, it must be noted that CSG of the phalanges, unlike the limb long bones^{4,8},
179 is not well documented in the literature and the relative importance of body size, activity and
180 taxonomy remain to be investigated in detail. The relationship between I_{max} and I_{min} , which
181 reflects the circularity of bone distribution was also examined by plotting I_{max} against I_{min} .
182 Plots were generated using IBM SPSS Statistics v. 23.

183

184

185 **1.5.2 Results**

186

187 In general, AW-1 lies outside of the range of CSG for intermediate phalanges from ray 2,
188 well within the range for ray 3, and at the upper end of the range for ray 4 (Supplementary
189 Figure 5), supporting the interpretation that AW-1 is most likely to be a 3rd intermediate
190 phalanx. For all cross-sectional properties, Holocene *H. sapiens* show a large range of
191 variation and the small sample of Neanderthals and Pleistocene *H. sapiens* do not appear well
192 differentiated from the Holocene specimens. While generally within the range of the
193 comparative specimens, AW-1 falls just outside the range of the sample for I_{max} relative to
194 I_{min} , with a low ratio indicating an unusually circular cross-section. In the long bones of the
195 lower limb, more circular shafts indicate similar loading in multiple directions¹⁰⁻¹¹, but its
196 precise interpretation for manual phalanges remains to be explored.

197

198 Further work to document the range of variation in phalanx CSG and its relationship to
199 ancestry and behaviour patterns would be required to further interpret the cross-sectional
200 circularity of the AW-1. A relationship between this high level of circularity and the
201 pathological bone formation on the dorsal surface of AW-1's shaft cannot be excluded, since
202 the shaft could be expanded in a dorso-palmar direction even where external appearance is

203 normal, which would serve to lower the I_{max}/I_{min} ratio. Alternatively, a generally high level of
204 loading might account for both the enthesophyte and more circular cross-section of the shaft.

205

206

207

208

209

210

211

212

213

214

215

216

217

218

219

220

221

222

223

224

225

226

227 **SI 2. U-series and combined US-ESR dating of fossil bone and teeth from**
228 **Al Wusta.**

229

230 **2.1 Materials and Methods**

231 **2.1.1 Material**

232 The human phalanx (AW-1, lab code for U-series = 3675) and a hippopotamus tooth
233 fragment (lab code WU1601) were collected from Trench 1. The external dose rate
234 calculations are based on the data from OSL sample PD40 (Supplementary Table 16), which
235 was collected at the equivalent position within unit 3a.

236

237 **2.1.2 U-series analysis**

238 U-series analysis of bones can be used to reconstruct U-uptake phases. Modern bones are
239 virtually U free. All the uranium that is measured in fossil samples migrated into the skeletal
240 tissues after these were buried. However, it is difficult to establish whether this U-uptake was
241 a single stage process that occurred a short time after burial, or whether the U-accumulation
242 was a complex, multistage process that may have commenced a significant time after the
243 original burial¹². In any case, as long as there is no indication for uranium leaching, the
244 calculated U-series age results have to be regarded as minimum age estimates with respect to
245 the age of the fossil.

246

247 The experimental setup for the U-series analysis of the AW-1 phalanx was previously
248 described in Grün and colleagues¹². Laser ablation (LA) was used to drill a number of holes
249 the finger bone following the approach of Benson et al.¹³. After a cleaning run with the laser

250 set at a diameter of 460 μm , seven holes were drilled for 1000 s (Supplementary Figure 6A)
251 with the laser set at 330 μm . The isotopic data streams (Supplementary Figure 6B) were
252 converted into $^{230}\text{Th}/^{234}\text{U}$ and $^{234}\text{U}/^{238}\text{U}$ activity ratios and apparent Th/U age estimates
253 (Supplementary Figure 6C) and subsequently binned into 30 successive sections (each
254 containing 33 cycles) for the calculation of average isotopic ratios and ages (Supplementary
255 Figure 6D; Supplementary Table 12).

256

257 A similar experimental setup and methodology were employed for the LA U-series analysis
258 of tooth sample WU1601 (Supplementary Figure 8). Individual closed system U-series age
259 estimates were calculated for each ablation spot and the whole analytical data of the enamel
260 and dentine sections were integrated to provide the data input for the ESR age calculations
261 (Supplementary Table 13).

262

263 **2.1.3 ESR dose evaluation**

264

265 Enamel was collected from tooth WU1601 and powdered $<200\ \mu\text{m}$. The sample was then
266 divided into 11 aliquots and gamma irradiated with a Gammacell-1000 Cs-137 source to the
267 following doses: 0, 49, 97, 146, 243, 340, 486, 873, 1457, 2430 and 3397 Gy. ESR
268 measurements were carried out at room temperature with an EMXmicro 6/1 Bruker ESR
269 spectrometer coupled to a standard rectangular ER 4102ST cavity. The following procedure
270 was used to minimise the analytical uncertainties: (i) all aliquots of a given sample were
271 carefully weighed into their corresponding tubes and a variation of $<1\ \text{mg}$ was tolerated from
272 one aliquot to another; (ii) ESR measurements were performed using a Teflon sample tube
273 holder inserted from the bottom of the cavity to ensure that the vertical position of the tubes

274 remains exactly the same for all aliquots. The following acquisition parameters were used: 3-
275 30 scans (depending on the sample and aliquot measured), 1 mW microwave power, 1024
276 points resolution, 15 mT sweep width, 100 kHz modulation frequency, 0.1 mT modulation
277 amplitude, 20 ms conversion time and 5 ms time constant.

278

279 ESR intensities were extracted from T1-B2 peak-to-peak amplitudes of the ESR signal of
280 enamel¹⁴, and then corrected by the corresponding number of scans and aliquot mass. Fitting
281 procedures were carried out with the Microcal OriginPro 9.5 software using a Levenberg-
282 Marquardt algorithm by chi-square minimization. D_E values were obtained by fitting a single
283 saturating exponential (SSE) function through the experimental data, with data weighting by
284 the inverse of the squared ESR intensity $(1/I^2)^{15}$.

285

286 The sample was measured three times on different days in order to evaluate the precision in
287 measurement and D_E . Only small variation of between 1.5% and 2.7% ($1-\sigma$) were found over
288 the three days, respectively. The final D_E value was calculated by pooling all the ESR
289 intensities derived from the three repeated measurements in a single dose response curve
290 (DRC)¹⁶. In order to avoid D_E overestimation caused by the use of the SSE function, an
291 appropriate maximum irradiation dose (D_{max}) was selected in accordance with the
292 recommendations by Duval and Grün¹⁷: given the magnitude of the D_E value (~ 100 Gy),
293 D_{max}/D_E should be between 5 and 10, and final dose evaluation were thus done with $D_{max}=873$
294 Gy ($D_{max}/D_E=9$). The final DRC is shown in Supplementary Figure 9.

295

296 **2.1.4 Dose rate evaluation and US-ESR age calculation**

297 For the dose rate calculations, the following parameters were used: an alpha efficiency of
298 0.13 ± 0.02^{18} , Monte-Carlo beta attenuation factors¹⁹, recently published dose-rate conversion
299 factors²⁰. For the calculation of the external sediment dose rate, the data of OSL sample PD40
300 (Supplementary Table 16) were used. The total external dose rate of $438 \pm 27 \mu\text{Gy/a}$ consists
301 of $254 \pm 25 \mu\text{Gy/a}$ cosmic dose rate (for the actual depth of 25 cm below surface), 180 ± 10
302 $\mu\text{Gy/a}$ external gamma dose rate, plus the external beta dose rate was corrected for the tooth
303 configuration, resulting in $4 \mu\text{Gy/a}$.

304

305 Combined US-ESR ages were calculated with DATA²¹ using the US model defined by Grün
306 et al²². Further details about this dating method applied to fossil teeth may be found in
307 Duval²³. The other details of the age result of $103 \pm 10 / -9 \text{ ka}$ are shown in Supplementary
308 Table 14.

309

310 **2.2 Results and discussion**

311

312 **2.2.1 U-series dating of the Al Wusta-1 phalanx**

313

314 Some scans show elevated ²³²Th levels (see Supplementary Figure 6B, around cycle 250),
315 which is the result of probing some pores that may be filled with detrital material. However,
316 all ²³⁸U/²³²Th elemental ratios are well above 50. Supplementary Figure 6E shows that the
317 calculated ages of the cycles with lower U/Th ratios are not affected by detrital ²³⁰Th, which
318 would systematically increase the results.

319 All age calculations are based on closed system assumptions, they are thus apparent age
320 estimates. U/Th ages were calculated using the Isoplot 3.75 Excel add-on²⁴. Note that this
321 program does not calculate asymmetric errors. All reported errors are 2- σ . We did not use the
322 diffusion-adsorption decay (DAD) model of Sambridge and colleagues²⁵ as there is evidence
323 of at least two discrete U-uptake phases.

324

325 All data steams have in common that the outer domains yield younger lower apparent ages
326 than those further inside the bone (Supplementary Figure 7A). This is clearly associated with
327 higher U concentrations (Supplementary Figure 7B and C). This indicates a second discrete
328 phase of U-accumulation, which overprinted the original isotopic signature. The more U was
329 taken up at that later phase, the younger becomes the apparent U-series age. For each of the
330 holes, the apparent age plateaus after an initial increase. These age plateaux systematically
331 increase from Hole 1 to Hole 7 (see Supplementary Figure 7A). Interestingly, there is a
332 reverse trend with older plateau ages associated with slightly higher U-concentrations
333 (Supplementary Figure 7D). This is could be related to a process where the domains, which
334 had accumulated more U during an initial uptake phase, were relatively less affected by any
335 subsequent U-migration processes.

336

337 To conclude, the age plateaux of hole #7 of 87.6 ± 2.5 ka represents the minimum age of the
338 finger bone. The true age of the bone may be older because (i), the age plateaux of holes #1
339 to 6 are affected by later U-uptake phases, and it is not possible to ascertain whether the age
340 plateau of hole #7 was not affected; (ii), the observed, complex U-migration processes may
341 have commenced a considerable time after the initial burial.

342

343 **2.2.2 Combined US-ESR dating of the fossil tooth**

344

345 Apparent U-series age results obtained for the dental tissues are close to those obtained in the
346 human phalanx: 83.5 ± 8.1 ka in the enamel and 65.0 ± 2.1 ka in dentine. These results suggest
347 that the tooth sample is at least 83 ka old.

348

349 The combined US-ESR age calculation yields a result of 103^{+10}_{-96} ka. This ESR result
350 agrees with OSL sample PD40 (98.6 ± 7 ka) within error.

351

352

353

354

355

356

357

358

359

360

361

362

363

364

365

366

367 **SI 3: Optically stimulated luminescence (OSL) dating of Al Wusta**

368

369 **3.1 Sample collection and preparation**

370

371 Trenches were dug through the marl beds into the underlying aeolian sand (Unit 1) at Al
372 Wusta. Three samples (PD15, PD17 and PD41, Supplementary Figure 13) were collected
373 from Unit 1 sands underlying the southern marl outcrop, upon which the AW-1 phalanx and
374 the majority of the animal fossils were found. A fourth sample (PD40, Supplementary Figure
375 13) was taken from Unit 3. PD40 and PD41 were taken from the same trench. OSL samples
376 were collected by hammering opaque tubes into cleaned section faces. In the laboratory,
377 quartz was extracted from the portion of each sample which had not been exposed to
378 sunlight. Samples were initially wet-sieved to isolate the 212-180 μm size fraction, and
379 carbonates and organic matter were subsequently removed using 1M HCl and H_2O_2
380 respectively. The samples were then re-sieved at 180 μm and quartz was extracted from the
381 $>180 \mu\text{m}$ fraction using density separations at 2.62 and 2.70 g/cm^3 and a subsequent HF acid
382 etch (23M HF for 60 min followed by a 10M HCl rinse). Since Nefud quartz samples are
383 prone to feldspar contamination, an additional one week H_2SiF_6 treatment followed by an
384 HCl rinse was also performed. Etched samples were re-sieved at 150 μm , to remove partially
385 dissolved grains, and stored in opaque containers prior to measurement.

386

387 **3.2 Luminescence measurements**

388

389 **3.2.1 Equipment**

390 All OSL measurements presented here were carried out using a Risø TL/OSL-DA-15
391 automated dating system²⁶, fitted with a single-grain OSL attachment^{27,28}. Optical stimulation

392 of single-grains used a 10 mW Nd: YVO₄ solid-state diode-pumped green laser (532 nm)
393 focussed to yield a nominal power density of 50 W/cm², following²⁶. All infra-red (IR)
394 stimulation was carried out using an IR (870 nm) laser diode array yielding a power density
395 of 132 mW/cm². OSL passed through 7.5 mm of Hoya U-340 filter and was detected using an
396 Electron Tubes Ltd 9235QB15 photomultiplier tube. Irradiation was carried out using a 40
397 mCi ⁹⁰Sr/⁹⁰Y beta source giving ~6 Gy/min. This source is calibrated relative to the National
398 Physical Laboratory, Teddington ⁶⁰Co γ -source (Hotspot 800²⁹). Due to the spatial
399 inhomogeneity of beta emitters across the active face of our ⁹⁰Sr/⁹⁰Y beta source, it was
400 necessary to calibrate the dose rate to each individual grain position on a single-grain disc³⁰
401 using the method of Armitage and colleagues³¹.

402

403 **3.2.2 Single-grain measurement and analysis**

404

405 Measurements were made on 2800-3600 individual quartz grains per sample (Supplementary
406 Table 15), using the single-aliquot regenerative-dose (SAR) method³², to estimate the
407 equivalent dose (D_e). Since optimum measurement conditions vary between samples^{32,33},
408 single-grain dose recovery tests^{34,35} were performed on two of the four samples (PD15 and
409 PD17) using a known dose of ~50 Gy. A preheating regime of 260 °C held for 10 seconds
410 prior to measurement of the natural/regenerated dose, and 220 °C held for 10 seconds prior to
411 measurement of the test dose, yielded dose recovery ratios (measured dose/known dose) of
412 1.01 ± 0.03 for both samples and was adopted for subsequent D_e measurements. Optical
413 stimulation was carried out at 125 °C for 2 s using the green laser. The OSL signal was that
414 recorded during the first 0.3 s of stimulation, with a background signal from the last 0.3 s of
415 stimulation subtracted^{36,37}. Dose response curves were fitted with a saturating exponential or a
416 saturating-exponential-plus-linear function. The standard error associated with each

417 individual D_e determination was estimated by Monte Carlo simulation. Curve fitting, D_e
418 determination and Monte Carlo simulation were performed using version 4.31.9 of the
419 Luminescence Analyst software³⁸.

420

421 It has been observed widely that the majority of quartz grains from unheated sedimentary
422 deposits do not yield a measureable OSL signal³⁹⁻⁴¹ or display luminescence characteristics
423 which indicate that they are unsuitable for age determination. Consequently, single-grain
424 dating studies must adopt criteria for rejecting uninformative grains⁴⁰. In this study, grains
425 were rejected where one or more of the following conditions are met: (1) the OSL signal
426 from the grain is too low to distinguish it from the variability in the background signal,
427 determined using the “Tn signal more than 3 sigma above BG” rejection criterion in
428 Luminescence Analyst³⁸; (2) the recycling ratio⁴² differs from unity by greater than two
429 standard errors; (3) the IR-depletion ratio¹⁷ is greater than two standard errors below unity;
430 (4) recuperation exceeds 5% of the natural signal and (5) the sensitivity-corrected natural
431 luminescence intensity is greater than the saturation intensity of the measured growth curve
432 (termed “oversaturation” in Supplementary Table 15). In addition, grains were rejected where
433 their measured D_e was within measurement uncertainty of 0 Gy at 2σ . This last criterion
434 excludes intruded modern grains, and has been found necessary for the analysis of samples
435 from similar contexts elsewhere in the Nefud Desert⁴³. These rejection criteria were applied
436 in order, and only the first cause of rejection is recorded in Supplementary Table 15. Of the
437 17,900 grains measured, only 265 displayed acceptable luminescence properties, a yield of
438 1.5%. The majority of grains (94%) were rejected due to low OSL signal intensity. Despite
439 rigorous attempts to remove feldspar from the quartz fraction, fewer grains were accepted
440 than failed the IR-depletion ratio criterion. This phenomenon has been observed in other
441 single-grain studies on Nefud “quartz” e.g Petraglia and colleagues⁴³.

442

443 To determine the age of a sample from a single-grain dataset it is necessary to calculate a
444 single value for the burial dose (D_b). Since the OSL samples presented here were taken from
445 aeolian sand where complete resetting of the OSL signal prior to deposition may be assumed,
446 and the small number of intruded grains were rejected prior to analysis, D_b was calculated for
447 all samples using the central age model (CAM)⁴⁴. Overdispersion (OD) values for the Al
448 Wusta samples ranged from $16 \pm 3\%$ to $26 \pm 3\%$ (PD17 and PD40 respectively), which is
449 consistent with values reported from well-bleached undisturbed sediments^{33,45,46}, supporting
450 the use of the CAM to derive estimates of D_b . Equivalent dose distributions for each sample
451 are presented in Supplementary Figure 10.

452

453 **3.3 Environmental dose rate calculations**

454 For HF acid etched sand-sized quartz grains, the environmental dose rate consists of external
455 beta, gamma and cosmic ray components. Beta dose rates were measured using a Risø GM-
456 25-5 low-level beta counting system⁴⁷ using MgO and Volkagem loess⁴⁸ standards, while
457 gamma dose rates were measured using an EG&G Ortec digiDart-LF gamma-spectrometer
458 using the “threshold” method. Dose rates were corrected for the effects of HF etching⁴⁹, grain
459 size⁵⁰ and a water content of $5 \pm 2.5\%$. The 2σ uncertainty on water content encompasses
460 completely dry conditions (0%) and saturation for 25% of the burial period (10%),
461 representing the full range of reasonable mean water content scenarios of a freely draining
462 aeolian sand. Cosmic ray dose rates were calculated using site location (27.4°N, 39.4°E, 925
463 m elevation) and present day sediment burial depths⁵¹. For samples other than PD40, the
464 overburden was assumed to consist of 40 cm of sand (the target sampling depth below the
465 base of the marl) containing 5% water by mass (assumed bulk density 1.74 g/cm^3), with the
466 remainder of the overburden depth being carbonates also containing 5% water by mass

467 (measured bulk density 1.36 g/cm^3). For PD40, the entire overburden was assumed to be sand
468 with an assumed bulk density of 1.74 g/cm^3 . Using these assumptions, cosmic rays contribute
469 between 33 % (PD15) and 44% (PD40) of the total calculated dose rate, meaning that
470 accurate estimation of the cosmic ray dose rate is more important for these samples than is
471 normally the case. Therefore, the assumptions regarding burial depth require detailed
472 consideration. Firstly, it was assumed that Unit 2 was deposited instantaneously above PD15-
473 17 and PD41, while the full depth of Unit 3a was deposited instantaneously above PD40.
474 This assumption allows the cosmic dose rate to be regarded as constant throughout the
475 sample's burial period. For Unit 2, this assumption must approximate reality since the OSL
476 ages for samples below Unit 2 are indistinguishable from those above. For unit 3 geologically
477 instantaneous deposition cannot be demonstrated, but seems likely based on the interpretation
478 that this deposit represents the encroachment of fluvial sedimentation during the final drying
479 of Al Wusta lake (SI Section 5). Uncertainties on the cosmic ray dose rate were set at $\pm 10\%$.
480 Assuming that the overlying sediments were deposited rapidly, mean overburden during a
481 sample's burial period is unlikely to have been lower than that in the present day.
482 Consequently, cosmic ray dose rates calculated as described above are either accurate or
483 overestimates of mean burial dose rates. Cosmic ray dose rate overestimation will occur
484 where appreciable reduction in the depth of overlying sediments has occurred since burial. In
485 the case of samples overlain by carbonate beds (all except PD40), the cohesive nature of
486 these sediments suggests that limited removal of overlying carbonates has occurred since
487 burial. Conversely, the coarse surface lag (Unit 3b) above Unit 3a (Sample PD40) suggests
488 that some overburden loss due to deflation has occurred (SI Section 5). It is difficult to
489 estimate the quantity of material lost due to this process, but the sensitivity of the true cosmic
490 ray dose rate to deflation may be estimated. In the present case, the lower (-10%) boundary of
491 the estimated cosmic ray dose rate would be achieved by adding ~40 cm of sand (bulk

492 density 1.74 g/cm³) to the burial depth of the shallow samples (PD17 and 40), or ~70 cm to
493 the burial depth of the deeper samples (PD15, 16, 41). However, this calculation represents
494 the worst-case scenario, since it implies greater overburden throughout the burial period,
495 followed by instantaneous removal of ~40/~70 cm of sand immediately prior to sampling. If
496 a more realistic model, assuming continuous deflation throughout the burial period is used,
497 then the lower boundary of the estimated cosmic ray dose rate is achieved after removal of 80
498 cm of sand overlying the shallow samples, and 140 cm of sand overlying deeper samples.
499 These considerations suggest that the ±10% (1σ) uncertainties assumed for our cosmic ray
500 dose rates encompass reasonable variations in overburden density over time.

501

502 Dose rates and sample ages are presented in Supplementary tables 16 and 17 respectively. All
503 analyses were carried out in the Royal Holloway Luminescence Laboratory by SA and R C-
504 W.

505

506

507

508

509

510

511

512

513

514

515

516

517 **SI 4 Site chronology and Bayesian model**

518 The combination of different numerical dating methods enables us to provide ages for AW-1
519 and associated sediment and fossils. The chronostratigraphic evidence available may be
520 summarized as follows (Supplementary Figures 11 and 12):

- 521 - The human phalanx was found on the surface of Trench 1, on an exposure of Unit 3b.
522 Direct U-series dating of AW-1 itself provides an age of 87.6 ± 2.5 ka (2σ confidence
523 level). This result should be regarded as a minimum age for the fossil.
- 524 - A hippopotamus tooth (WU1601) was collected from Trench 1 within Unit 3a, one
525 metre away from AW-1 (Supplementary Figure 14). U-series dating of the dental
526 tissues provides apparent ages of 83.5 ± 8.1 ka (enamel) and 65.0 ± 2.1 ka (dentine)
527 (2σ). These minimum age results are consistent with that obtained for AW-1,
528 suggesting that both fossils are coeval.
- 529 - Combined US-ESR dating of WU1601 yields an age of $103^{+10/-9}$ ka (1σ), indicating
530 a relatively early uranium uptake in dental tissues ($p=-0.83$ and -0.53 for enamel and
531 dentine, respectively). This age estimate is compatible with the minimum age results
532 derived from U-series dating of AW-1 and WU1601.
- 533 - The OSL sample collected from PD40 section within the same Unit 3a provides an age
534 of 98.6 ± 7.0 ka (PD40). This estimate is consistent with the US-ESR age obtained for
535 WU-1601 and the minimum age of ~ 88 ka obtained for AW-1.
- 536 - Three OSL samples collected from Unit 1 provides ages of 85.3 ± 5.6 ka (PD17), 92.2
537 ± 6.8 ka (PD41) and 92.0 ± 6.3 ka (PD15). These ages are internally consistent and a
538 weighted mean age of 89.3 ± 3.6 ka may be derived. Because Unit 1 is stratigraphically
539 located below Unit 3a, these results provide a maximum possible age for Unit 3 and the
540 associated fossils.

541 The combination of these data suggests a 2σ time interval of 85.1 to 96.5 ka for AW-1 (86.5-
542 92.9 ka at 1σ) based on the minimum and maximum age constraints derived from the direct U-
543 series age ($87.6-2.5 = 85.1$ ka) and the weighted mean OSL age of Unit 1 ($89.3+7.2=96.5$ ka).
544 This age range agrees well with the US-ESR age result obtained for WU1601 collected close
545 to AW-1 (Supplementary Figure 14).

546

547 In order to further constrain the chronology of the deposits, all these data were incorporated
548 into a Bayesian sequential phase model with phase 1 (underlying aeolian sand) corresponding
549 to Unit 1 and Phase 2 (lake phase) to both Units 2 (no samples dated) and 3. We have not
550 excluded shared systematic uncertainties (e.g. uncertainties shared between OSL ages) from
551 the uncertainty term on individual ages. The exclusion of shared systematic uncertainties may
552 be appropriate where: 1) a number of age estimates for a single event are being combined (e.g.
553 10 OSL ages for a single stratum) or 2) where the principal aim is to determine the duration of
554 time represented in a phase of activity/deposition. However, we use the Bayesian sequential
555 phase model to determine the timing of deposition of the AW1 specimen. Here the uncertainties
556 on individual ages (whether shared or not) do represent the uncertainty on the timing (but not,
557 in the case of shared uncertainties, the duration) of deposition. With this type of model
558 removing systematic uncertainties would give a false sense of precision to the depositional age
559 for AW1. Modelled ages indicate that deposition of Unit 1 ceased 93.1 ± 2.6 ka (Phase 1, PD15,
560 17, 41) and that Units 2 and 3 and all associated fossils were deposited between 92.2 ± 2.6 ka
561 and 90.4 ± 3.9 ka (Phase 2, all other ages). The end date for phase 2 should be treated as a
562 maximum value since no overlying material is present, precluding the possibility of further
563 constraining the end of this phase. The timing of the lake phase is earlier than that indicated by
564 other humidity records from the region. Given that the three samples from sands underlying
565 the lake (arid phase indicators) are internally consistent, and coincide with the MIS 5c

566 insolation minimum, we propose that the subsequent lake phase correlates with the
567 strengthened summer monsoon associated with the insolation peak at 84 ka (Fig. 6).

568

569

570

571

572

573

574

575

576

577

578

579

580

581

582

583

584

585

586

587

588

589

590

591 The code used to produce the Bayesian sequence model is as follows:

```
592 Plot()
593 {
594   Sequence()
595   {
596     Boundary("Start 1");
597     Phase("1")
598     {
599       Date("PD41",N(calBP(92200),6800))
600       {
601       };
602       Date("PD17",N(calBP(85300),5600))
603       {
604       };
605       Date("PD15",N(calBP(92000),6300))
606       {
607       };
608     };
609     Boundary("End of sand");
610     Boundary("Start of lake");
611     Phase("2")
612     {
613       Date("PD40",N(calBP(98600),7000))
614       {
615       };
616       Before("i")
617       {
618         Date("AW-1",N(calBP(87600),1250))
619         {
620         };
621       };
622       Before("ii")
623       {
624         Date("Hippo enamel",N(calBP(83500),4050))
625         {
626         };
627       };
628       Before("iii")
629       {
630         Date("Hippo dentine",N(calBP(65000),1050))
631         {
632         };
633       };
634       Date("US-ESR",N(calBP(103000),10000))
635       {
636       };
637     };
638     Boundary("End of lake");
639   };
640 };
641
```

642

643 **SI 5. Stratigraphy, sedimentology and palaeoecology**

644

645 **5.1 Results**

646 **5.1.1 Sedimentology**

647

648 Unit 1 consists of loose, cross-bedded medium to coarse sands that contain evidence for
649 bioturbation and iron-staining, this deposit underlies the sequence across the whole Al Wusta
650 site (Supplementary Figures 13 and 14). The carbonate beds (Unit 2) exposed at Al Wusta are
651 structureless and homogeneous, with some evidence for weak, horizontal laminations in
652 PD16 sediments at depths between 70-40 cm. Carbonate content is high throughout all three
653 sequences (typically >50%, Supplementary Figure 13), but the sediments have a low density
654 typical of diatomite when dry. Shell fragments are rare but are present in the base of PD15
655 and PD16 and towards the top of PD16. These fragments are obvious in thin section but not
656 in hand specimen and any picked remains could not be identified to specific taxa. During
657 sieving of samples for isotopic analysis the coarse residue, >63 μ m, was examined and
658 ostracod fossils were not observable. XRD whole rock analysis (that characterises the
659 mineralogy of crystalline mineral composition, and consequently will not identify organics
660 and non-crystalline biominerals, i.e. diatoms), indicate that the samples are dominated by
661 calcite (>90%) with minor amounts of quartz (Supplementary Table 18 and Supplementary
662 Figure15). Peaks that are attributable to evaporitic minerals such as gypsum and halite are
663 present but the peak heights are so small that they are indistinguishable from background
664 noise. Unit 3a consists of medium sands that are weakly horizontally laminated and contain
665 fragments of eroded marls, occasional clasts and shells (*Melanoides tuberculata* and
666 *Planorbis* sp). The upper part of Unit 3 (Unit 3b) is effectively desert pavement and has been

667 formed by the aeolian deflation of Unit 3a, concentrating clasts, shells, lithic and fossils at the
668 land surface. The upper parts of Unit 3a contain calcite-cemented rhizolith that, as a result of
669 progressive sediment deflation, now occur at the land surface as a cemented cap.

670

671 **5.1.2 Micromorphology**

672

673 All samples are dominated by homogeneous microsparite with some local zones of spar and
674 micrite (Supplementary Figure 16a). Most sediments are massive with no clear sedimentary
675 structures except for the sediments in PD16 (40-70 cm) which show evidence for finely
676 laminated calcite, with laminations reflecting alternations between fine-grained micrite,
677 coarser microspar and organics (Supplementary Figure 16b). Towards the top of PD17
678 laminations of allogenic quartz grains occur but these are infrequent (30-40 cm). Where
679 quartz grains occur, their surfaces show signs of etching and replacement with calcite.

680

681 Organic remains are present in either an amorphous form or showing clear signs of cellular
682 preservation. Diatoms and sponge spicules are visible in many slides (Supplementary Figure
683 16c) and the latter are typically most abundant at the sample levels with the lowest %
684 carbonate values. Iron staining occurs towards the top of PD15 (40-50 cm) and towards the
685 base of PD16 (0-10 cm). There is no evidence for neomorphism and negligible evidence for
686 pore-infilling of secondary cement.

687

688 **5.1.3 $\delta^{18}\text{O}$ and $\delta^{13}\text{C}$ analysis**

689

690 The $\delta^{18}\text{O}$ and $\delta^{13}\text{C}$ values of the sub-samples from the four sampling locations (PD15, 16, 17
691 and 40) are shown in Supplementary Figure 17 Data from all four sections show very similar

692 $\delta^{18}\text{O}$ values), although there is a significant scatter in each dataset. Greater variation occurs
693 within the mean $\delta^{13}\text{C}$ values, although the standard deviations of each dataset are again large.
694 Although the dataset from each sampling locality is small PD15 (n = 8), PD 16 (n = 15),
695 PD17 (n = 7) and PD40 (n = 12) it is sufficient to show the following patterns: 1) there is no
696 co-variance in $\delta^{18}\text{O}$ and $\delta^{13}\text{C}$ values at any site or within the whole dataset level (r^2 ca 0.2)
697 and 2) there is no consistent pattern of variation upwards through the profiles. With regard to
698 the second point, while there is a clear trend at site PD40 of increasingly positive values
699 upwards through the profile the reverse is true of PD16. Interpretation of these conflicting
700 signals is problematic because it is unclear whether the deposits in each sequence are
701 absolutely contemporaneous. One sample of calcite rhizolith was analysed from the calcrete
702 capping PD40. This sample has the highest $\delta^{18}\text{O}$ value of the dataset, but it is the $\delta^{13}\text{C}$ value
703 that is most significant as the high value (-1.12‰) implies that the vegetation that became
704 established after the lake basin infilled/desiccated was a C4 grassland.

705

706 **5.1.4 Diatoms**

707

708 The diatom flora at PD15 and PD16 are shown in Supplementary Figures 18 and 19. Both
709 sites show very similar species assemblages. The diagrams are divided into statistically
710 significant zones based on a comparison with the broken-stick model using the program
711 BSTICK version 1⁵². The species diagrams of each site can be divided into three statistically
712 significant zones, the main characteristics of which are outlined below, along with the main
713 environmental implications of these assemblages:

714

715 **PD15**

716 Zone I

717 This zone comprises planktonic species (*Lindavia rossi*, *Cyclotella krammeri* and *Lindavia*
718 *ocellata*) which is illustrated by the high planktonic: benthic ratio. The CA and DCCA axis 1
719 scores decrease slightly in this zone. The log concentration, however, increases in this section
720 meanwhile there is a minor decrease in the F index.

721

722 Zone II

723 This section reflects a change in species from mainly planktonic taxa to an increase in benthic
724 taxa (*Cymbella affinis* and *Nitzschia angustata*) and periphytic (*Staurosirella lapponica* and
725 *Ulnaria ulna* (agg.)). The increase in benthic and periphytic taxa is notable in the habitat
726 composition diagram. The CA and DCCA axis 1 sample scores both decline considerably.
727 There is also a decrease in the log concentration and the F index remains low.

728

729 Zone III

730 *Aulacoseira italica* and *Aulacoseira granulata* are the dominant taxa of this zone. The sample
731 at 40 cm does not contain any benthic taxa therefore the planktonic: benthic ratio cannot be
732 calculated for this level which is reflected in the habitat composition diagram. There is an
733 increase in the CA axis 1 sample scores meanwhile a decrease in the DCCA axis 1 sample
734 scores and log concentration occurs. The F index, which is a dissolution index, shows that the
735 level of preservation is high for this sample in comparison to the rest of the profile.

736

737 pH

738 The assemblage reflects increasing pH as *Lindavia ocellata* usually occurs in mesotrophic
739 lakes⁵³, whereas *Staurosirella lapponica*, *Stephanodiscus hantzschii*, *Aulacoseira granulata*
740 and *Aulacoseira italica* are indicative of eutrophic lakes^{54,55}. *Staurosirella lapponica* and

741 *Stephanodiscus hantzschii* are good indicators of high alkalinity lakes meanwhile
742 *Aulacoseira granulata* and *Aulacoseira italica* are characteristic of carbonate rich lakes.

743

744 **Lake depth**

745

746 The planktonic: benthic ratio and the habitat summary show that zone I is the deepest as
747 planktonic (e.g. *Lindavia rossi* and *Cyclotella krammeri*) and tychoplanktonic (e.g. *Lindavia*
748 *ocellata*) taxa increase to reach a peak at 0cm^{56,57}. The proportion of periphytic taxa increases
749 throughout the zone II meanwhile benthic (e.g. *Cymbella affinis* and *Nitzschia angustata*)
750 taxa reach a peak at 20 cm suggesting a decline in water depth which remains low for the
751 remainder of the sequence. *Aulacoseira italica* and *Aulacoseira granulata*, which are
752 periphytic and planktonic taxa respectively, dominate in zone III. *Aulacoseira granulata*
753 suggests that lake levels were quite shallow⁵⁸ up to a few metres and quite turbulent^{55,59}.
754 *Aulacoseira italica* accounts for 65% of the assemblage at 40 cm also suggesting shallower
755 conditions as the habitat summary shows that this level comprises of periphytic and
756 planktonic taxa with a small proportion of taxa with unknown ecology.

757

758 **Salinity**

759 There are very few saline tolerant species except for *Epithemia argus* which can be found in
760 harsh conditions from saline to high alkaline, nutrient poor conditions. Due to its low
761 abundance and the lack of other saline species salinity is not a major driver of this
762 assemblage.

763

764 **Phosphorous**

765 The taxa (*Lindavia rossi*, *Cyclotella krammeri* and *Cyclotella ocellata*) show increasing
766 nutrient enrichment from a mesotrophic lake, which suggests moderate phosphorous
767 concentration to eutrophic conditions with high phosphorous concentrations characterised by
768 *Stephanodiscus hantzschii*, *Aulacoseira granulata* and *Aulacoseira italica*⁵⁶⁻⁵⁹.

769

770 **PD16**

771 Zone I

772 *Stephanodiscus* and *Aulacoseira* are the dominant taxa in this zone with small increases in
773 *Fragilaria delicatissima*, *Staurosirella lapponica* and *Cymbella affinis*. There is an increase
774 in the planktonic: benthic ratio at the 10 cm which remains stable until zone II. The PCA and
775 DCCA axis 1 scores diverge at 0 cm; however, both show little change meanwhile the log
776 concentration and the F Index both increase until 10 cm before decreasing.

777

778 Zone II

779 There is a large decline in *Aulacoseira italica* in this section, while a decrease in the
780 periphytic taxa occurs with a contemporaneous increase in benthic taxa. The PCA axis 1
781 scores remain stable; meanwhile there is an increase in the DCCA axis 1 sample scores,
782 fluctuations in the log concentration and an increase in preservation in this zone.

783

784 Zone III

785 *Lindavia rossi*, *Cyclotella krammeri* and *Lindavia ocellata* are the predominant taxa of this
786 zone; however, *Aulacoseira italica* and *Lindavia ocellata* are the main taxa at 70 cm. The
787 reduced abundance of benthic taxa is reflected by the increased planktonic: benthic ratio. The
788 PCA and DCCA axis 1 sample scores also illustrate the change in composition. The log
789 concentration and F Index both follow the same trend and decrease overall in this section.

790 **pH**

791

792 The assemblage shows generally declining pH from *Stephanodiscus hantzschii*,
793 *Stephanodiscus parvus*, *Aulacoseira angustata*, *Staurosirella lapponica*, *Aulacoseira italica*,
794 *Cymbella affinis*, *Lindavia ocellata*, *Cyclotella krammeri* and *Lindavia rossi*. The interaction
795 of other variables, for examples, depth, light and phosphorous can also affect the abundance
796 of different taxa^{56,61}. The taxa present in zones I and II are associated with higher pH
797 consistent with lower water levels which can concentrates the pH. In zone III the taxa
798 changes and reflects lower pH conditions coherent with higher water levels which dilutes the
799 pH level and other nutrients^{62,63}.

800

801 **Lake depth**

802 The planktonic: benthic ratio and habitat summary shows that zone I and II consists of mainly
803 benthic taxa and periphytic taxa suggesting lower water levels. Zone III comprises of mostly
804 planktonic and tychoplanktonic species, indicating higher water levels. The PCA and DCCA
805 axis 1 sample scores both show a big change in the composition and, over time, of the
806 assemblage, reflecting the change in water level.

807

808 **Salinity**

809 *Epithemia argus* is the only saline species present in the diagram which indicates that
810 assemblage is not significantly influenced by salinity.

811

812 *Phosphorous*

813 The response to nutrient enrichment, which is usually linked to phosphorous, follows the
814 same trend as pH of decreasing nutrient status as reflected by the declining nutrient tolerant

815 taxa. Nutrient cycling within the lake is also affected by other variables (e.g. depth, light and
816 pH) thus in zones I and II where there is lower water depth the phosphorous concentration
817 increases enabling *Stephanodiscus hantzschii* and *Aulacoseira granulata* to thrive.
818 Conversely in Zone III the assemblage consists of species with a low threshold for
819 phosphorous which suggests a higher water level as the phosphorous becomes more
820 dilute^{62,63}.

821

822 The overall change in the diatom assemblages can be assessed by the changes in the species
823 composition of the sample (PCA or CA) and over time between the samples (DCCA). CA
824 was used in PD15 which shows that there are substantial changes from 20 cm to the top of
825 the core as the exploratory DCA axis 1 gradient length was ≥ 1.5 SD units. The DCCA also
826 shows a corresponding high species turnover which suggests a large change in species
827 composition between samples which the decrease in the planktonic:benthic ratio reflects.
828 PCA was used in PD16 (gradient length of exploratory DCA was ≤ 1.5 SD units) that shows
829 there are smaller species compositional changes within this site than PD15. The largest
830 change occurs between 40-50 cm at PD15 which is simultaneous with a change in taxa
831 reflected by the sudden increase in the DCCA axis 1 sample scores and the planktonic:
832 benthic ratio. Although the changes appear larger in PD15 there are caveats to consider; the
833 small sample size of 5 samples at this site may not be as representative of the environment as
834 a larger dataset so the results may change if more samples were analysed at more frequent
835 intervals. The planktonic:benthic ratio of PD15 is smaller than that of PD16 suggesting less
836 fluctuation in the water level.

837

838 **5.2 Interpretation**

839

840 The proxy data outlined above allows the environment and hydrology of the Al Wusta lake
841 beds to be reconstructed. This has implications for both the environment of the site itself but
842 also for the regional palaeoclimate of the time.

843

844 **5.2.1 Environment and hydrology of the Al Wusta lake beds**

845

846 The loose and cross-bedded nature of the sands of Unit 1 are typical of aeolian dune sands
847 and indicate that, prior to carbonate accumulation, the Al Wusta site was affected by active
848 dune migration. Unit 2, characterised by massive carbonate beds and their microfabrics, is
849 typical of the accumulation of authigenic carbonate marl on the bed of a lacustrine
850 environment^{64,65}. The precipitation of carbonate in the water column and its deposition out of
851 suspension leads to the development of fine-grain marl beds. The structureless character of
852 the beds is indicative of shallow water resulting in the sediment being oxidised and
853 consequently bioturbated, or exposed to water column turbulence by surface winds. The
854 preservation of laminations within PD16 most probably relates to short-term episodes of
855 deeper water or more rapid rates of sedimentation. Despite being shallow there is no
856 sedimentary evidence to indicate that the lacustrine environment underwent desiccation, as
857 there is a complete absence of surface exposure features, and the character of the sediments
858 are consistent throughout the entirety of the bed⁶⁴. The shallow nature of the water is
859 supported by the diatom assemblage which contains significant proportions of *Aulacoseira*
860 *italica* and *Aulacoseira granulata* which indicates a few metres of water depth, with the latter
861 being indicative of turbulent water conditions. While changes in the planktonic/benthic ratio
862 of the diatom assemblage suggest progressive changes in water level there is no evidence to
863 indicate that the water level dropped to sub-aerially expose the lake beds. Consequently, the
864 beds record the existence of a perennial water body.

865

866 The diatom flora is dominated by freshwater species with negligible evidence for salinity
867 tolerant species. The lake was, therefore, a freshwater environment; an interpretation
868 supported by the dominance of calcite in the lake XRD mineralogy traces and an absence of
869 evaporitic minerals such as halite and gypsum.

870

871 A lack of covariance in $\delta^{18}\text{O}$ and $\delta^{13}\text{C}$ values is often used to indicate whether a lake basin
872 was part of an open system (i.e. a system with an active inflow and outflow to the basin) or
873 not. Generally, the absence of co-variance is indicative of open-system lake waters that are
874 regularly recharged; this has the effect of limiting any in-basin modification of the isotopic
875 signal by processes such as evaporation⁶⁶. Such a scenario could be true of the Al Wusta lake
876 beds as the persistence of freshwater conditions (as evidenced by the diatom assemblages)
877 and the lack of evaporative minerals would indicate that this system never underwent
878 sufficient evaporation to produce brackish or saline conditions. However, two points are
879 important to consider here. Firstly, a number of studies exist that report closed lake systems
880 that do not show co-variance in their isotopic signals⁶⁷. The exact cause of this is not always
881 clear, however, it highlights the fact that the absence of $\delta^{18}\text{O}$ and $\delta^{13}\text{C}$ co-variance at Al
882 Wusta should not be used as definitive evidence of this site recording an open lake system.
883 Secondly, it is important to acknowledge that, even when there is no isotopic covariance, the
884 $\delta^{18}\text{O}$ of the water in open system lakes can still become enriched as a result of the
885 evaporation of surface waters. However, as such systems have regular recharge this does not
886 result in the waters becoming brackish or saline⁶⁸. This is an important point as it is
887 impossible to say whether minor or major evaporative enrichment in lake $\delta^{18}\text{O}$ water values
888 occurred at Al Wusta, but the diatom and mineralogical evidence shows that if such
889 evaporation did occur, it was not sufficient to cause the waters to become brackish.

890

891 In summary, the proxy evidence indicates that Unit 2 represents the deposition of marl in a
892 perennial water body that was entirely fresh. At this time the Al Wusta lake basin was an
893 accessible and permanent freshwater resource for any early humans in the region. The pattern
894 in the $\delta^{18}\text{O}$ values seen at site PD40 (an increase in $\delta^{18}\text{O}$ values upward through the
895 sequence) could reflect a trend to greater aridity during the accumulation of this sequence
896 (with increasing values reflecting greater evaporation and hence greater aridity). However, as
897 the reverse is true for PD16 it is difficult to know how robust this interpretation is.

898

899 The mean $\delta^{18}\text{O}$ values of this sequence (-2.4 to -1.9‰) reflect both the $\delta^{18}\text{O}$ value of the lake
900 water and the temperature at which carbonate precipitation occurred⁶⁶. Both of these are
901 unknown, however, the nearest local isotopic dataset indicates that modern rainfall has a $\delta^{18}\text{O}$
902 value of -4.0 to -4.5‰⁶⁹. If such values occurred at the time of marl development at Al Wusta
903 then it is likely that either the temperature of mineralisation was surprisingly low (i.e. a
904 carbonate with a mean $\delta^{18}\text{O}$ value of -2.2‰ precipitating from water with a mean $\delta^{18}\text{O}$ value
905 of -4.25‰ would form in isotopic equilibrium at a temperature of ca 11°C) or that significant
906 isotopic enrichment, through evaporation, of the lake water had occurred. It is also important
907 to consider, however, that the modern climate system that generates rainfall with a value of -
908 4.0 to -4.5‰ is a function of a westerly dominated system. As most humid phases in the
909 Arabian Peninsula are suggested to relate to increased monsoon strength⁷⁰, it is likely that the
910 $\delta^{18}\text{O}$ value of the rainfall during the formation of the lake system at Al Wusta was
911 significantly different, and most likely heavier, than modern day values. A strong south to
912 north gradient in the $\delta^{18}\text{O}$ value of modern rainfall appears to exist in Arabia in the present
913 day, with values in the southern part of this region being >0‰ in contrast with those in the
914 north that are around 4‰⁷¹. Only a small northward shift in the air masses bringing rainfall

915 from a southerly source would, therefore, produce a significant increase in the $\delta^{18}\text{O}$ value of
916 rainfall at Al Wusta.

917

918 Consequently, it is currently unclear whether the marl $\delta^{18}\text{O}$ value of ca -2.2‰ is a function of
919 low water temperatures, isotopic enrichment, different air mass trajectory or a combination of
920 all of these factors. Although many of the artefacts and fossils are found within Unit 3 it is
921 important to stress that *in situ* artefacts are found with Unit 2 implying that humans were
922 present in the landscape during the existence of the perennial freshwater lake body.

923

924 The deposits of Unit 3a are interpreted as waterlain sands based on the presence of freshwater
925 molluscs, the horizontal laminations and the incorporation of ripped up fragments of the
926 underlying marl. The sands are interpreted as reflecting the encroachment of fluvial
927 sedimentation during the final phase of basin infilling, either as a result of desiccation or
928 simply due to the progressive reduction in available accommodation space. It is considered
929 that the former is more likely as the inclusion of ripped up marl fragments would imply that
930 the upper surface of Unit 2 had dried out and fragmented prior to the deposition of Unit 3a.

931 The waterlain sands are capped by a horizon of calcified rhizoliths that represent the final
932 transition from sub-aqueous to terrestrial conditions at the site. The coarse surface lag (Unit
933 3b) reflects the winnowing of Unit 3a by aeolian processes and the formation of a desert
934 pavement. The relatively resistant nature of the rhizolith horizon makes this layer resistant to
935 aeolian erosion resulting in the occurrence of these features as a cemented cap at the top of
936 the sequence.

937

938 The majority of the excavated Al Wusta artefacts and fossils are found in Unit 3a. As the
939 sediments of this unit contain evidence of eroded and reworked marl from Unit 2 it is

940 possible that the archaeological and faunal material has been derived from Unit 2 and
941 reworked into the fluvial sands. If this is the case then it supports the idea that human
942 occupation at the site is associated with the existence of a perennial, freshwater lake. If the
943 artefacts and fossils are *in situ* then it implies that occupation of the site must have persisted
944 after the contraction of the lake basin and the desiccation of the water body.

945

946 **5.2.2. Implications of the Al Wusta sequence for regional palaeoclimate**

947

948 The proxy record of the Al Wusta sequence records the existence of a perennial, freshwater
949 lake system. Regarding human migration into this region, it is important to establish whether
950 the existence of such a system can be explained by local hydrogeology or by increased
951 regional moisture (i.e. the occurrence of a humid phase). It is argued here, despite evidence
952 from only a single site being presented, that an increase in mean annual precipitation is
953 required to explain the development of the Al Wusta lake basin. This suggestion is based
954 upon three main observations. Firstly, the fact that Unit 2 comprises well-developed marl
955 beds means that the lake waters must have been fed by groundwater recharge. The presence
956 of sufficient dissolved Ca^{2+} in the lake waters to produce extensive marl precipitation requires
957 migration of the waters through an aquifer. While much of the underlying geology is quartz
958 rich sands, these are interbedded with units of carbonate rich marls that reflect phases of lake
959 activity that pre-date the formation of the Al Wusta sequence. It is likely that these beds are
960 the source of the dissolved minerals that fed into the Al Wusta basin. Secondly, no
961 groundwater fed lake systems currently exist in the Nefud as the water table is too low.
962 Surface water bodies are, therefore, restricted to highly ephemeral recharge playas. Thirdly,
963 the underlying sediments and bedrock in this region are highly permeable aeolian sands; no
964 local impermeable strata exist that could generate a locally perched water table that would

965 explain the existence of a lake system at this site. It is, therefore, proposed that the genesis of
966 a groundwater fed lake system at this locality requires a regional increase in mean annual
967 rainfall and the persistence of a humid phase in the Nefud Desert.

968

969 **5.2.3 Summary**

970 The Al Wusta sequence records the evolution of the site across an entire humid phase from
971 aeolian deposition (Unit 1) to the development of lacustrine conditions (Unit 2) to the
972 progressive drying out of the lake basin and the reversion to terrestrial conditions (Units 3a
973 and b). In particular, the diverse range of proxies discussed here indicate that the Unit 2
974 carbonate deposits at Al Wusta were deposited in a perennial shallow (a few metres of water
975 depth) alkaline lake environment. This lake water body formed as a result of a humid phase
976 and was fresh throughout its existence, making it a major resource for humans and fauna
977 during this interval.

978

979

980

981

982

983

984

985

986

987

988

989

990 **SI 6. Al Wusta vertebrate palaeontology, biogeography and taphonomy.**

991

992 The Al Wusta vertebrate fossil assemblage (Supplementary Table 19; Supplementary Figure
993 19) is very fragmented, with few complete bones recovered. Fossil weathering is extensive
994 and much of the cortical surfaces of the bones are missing, making skeletal element and
995 taxonomic identification difficult. Of the 860 specimens, 305 are identifiable to skeletal
996 element, with long bone shafts most common (Supplementary Table 20). Of the 12 distinct
997 taxa identified, medium-sized bovids are most abundant, followed by small-sized bovids and
998 *Hippopotamus*. *Hippopotamus* is represented solely by incisor and tusk fragments recovered
999 *in situ*. *Kobus* sp. is represented by partial right M₂ and M₃ teeth (Supplementary Figure 20).
1000 The M₃ has a distally positioned lingual accessory cusp, simple and flattened U-shaped
1001 infundibulum, and a rounded buccally projecting hypoconulid. The occlusal length is within
1002 the range of *K. ellipsiprymnus*; nevertheless, the specimen is too fragmented to allow positive
1003 species identification. Rodentia is represented by two specimens, a maxilla fragment missing
1004 all molars, and an almost complete cranium including part of the mandible. Despite the
1005 completeness of this specimen, it is distorted, fragile and partially covered in matrix, making
1006 a more precise taxonomic identification difficult. Two isolated reptile teeth belonging to a
1007 species of *Varanus* were identified. The presence of *Struthio* is confirmed by numerous egg
1008 shell fragments recovered *in situ*. Additionally, two smaller-bodied species of birds are
1009 represented by incomplete long bone fragments.

1010

1011 While *Hippopotamus* is restricted to Africa today, during the Pleistocene it was common
1012 throughout parts of Europe and Asia^{72,73}. Dispersals out of Africa led to localised speciation
1013 events in Europe and the Levant⁷⁴; however, there is some debate surrounding the precise
1014 number of *Hippopotamus* species^{75,76}. While it seems likely that the Al Wusta specimens

1015 represent an out of Africa dispersal, it should be noted that *H. amphibius* has been identified
1016 at sites in Britain and Central Europe dated near the Middle to Late Pleistocene
1017 transition^{72,77,78}. *Pelorovis* is common in East Africa throughout the Pleistocene and is also
1018 found at a few sites in North Africa but is absent from Europe and the Levant after the Early
1019 Pleistocene⁷⁹⁻⁸¹. Both *Pelorovis* spp. and *Hippopotamus* have been identified at other sites in
1020 Saudi Arabia^{82,83} suggesting repeated dispersal events into the Arabian Peninsula during
1021 periods of climate amelioration. *Kobus* typically inhabit flood-plains and grasslands
1022 bordering water⁸⁴. During the Middle and Late Pleistocene *Kobus* was restricted to Africa and
1023 mostly south of the Maghreb. Notable northern occurrences were reported from Algeria and
1024 Egypt, associated with the Last Interglacial^{85,86}, but is unknown from the Levant during this
1025 period. This may support a tendency toward longitudinal dispersals⁸⁷, in this case eastward
1026 dispersal out of Africa and into the Arabian Peninsula via the Southern Levant. *Struthio* is
1027 common in Africa, but has also been identified by eggshell fragments on the Indian
1028 subcontinent from as early as the Middle Miocene and as recently as 18 ka^{87,88}. *Struthio* has
1029 been found at several sites in the Levant, and was extant in Southwest Asia until the 20th
1030 century.

1031

1032 Weathering of many specimens, particularly those collected from the surface at the western
1033 edge of the southern ridge at Al Wusta, suggests that they were likely exposed for a
1034 significant period of time post-fossilisation, with abrasion and polishing attributable to
1035 aeolian processes. Surface fossils included several refits recovered in close proximity,
1036 suggesting limited post-exposure transport. It is likely that such specimens became
1037 concentrated on the surface as a result of winnowing of the main fossiliferous layer. For these
1038 specimens, post-mortem weathering (i.e. prior to fossilisation) was impossible to determine
1039 due to the extensive fossil weathering of the cortical surfaces (i.e. following fossilization).

1040 Specimens collected *in situ* were typically better preserved and lacked the abrasion and
1041 polishing common to the specimens from the surface. However, pre-depositional weathering
1042 of these remains, on the other hand, was difficult to determine due to the fragmentary nature
1043 of the fossils and the fact that many specimens remain encrusted in carbonate. Despite the
1044 absence of body mammalian carnivores in the fossil assemblage, tooth pits potentially
1045 attributable to hyenas, large canids, or large felids are evident on some bones (Supplementary
1046 Figure 20H; Supplementary Table 21). Manganese staining is also present on numerous
1047 specimens. Two small bone fragments may have been burnt: one is blackened and the other
1048 one is dark brown in colour. However, their preservation is too poor to confidently rule out
1049 diagenetic discolouration. No additional bone surface modifications were observed, although
1050 this was not surprising considering that fine scale modifications are likely to have been
1051 removed during weathering.

1052

1053 Analysis of long bone circumference revealed a majority of type 1 shafts (75%), with type 2
1054 and type 3 occurring much less frequently (12% and 13%, respectively). The type 3 and type
1055 2 to type 1 index is 0.31, falling within the typical range identified for assemblages
1056 accumulated by carnivores and hominins⁸⁹. While extensive fossil weathering may also have
1057 contributed to the production of type 1 shafts; nevertheless, there is evidence for large
1058 carnivores and hominins at Al Wusta and it is likely that they contributed to the production of
1059 type 1 shafts during prey processing and consumption. Furthermore, the under-representation
1060 of epiphyses (N = 11) at Al Wusta supports carnivore ravaging of long bone ends⁹⁰ although
1061 this may also be an artefact of other non-biological preservation biases. Additional support
1062 that bone breaking agents were, at least in part, responsible for the accumulation of bones is
1063 the presence of green breaks (N = 12). Unfortunately, the assemblage is too poorly preserved
1064 to determine a primary accumulator.

1065 **SI 7. Al Wusta lithic technology.**

1066 **7.1 Introduction**

1067

1068 The Al Wusta lithic (stone tool) assemblage consists of 380 artefacts, systematically collected
1069 in transects and piece plotted from the southern end of the site in close proximity to the marl
1070 beds and from excavations in 2016 and 2017 (Figure 1). Lithics continued to the north, but
1071 were not included in the analysis here, which is limited to material south of the Holocene
1072 playa (Figure 1). The assemblage is Middle Palaeolithic in its characteristics, with a focus on
1073 centripetal Levallois reduction, particularly of chert and quartzite. Retouched tools are
1074 predominantly side-retouched flakes. The lithics, all from the same spatially restricted area,
1075 also display similar raw materials, weathering and technology and are therefore treated here
1076 as a single assemblage. The Al Wusta lithic assemblage is a valuable reference point for late
1077 MIS 5 Arabia, and displays similar technological features to other contemporary Arabian
1078 assemblages^{43,91-93}.

1079

1080 The Al Wusta lithic assemblage can be divided into the following categories (% in brackets
1081 shows % of total assemblage): 229 flakes (60.20%) [of which 36 are Levallois flakes,
1082 9.47%], 55 chips and chunks (14.47%), 21 retouched flakes (5.52%), one hammerstone
1083 (0.26%), and 74 cores (19.47%). Our aim here is to describe the basic technological
1084 characteristics of this lithic assemblage, which we analysed using the methodology and
1085 terminology described by Scerri and colleagues⁹⁴⁻⁹⁶ and Groucutt and colleagues^{93,97}.

1086

1087 The surface lithic assemblage was found closely associated with the marl deposits. Eleven
1088 lithics were excavated at the site, in the upper part of the marl and in the overlying *in situ*
1089 sand layer. The excavated material demonstrates similar characteristics to the larger sample

1090 from the surface, and includes similar raw material (focus on local lacustrine chert), three
1091 Levallois cores, flakes with faceted platforms and a debordant flake. The density of lithics
1092 on the surface, together with the considerable variation in their size suggests that they are not
1093 extensively redeposited, and we suggest that they were made by hominins beside the late MIS
1094 5 lakeshore and then deposited into the lake by gravity and low energy movement.

1095

1096 **7.2 Raw materials**

1097

1098 In terms of raw material composition, the most common material consists of
1099 a local lacustrine chert (65.09%), followed by quartzite (17.59%), ferruginous quartzite
1100 (11.02%), quartz (5.25%), argillaceous sandstone (0.52%), and other sandstone (0.52%). This
1101 raw material structure is unusual for the area. Al Wusta is the only identified Middle
1102 Palaeolithic assemblage in the region not dominated by quartzite, generally highly
1103 ferruginized^{91,92,97-99}. It appears that suitable quartzite is rare in the environs of Al Wusta, with
1104 our survey of the area showing an absence of large beds of ferruginous quartzite (Figure 5c).
1105 Non-ferruginous forms of quartzite (e.g. Figure 5f) are relatively common in the assemblage,
1106 and appear to occur as rounded pebbles of fluvial or conglomerate origin. Aside from chert,
1107 other materials occur in low frequencies, such as quartz (Figure 5e), which occurs as small
1108 pebbles in the bedrock of the area, and a rare type of rock which can be described as
1109 argillaceous sandstone⁹⁹ (Figure 5A).

1110

1111 The dominant raw material consists of chert, which occurs with varying colours and textures.
1112 The most common is brown in colour (e.g. Figure 5d). Our surveys of the area show that this
1113 material has formed in lakebeds in the area, which form a raw material source when exposed
1114 by subsequent erosion. We have conducted knapping experiments with this raw material,

1115 which shows that while variable, it is difficult material for knapping. The dominant chert at
1116 Al Wusta seems to be a particular poor quality form. The chert clasts are relatively small
1117 (always smaller than fist sized), have a very thick and undulating cortex, and frequently have
1118 inclusions. The material is also extremely hard, and has to be struck with considerable force
1119 to remove a flake. Despite these limitations, if knappers could access the inner part of the
1120 nodules, the chert is fine grained and appears to have reasonable properties of conchoidal
1121 fracture.

1122

1123 **7.3 Core technology**

1124

1125 The 74 residual Al Wusta cores are dominated by Levallois cores (54, 73%), with smaller
1126 numbers of non-Levallois multiple platform cores (12, 15.6%), double platform
1127 (bidirectional) cores (two, 2.7%), single platform cores (two, 2.7%), tested/minimally flaked
1128 cores (two, 2.7%), one radial core (i.e. a core flaked centripetally, but which is neither
1129 Levallois nor discoidal) (1.4%), and one core fragment (1.4%). It is clear, therefore, that
1130 reduction was dominated by use of the Levallois technique. Other methods appear more ad
1131 hoc in character. Multiple platform cores, for instance, tend to be small, having a mean
1132 weight of 19.3 g if one large outlier weighing 349.9 g is removed. This compares to the
1133 average weight for all cores of 34.9 g (with the same outlier also excluded). This suggests
1134 that multiple platform core reduction, the main non-Levallois reduction method, was
1135 employed on small clasts and/or on heavily reduced cores, which may have been Levallois
1136 cores earlier in reduction. There is no evidence of *façonnage* reduction, nor of blade
1137 production.

1138

1139 Of the 54 Levallois cores, 36 (66.7%) are preferential Levallois cores with centripetal
1140 preparation (e.g. Supplementary Figure 21a,b,d) and 13 (24.1%) are recurrent centripetal
1141 Levallois cores (e.g. Supplementary Figure 21C). The small number of pieces not in these
1142 categories are indeterminate Levallois cores where overshoot removals have removed the
1143 whole debitage surface (9.2%). From the geometry of the cores and the morphology of
1144 platform surface these are clearly centripetal Levallois cores, but it is not clear if their final
1145 phase of reduction was recurrent or preferential in character. Finally, one example each of
1146 recurrent unidirectional and recurrent bidirectional Levallois cores were identified. Striking
1147 platforms are faceted on 87% of the Levallois cores. In most cases preferential scars on
1148 Levallois cores demonstrate the product of parallel sided and sometimes oval Levallois
1149 flakes, with a small number producing pointed products.

1150

1151 Preferential and recurrent cores are similar in many features, for instance they have a similar
1152 number of scars (average of 12.9 and 10.9 respectively) and a similar percentage of cortical
1153 cover (23% and 27%). However, in terms of size recurrent cores are typically smaller (14.3 g,
1154 σ 9.0) than preferential cores (36.9 g, σ 42.7). These data indicate that, as a general pattern
1155 and perhaps within a situation of interchangeable reduction between Levallois methods,
1156 larger cores were reduced preferentially and a recurrent method was used late in reduction.
1157 The predominant focus on centripetal Levallois reduction demonstrates a level of
1158 homogeneity to core reduction at the site.

1159

1160 **7.4 Debitage**

1161 Lithic debitage (n=284) at Al Wusta can be classified as complete flakes (185, 65.1%),
1162 broken flakes (44, 15.5%) and chips/chunks (55, 19.4%). Our description here focusses on
1163 complete flakes.

1164

1165 The average length (technological), width (mid-point), thickness (mid-point), and weight of
1166 complete flakes are 29.8 mm (σ 11.9), 24.5 mm (σ 9.2), 8.46 mm (σ 4.2), and 13.1 g (σ 16.3)
1167 respectively. To aid comparability, if we exclude flakes which are less than 20 mm in length,
1168 these values become 32.25 mm (σ 11.3), 25.7 mm (σ 9.4), 9.3 mm (σ 4.3), and 14.6 (σ 16.9).

1169

1170 Other basic features for complete flakes >20 mm in length include an average cortical cover
1171 of 16.5% of the debitage surface, an average of 2.8 dorsal scars (σ 1.7), striking platforms are
1172 prepared (faceted or dihedral) in 41.6% percent of cases and striking platforms have average
1173 external platform values of 74.9° (σ 6.2). Dorsal scar patterns can be classified as: 31.5%
1174 unidirectional, 2.4% unidirectional convergent, 1.6% perpendicular, 3.1% crossed, 11.8%
1175 bidirectional, 13.4% subcentripetal, and 36.2% centripetal.

1176

1177 Complete Al Wusta Levallois flakes (e.g. Supplementary Figure 21E,G-K) are on average 33
1178 mm in length, 25.5 mm in width and 7.4 mm thick. They are generally broadly parallel sided
1179 in shape. They most commonly (64.5%) have centripetal scar patterns, with a further 12.9%
1180 having subcentripetal scar patterns. The remaining Levallois flakes are characterised by
1181 unidirectional scar patterns (16.1%) and unidirectional convergent (6.5%). 74.2% of the Al
1182 Wusta Levallois flakes have prepared platforms.

1183

1184 Summarising these data, Al Wusta flakes are therefore typically small, quite commonly
1185 cortical and with various scar patterns but particularly unidirectional and centripetal.
1186 Levallois flakes are also small, and indicate a tendency to produce Levallois flakes by
1187 centripetal preparation and hard hammer percussion from prepared platforms. These

1188 characteristics are consistent with the evidence from the cores in indicating that lithic
1189 technology at Al Wusta is focussed on centripetal Levallois reduction.

1190

1191 **7.5 Retouched flakes**

1192

1193 A total of 21 retouched flakes were found at Al Wusta (15 complete). Three of these have
1194 only distal retouch (e.g. Supplementary Figure 21m), seven are retouched along one lateral
1195 (e.g. Supplementary Figure 21n), seven are retouched on both laterals (e.g. Supplementary
1196 Figure 21l), and two are retouched on both laterals and distally (two more are fragments).

1197 Where it can be determined, 87.5% of striking platforms are faceted or dihedral.

1198

1199 Of the complete retouched pieces, they are mostly parallel sided and 66.7% have either
1200 cortical surfaces or unidirectional scar patterns. Their average length, width, thickness and
1201 weight are 33.6 mm (σ 11.5), 24.34 mm (σ 12.4), 10.7 mm (σ 2.4), and 15.9 g (σ 2.4). These
1202 are similar values to the overall flake population.

1203

1204 In most cases retouch is 'regular', while 33% of retouched flakes have notches as well as
1205 regular retouch. In all but one case, the retouch is continuous rather than clustered, and
1206 virtually all of the retouch is semi-abrupt. Retouch is always found on either the dorsal
1207 surface or on both surfaces, and never exclusively on the ventral surface. Index of
1208 Invasiveness (I of I)¹⁰⁰, values range from 0.094 to 0.5, averaging at 0.25. Geometric Index of
1209 Unifacial retouch (GIUR)¹⁰¹ values range from 0.45 to 0.89 with an average of 0.69. The
1210 quite low values for I of I and high values for GIUR demonstrates that retouch was not
1211 horizontally extensive across the face of the flakes, but was vertically quite intensive.

1212

1213 The retouched component of Al Wusta therefore shows a focus on typical side retouched
1214 flakes (“scrapers”) with prepared platforms, as is commonly the case for Middle Palaeolithic
1215 assemblages.

1216

1217 **7.6 Al Wusta lithic technology in comparative context**

1218

1219 The lithic assemblage of Al Wusta demonstrates a consistent approach to lithic technology,
1220 focussed on centripetal Levallois technology. Here we will briefly consider this technology in
1221 relation to sites elsewhere in Arabia and surrounding regions.

1222

1223 The corpus of Arabian sites which can be related to later MIS 5 by chronometric dating
1224 techniques is small, but increasing. These include the ~75 ka assemblage at JQ-1 at
1225 Jubbah^{43,91}, the ~ 100-60 ka assemblage from JSM-1 at Jubbah^{91,95}, and the ~85 ka assemblage
1226 from Mundafan Al Buhayrah in southwestern Arabia⁹³. We emphasise the latter assemblage
1227 from Mundafan as the key example, with both good chronometric age estimates and a large
1228 and diagnostic lithic assemblage. Most Arabian Middle Palaeolithic assemblages remain
1229 undated, or have produced contradictory age estimates, which mean little can be said on their
1230 age with certainty. The available chronologically secure data indicate that mid to late MIS 5
1231 sites demonstrate a focus on centripetal Levallois reduction, with both centripetally prepared
1232 preferential and recurrent centripetal Levallois methods employed. In all cases they lack
1233 bifacial façonnage technology and beaked (‘Nubian’) Levallois reduction. Levallois point
1234 production only occurs at marginal levels. Differences at these sites tend to correlate with raw
1235 material aspects. Both MDF-61 and JQ-1 appear to be located far (>10 km) from good raw
1236 material sources, and in both cases demonstrate highly reduced assemblages, both in terms of
1237 core reduction and high levels of retouch^{93,99}. In terms of size aspects, lithics at Al Wusta are

1238 relatively small for MP/MSA assemblages. They are much smaller than many Arabian sites,
1239 but also not as small as sites with highly reduced assemblages elsewhere in southwest Asia,
1240 such as Tor Faraj in Jordan and Warwasi in Iran^{93,97,102}. We associate these small size aspects
1241 primarily with raw material factors at Al Wusta. The relatively high levels of retouch at Al
1242 Wusta likewise likely correlate with the limitations of raw material in the area, encouraging
1243 resharpening/edge rejuvenation of existing pieces.

1244

1245 In areas to the north and west of Arabia a number of assemblages date to mid to late MIS 5
1246 and share similar technological characteristics with Al Wusta. In the Levant this is most
1247 clearly demonstrated by Qafzeh Cave, with its famous *Homo sapiens* fossils, dating to ~100-
1248 90 ka¹⁰¹. Moving into northeast Africa, sites such as 1017 and 34a have been attributed to
1249 later MIS 5 (~85-80 ka) on both stratigraphic grounds and with preliminary chronometric age
1250 estimates¹⁰⁴⁻¹⁰⁶. The technology of these sites again demonstrates a focus on centripetal
1251 Levallois reduction. The Bir Tarfawi and Bir Sahara palaeolakes feature broadly similar
1252 technology, and were repeatedly occupied during the wet phases of MIS 5¹⁰⁷. In the Horn of
1253 Africa key evidence comes from a series of dated assemblages in the Aduma area¹⁰⁸. These
1254 date to between ~100 and 80 thousand years ago, and as with sites such as Al Wusta
1255 demonstrate a focus on the centripetal reduction of small Levallois cores, and are also
1256 associated with *Homo sapiens* fossils. While these sites feature similar core reduction
1257 methods, in contrast to, for example, the unidirectional focus of MIS 4-3 Neanderthal
1258 assemblages in southwest Asia, further research is needed to understand similarities and
1259 differences in areas such as retouched tool technology.

1260

1261 While traditionally masked by variable analytical methodologies, differing regional
1262 nomenclatures and a lack of knowledge on areas such as Arabia, we interpret these findings

1263 as indicating broad technological similarities across a large area in mid to late MIS 5¹¹⁰.
1264 However, East African sites appear to feature more of a focus on retouched point production
1265 (although this must be matched against these sites having large sample sizes compared to
1266 assemblages in places such as Arabia). In terms of core reduction methods, however,
1267 assemblages in East Africa, northeast Africa, the Levant and Arabia all appear to be similar
1268 in mid to late MIS 5. In line with available fossil evidence, we note that this pattern appears
1269 to be most ancient in East Africa^{108,109}. In contrast to East Africa, areas such as the Nile
1270 Valley, the Levant and Arabia demonstrate highly variable MP/MSA records. This pattern
1271 suggests that at least in terms of visible (archaeologically preserved) aspects of material
1272 culture, the earlier phases of dispersal into southwest Asia did not relate to radical
1273 technological innovation. Phases of dispersal correlate with windows of climatic amelioration
1274 in the Saharo-Arabian arid belt, while further research is needed to understand the nature of
1275 demographic, social and behavioural changes in sub-Saharan Africa which might have
1276 triggered dispersals. Beyond these broad observations of similarities in contemporaneous
1277 similarities, detailed comparative studies of chronometrically constrained lithic assemblages
1278 are needed to clarify patterns of similarities and differences in lithic assemblages.

1279

1280

1281

1282

1283

1284

1285

1286

1287 **Supplementary References**

1288

- 1289 1. Martinez-Navarro, B., *et al.* Early Pleistocene “hominid remains” from southern
1290 Spain and the taxonomic assignment of the Cueva Victoria phalanx. *J. Hum. Evol.* **48**,
1291 517-523 (2005).
- 1292 2. Martinez-Navarro, B., *et al.* Reply to Gilbert et al. (2008) on the supposed human
1293 phalanx from Cueva Victoria (Cartagena, Spain). *J. Hum. Evol.* **54**, 157-161 (2008).
- 1294 3. Ruff, C. B. Body size, body shape, and long bone strength in modern humans. *J.*
1295 *Hum. Evol.* **38**, 269-90 (2000).
- 1296 4. Pearson O. M, Lieberman D. E. The aging of Wolff's "law": ontogeny and responses
1297 to mechanical loading in cortical bone. *Am. J. Phys. Anthropol.* **125**, 63-99 (2004)
- 1298 5. Ruff, C., Holt, B., Trinkaus, E. Who's afraid of the big bad Wolff?: "Wolff's law" and
1299 bone functional adaptation. *Am. J. Phys. Anthropol.* **129**, 484-98 (2006).
- 1300 6. Ruff, C. B., Trinkaus, E., Walker, A., Larsen, C. S. Postcranial robusticity in Homo. I:
1301 Temporal trends and mechanical interpretation. *Am. J. Phys. Anthropol.* **91**, 21-53
1302 (1993).
- 1303 7. Rasband, W. S. *ImageJ*. Bethesda, Maryland, USA: U.S. National Institutes of
1304 Health, <http://imagej.nih.gov/ij/> (1997-2016).
- 1305 8. Doube, M. et al. BoneJ: Free and extensible bone image analysis in ImageJ. *Bone* **47**,
1306 1076-9 (2010).
- 1307 9. Ruff, C.B. in *Biological Anthropology of the Human Skeleton* (Katzenberg M.A.,
1308 Saunders, S.R.) 183-206 (Wiley, 2007).
- 1309 10. Ruff, C. Sexual dimorphism in human lower limb bone structure: relationship to
1310 subsistence strategy and sexual division of labor. *J. Hum. Evol.* **16**, 391-416 (1987).

- 1311 11. Shaw, C. N, Stock, J. T. Intensity, repetitiveness, and directionality of habitual
1312 adolescent mobility patterns influence the tibial diaphysis morphology of athletes.
1313 *Am. J. Phys. Anth.* **140**, 149-59 (2009).
- 1314 12. Grün, R., Eggins, S., Kinsley, L., Mosely, H., Sambridge, M. Laser ablation U-series
1315 analysis of fossil bones and teeth. *Palaeogeogr., Palaeoclimatol., Palaeoecol.* **416**,
1316 150-167 (2014).
- 1317 13. Benson, A., Kinsley, L., Defleur, A., Kokkonen, H., Mussi, M., Grün, R., 2013. Laser
1318 ablation depth profiling of U-series and Sr isotopes in human fossils. *J. Arch. Sci.* **40**,
1319 2991-3000 (2013).
- 1320 14. Grün, R. Methods of dose determination using ESR spectra of tooth enamel. *Radiat.*
1321 *Meas.* **32**, 767-772 (2000).
- 1322 15. Duval, M., Grün, R., Falguères, C., Bahain, J.J., Dolo, J.M. ESR dating of Lower
1323 Pleistocene fossil teeth: Limits of the single saturating exponential (SSE) function for
1324 the equivalent dose determination. *Radiat. Meas.* **44**, 477-482 (2009).
- 1325 16. Duval, M., Guilarte Moreno, V., Grün, R. ESR dosimetry of fossil enamel: some
1326 comments about measurement precision, long-term signal fading and dose–response
1327 curve fitting. *Rad. Prot. Dosim.* **157**, 463-476 (2013).
- 1328 17. Duval, M., Grün, R. Are published ESR dose assessments on fossil tooth enamel
1329 reliable? *Quatern. Geochron.* **31**, 19-27 (2016).
- 1330 18. Grün, R., Katzenberger-Apel, O. An alpha irradiator for ESR dating. *Ancient TL* **12**,
1331 35-38 (1994).
- 1332 19. Marsh, R. E. *Beta-gradient Isochrons Using Electron Paramagnetic Resonance:*
1333 *Towards a New Dating Method in Archaeology.* (MSc thesis, McMaster University,
1334 Hamilton, 1999).

- 1335 20. Guérin, G., Mercier, N., Adamiec, G.. Dose rate conversion factors: update. *Ancient*
1336 *TL* **29**, 5-8 (2011).
- 1337 21. Grün, R. The DATA program for the calculation of ESR age estimates on tooth
1338 enamel. *Quatern. Geochron.* **4**, 231-232 (2009).
- 1339 22. Grün, R., Schwarcz, H.P., Chadam, J. ESR dating of tooth enamel: Coupled
1340 correction for U-uptake and U-series disequilibrium. *Int. J. Radiat. Appl. Instrum.*
1341 *Nucl. Tracks. Radiat. Meas.* **14**, 237-241 (1988).
- 1342 23. Duval, M. in *Encyclopaedia of Scientific Dating* (eds Rink, W.J., Thompson, J.W.)
1343 239-246 (Springer, 2015).
- 1344 24. Ludwig, K. R. *User's manual for Isoplot 3.75*. Berkeley Geochronology Center,
1345 Special Publication **5**, 1-75 (2012).
- 1346 25. Sambridge, M., Grün, R., Eggins, S. U-series dating of bone in an open system: The
1347 diffusion-adsorption-decay model. *Quatern. Geochron.* **9**, 42-53 (2012).
- 1348 26. Bøtter-Jensen, L., Andersen, C. E., Duller, G. A. T., Murray, A. S. Developments in
1349 radiation, stimulation and observation facilities in luminescence measurements.
1350 *Radiat. Meas.* **37**, 535-541 (2003).
- 1351 27. Duller, G. A. T., Bøtter-Jensen, L., Murray, A. S. Combining infrared- and green-
1352 laser stimulation sources in single-grain luminescence measurements of feldspar and
1353 quartz. *Radiat. Meas.* **37**, 543-550 (2003).
- 1354 28. Duller, G. A. T., Bøtter-Jensen, L., Murray, A. S., Truscott, A. J. Single grain laser
1355 luminescence (SGLL) measurements using a novel automated reader. *Nucl. Instr.*
1356 *Meth. Phys. Res.* **155**, 506-514 (1999).
- 1357 29. Armitage, S., Bailey, R. The measured dependence of laboratory beta dose rates on
1358 sample grain size. *Radiat. Meas.* **39**, 123-127 (2005).

- 1359 30. Ballarini, M., Wintle, A. G., Wallinga, J. Spatial variation of dose rate from beta
1360 sources as measured using single grains. *Ancient TL* **24**, 1-7 (2006).
- 1361 31. Armitage, S. J., Jasim, S. A., Marks, A. E., Parker, A. G., Usik, V. I., Uerpmann, H. -
1362 P. The Southern Route "Out of Africa": Evidence for an Early Expansion of Modern
1363 Humans into Arabia. *Science* **331**, 453-456 (2011).
- 1364 32. Murray, A. S., Wintle, A. G. Luminescence dating of quartz using an improved
1365 single-aliquot regenerative-dose protocol. *Radiat. Meas.* **32**, 57-73 (2000).
- 1366 33. Jacobs, Z. et al. Ages for the Middle Stone Age of southern Africa: Implications for
1367 human behavior and dispersal. *Science* **322**, 733-735 (2008).
- 1368 34. Roberts, R. G., Galbraith, R. F., Olley, J. M., Yoshida, H., Laslett, G. M. Optical
1369 dating of single and multiple grains of quartz from Jinmium rock shelter, northern
1370 Australia: Part II, results and implications. *Archaeometry* **41**, 365-395 (1999).
- 1371 35. Wallinga, J., Murray, A., Duller, G. A. T. Underestimation of equivalent dose in
1372 single-aliquot optical dating of feldspars caused by preheating. *Radiat. Meas.* **32**, 691-
1373 695 (2000).
- 1374 36. Jacobs, Z., Duller, G.A.T., Wintle, A.G. Interpretation of single grain Distributions
1375 and calculation of De. *Radiat. Meas.* **41**, 264-277 (2006).
- 1376 37. Thomsen, K.J., Murray, A.S., Bøtter-Jensen, L. Sources of variability in OSL dose
1377 measurements using single grains of quartz. *Radiat. Meas.* **39**, 47-61 (2005).
- 1378 38. Duller, G. A. T. Assessing the error on equivalent dose estimates derived from single
1379 aliquot regenerative dose measurements. *Ancient TL* **25**, 15-24 (2007).
- 1380 39. Duller, G. A. T., Bøtter-Jensen, L., Murray, A. S. Optical dating of single sand-sized
1381 grains of quartz: Sources of variability. *Radiat. Meas.* **32**, 453-457 (2000).
- 1382 40. Jacobs, Z., Duller, G. A. T., Wintle, A. G. Optical dating of dune sand from Blombos
1383 Cave, South Africa: II - Single grain data. *J. Hum. Evol.* **44**, 613-625 (2003).

- 1384 41. Thomsen, K. J., Murray, A. S., Bøtter-Jensen, L., Kinahan, J. Determination of burial
1385 dose in incompletely bleached fluvial samples using single grains of quartz. *Radiat.*
1386 *Meas.* **42**, 370-379 (2007).
- 1387 42. Duller, G. A. T. Distinguishing quartz and feldspar in single grain luminescence
1388 measurements. *Radiat. Meas.* **37**, 161-165 (2003).
- 1389 43. Petraglia, M. D. et al. Hominin Dispersal into the Nefud Desert and Middle
1390 Palaeolithic Settlement along the Jubbah Palaeolake, Northern Arabia. *PLoS ONE* **7**,
1391 e49840 (2012).
- 1392 44. Galbraith, R. F., Roberts, R. G., Laslett, G. M., Yoshida, H., Olley, J. M. Optical
1393 dating of single and multiple grains of quartz from Jinmium rock shelter, northern
1394 Australia: Part I, experimental design and statistical models. *Archaeometry* **41**, 339-
1395 364 (1999).
- 1396 45. Armitage, S. J., King, G. E. Optically stimulated luminescence dating of hearths from
1397 the Fazzan Basin, Libya: A tool for determining the timing and pattern of Holocene
1398 occupation of the Sahara. *Quat. Geochronol.* **15**, 88-97 (2013).
- 1399 46. Tribolo, C., Mercier, N., Rasse, M., Soriano, S., Huyssecom, E. Kobo 1 and L'Abri aux
1400 Vaches (Mali, West Africa): Two case studies for the optical dating of bioturbated
1401 sediments. *Quat. Geochronol.* **5**, 317-323 (2010).
- 1402 47. Bøtter-Jensen, L., Mejdahl, V. Assessment of beta dose-rate using a GM multicounter
1403 system. *Int. J. Rad. Appl. Instrum. B.* **14**, 187-191 (1988).
- 1404 48. De Corte, F. et al. Preparation and characterization of loess sediment for use as a
1405 reference material in the annual radiation dose determination for luminescence dating.
1406 *J. Radioanal. Nucl. Chem.* **272**, 311-319 (2007).
- 1407 49. Hong, D. *Luminescence stimulated from quartz by green light: developments relevant*
1408 *to dating.* (PhD thesis, University of Edinburgh, 1988).

- 1409 50. Mejdahl, V. Thermoluminescence dating: Beta- dose attenuation in quartz grains.
1410 *Archaeometry* **21**, 61-72 (1979).
- 1411 51. Prescott, J. R., Hutton, J. T. Cosmic ray and gamma ray dosimetry for TL and ESR.
1412 *Int. J. Rad. Appl. Instrum.* **14**, 223-227 (1988).
- 1413 52. Bennett K. D. Determination of the Number of Zones in a Biostratigraphical
1414 Sequence. *New Phytologist* **132**, 155-170 (1996).
- 1415 53. Wagner B, *et al.* A 40,000-year record of environmental change from ancient Lake
1416 Ohrid (Albania and Macedonia). *J. Paleolimnology* **41**, 407-430 (2009).
- 1417 54. Bennion, H., Simpson, G. The use of diatom records to establish reference conditions
1418 for UK lakes subject to eutrophication. *J. Paleolimnology* **45**, 1-20 (2011).
- 1419 55. Rosenberg, T. M. *et al.* Middle and Late Pleistocene humid periods recorded in
1420 palaeolake deposits of the Nafud desert, Saudi Arabia. *Quatern. Sci. Rev.* **70**, 109-123
1421 (2013).
- 1422 56. Saros, J. E., Anderson, N. J. The ecology of the planktonic diatom *Cyclotella* and its
1423 implications for global environmental change studies. *Bio. Rev. Camb. Philos.* **90**,
1424 522-541 (2015).
- 1425 57. Wunsam, S., Schmidt, R., Klee, R. *Cyclotella*-taxa (Bacillariophyceae) in lakes of the
1426 Alpine region and their relationship to environmental variables. *Aquat. Sci.* **57**, 360-
1427 386 (1995).
- 1428 58. Verschuren, D., Laird, K. R., Cumming, B. F. Rainfall and drought in equatorial east
1429 Africa during the past 1,100 years. *Nature* **403**, 410-414 (2000).
- 1430 59. Wolin, J. A., Stone, J. R. in *The Diatoms Applications to the Environmental and*
1431 *Earth Sciences* (eds Stomer, F., Smol, J.P.) 174-185 (Cambridge University Press,
1432 2010)

- 1433 60. McGowan, S., Grauert, M., Anderson, N. J. A late Holocene record of landscape
1434 degradation from Heygsvatn, the Faroe Islands. *Palaeogeography Palaeoclimatology*
1435 *Palaeoecology* **264**(1-2) 11-24 (2008).
- 1436 61. Phillips, G., Pietilainen, O. P., Carvalho, L., Solimini, A., Solheim, A. L., Cardoso, A.
1437 C Chlorophyll-nutrient relationships of different lake types using a large European
1438 dataset. *Aquatic Ecology* **42**(2) 213-226 (2008).
- 1439 62. Alonso-Zarza, A. M. Palaeoenvironmental significance of palustrine carbonates and
1440 calcretes in the geological record. *Earth Sci. Rev.* **60**, 261-298 (2003).
- 1441 63. Verrecchia, E. P. in *Geochemical Sediments and Landscapes* (eds Nash, D. J.,
1442 McLaren, S. J.) 298-329 (Blackwell, 2007).
- 1443 64. Talbot, M. R. A review of the palaeohydrological interpretation of carbon and oxygen
1444 isotopic ratios in primary lacustrine carbonates. *Chem. Geol.* **80**, 261-279 (1990).
- 1445 65. Li, H. C., Ku, T. L. $\delta^{13}\text{C}$ - $\delta^{18}\text{O}$ covariance as a paleohydrological indicator for closed-
1446 basin lakes. *Palaeogeogr. Palaeoclimatol. Palaeoecol.* **133**, 69-80 (1997).
- 1447 66. Leng, M.J. and Marshall, J.D. Palaeoclimate interpretation of stable isotope data from
1448 lake sediment archives. *Quatern. Sci. Rev.* **23**, 811-831 (2004).
- 1449 67. Holmes, J.A., et al. Holocene palaeolimnology of Kajemamm Oasis, Northern
1450 Nigeria: an isotopic study of ostracodes, bulk carbonate and organic carbon. *J. Geol.*
1451 *Soc.*, **154**, 311-319 (1997).
- 1452 68. Marshall, J.D., et al. A high resolution late glacial isotopic record from Hawes Water,
1453 Northwest England. Climatic oscillations: calibration and comparison of
1454 palaeotemperature proxies. *Palaeogeogr., Palaeoclimatol., Palaeoecol.* **185**, 25-40
1455 (2002).
- 1456 69. Rozanski, K., Araguas-Araguas, L., Gonfiantini, R. Isotopic Patterns in Modern
1457 Global Precipitation. In: Swart, P.K., Lohmann, K.C., McKenzie, J., Savin, S. (eds).

- 1458 *Climate Change in Continental Isotopic Records*. Geophysical Monograph 78,
1459 American Geophysical Union, 1-36 (1993).
- 1460 70. Parton, A., et al. Orbital-scale climate variability in Arabia as a potential motor for
1461 human dispersals. *Quatern. Int.* **382**, 82-97 (2015).
- 1462 71. Fleitmann, D., Matter, A., Pint, J.J., Al-Shanti, M. The speleothem record of climate
1463 change in Saudi Arabia. Saudi Geological Survey report, SGS-OF-2004-8 (2004).
- 1464 72. Eltringham, S. K. *The Hippos: Natural History and Conservation* (Academic Press,
1465 London, 1999)
- 1466 73. Estres, R. D. *The Behaviour Guide to African Mammals*. (University of California
1467 Press, Berkeley, 1991).
- 1468 74. Belmaker, M. In *Out of Africa I: The First Hominin Colonization of Eurasia* (eds.
1469 Fleagle, J. G., Shea, J. J., Grine, F. E., Baden, A. L., Leakey, R. E.) 183-205
1470 (Springer, 2010).
- 1471 75. Martínez-Navarro, B. in *Out of Africa I: The First Hominin Colonization of Eurasia*
1472 (eds. Fleagle, J. G., Shea, J. J., Grine, F. E., Baden, A. L. & Leakey, R. E) 207-224
1473 (Springer, New York, 2010).
- 1474 76. Martínez-Navarro, B., Rook, L., Segid, A., Yosief, D., Farretti, M. P., Shoshani, J.,
1475 Techle, T. M., Libsekal, Y. The large fossil mammals from Buia (Eritrea):
1476 systematics, biochronology and paleoenvironments. *Riv. Ital. Paleontol. S.***110**, 61-88
1477 (2004).
- 1478 77. Shreeve, D. C. A new record of Pleistocene hippopotamus from River Severn terrace
1479 deposits, Gloucester, UK-palaeoenvironmental setting and stratigraphical
1480 significance. *P. Geologist. Assoc.* **120**, 58-64 (2009).
- 1481 78. van Kolfschoten, Th. The Eemian mammal fauna of central Europe. *Geol. Mijnbouw-*
1482 *N. J. G.* **79**, 269-281 (2000).

- 1483 79. Tchernov, E. The Afro-Arabian Component in the Levantine Mammalian Fauna – A
1484 Short Biogeographical Review. *Isr. J. Zool.* **38**, 155-159 (1992).
- 1485 80. Geraads, D. Plio-Pleistocene Mammalian Biostratigraphy of Atlantic Morocco.
1486 *Quaternaire.* **13**, 43-53 (2002).
- 1487 81. Michel, P., Wengler, L. *Un Site Palaeontologique Avec Des Vestiges Archeologiques:*
1488 *La Carriere Doukkala II* (Region De Temara – Maroc Atlantique). **5**, 11-41 (1993).
- 1489 82. Stimpson, C. et al. Middle Pleistocene vertebrate fossils from the Nefud Desert, Saudi
1490 Arabia: Implications for biogeography and palaeoecology. *Quatern. Sci. Rev.* **143**, 13-
1491 36 (2016).
- 1492 83. McClure, H. A. *Late Quaternary Palaeoenvironments of the Rub' al Khali.* (PhD
1493 Thesis, Univeristy College, London, 1984).
- 1494 84. O'Regan, H. J., Turner, A., Bishop, L. C., Elton, S., Lamb, A. L. Hominins without
1495 fellow travellers? First appearances and inferred dispersals of Afro-Eurasian large
1496 mammals in the Plio-Pleistocene. *Quatern. Sci. Rev.* **30**, 1343-1352 (2011).
- 1497 85. Hadjouis, D. Présence du Genera Kobus (Bovidae, Artiodactyla) dans le Pléistocène
1498 Supérieur D'Algérie. *L'Anthropologie.* **90**, 317-320 (1986).
- 1499 86. Kowalski, K., Neer, W. V., Bockenski, Z., Mlynarsko, M., Rzabik-Kowalska, B.,
1500 Szyndlar, Z., Gautier, A., Close, A. E., Wendorf, F. A Last Interglacial Fauna from
1501 the Eastern Sahara. *Quat. Res.* **32**, 335-341 (1989).
- 1502 87. Blinkhorn, J., Achyuthan, H., Petraglia, M. D. Ostrich expansion into India during the
1503 Late Pleistocene: Implications for continental dispersal corridors. *Palaeogeogr.,*
1504 *Palaeoclimatol., Palaeoecol.* **417**, 80-90 (2015).
- 1505 88. Jain, S., Rai, N., Kumar, G., Pruthi, P. A., Thangaraj, K., Bajpai, S., Pruthi, V.
1506 Ancient DNA Reveals Late Pleistocene Existence of Ostriches in Indian Sub-
1507 Continent. *PLoS ONE.* **12**, e0164823 (2017).

- 1508 89. Domínguez-Rodrigo, M., Egeland, C. P., Barba, R. in *Deconstructing Olduvai: A*
1509 *Taphonomic Study of the Bed I Sites* (eds. Domingues-Rodrigo, M., Barba, R. &
1510 Egeland, C. P.) 23-32 (Springer, New York, 2007)
- 1511 90. Cruz-Urbe, K. Distinguishing hyena from hominid bone accumulations. *J. F.*
1512 *Archaeol.* **18**, 467–486 (1991).
- 1513 91. Petraglia, M. D. et al. Middle Palaeolithic occupation on a Marine Isotope Stage 5
1514 lakeshore in the Nefud Desert, Saudi Arabia. *Quatern. Sci. Rev.* **30**, 1555-1559
1515 (2011).
- 1516 92. Scerri, E. M. L. et al. Middle to Late Pleistocene human habitation in the western
1517 Nefud Desert. *Quatern. Int.* **382**, 200-214 (2015).
- 1518 93. Groucutt, H. S. et al. Human occupation of the Arabian Empty Quarter during MIS 5:
1519 evidence from Mundafan al-Buhayrah. *Quatern. Sci. Rev.* **119**, 116-135 (2015).
- 1520 94. Scerri, E. M. L., Drake, N. A., Jennings, R., Groucutt, H. S. Earliest evidence for the
1521 structure of *Homo sapiens* populations in Africa. *Quatern. Sci. Rev.* **101**, 207-2016
1522 (2014).
- 1523 95. Scerri, E. M. L., Groucutt, H. S., Jennings, R. P., Petraglia, M. D. Unexpected
1524 technological heterogeneity in northern Arabia indicates complex Late Pleistocene
1525 demography at the gateway to Asia. *J. Hum. Evol.* **75**, 125-142 (2014).
- 1526 96. Scerri, E. M. L., Gravina, B., Blinkhorn, J., Delagnes, A. Can lithic attribute analyses
1527 identify discrete reduction trajectories? A quantitative study using refitted lithic sets.
1528 *J. Arch. Method Theory* **23**, 669-691.
- 1529 97. Groucutt, H. S. et al. Late Pleistocene lakeshore settlement in Arabia: Middle
1530 Palaeolithic technology from Jebel Katefeh, Jubbah. *Quatern. Int.* **382**, 215-236.

- 1531 98. Jennings, R. P., Parton, A., Clark-Balzan, L., White, T. S., Groucutt, H. S., Breeze, P.,
1532 Parker, A. G., Drake, N. A., Petraglia, M. D. Human occupation of the northern
1533 Arabia interior during early Marine Isotope State 3. *J. Quat. Sci.* **31**, 953-966 (2017).
- 1534 99. Groucutt, H. S. et al. Middle Palaeolithic raw material procurement and early stage
1535 reduction at Jubbah, Saudi Arabia. *Arch. Res. Asia.* **9**, 44-62 (2017).
- 1536 100. Clarkson, C. An Index of Invasiveness for the measurement of unifacial and
1537 bifacial retouch: a theoretical, experimental, and archaeological verification. *J. Arch.*
1538 *Sci.* **29**, 65-75.
- 1539 101. Kuhn, S. L., A geometric index of reduction for unifacial stone tools. *J. Arch.*
1540 *Sci.* **17**, 583-593 (1990).
- 1541 102. Groucutt, H.S. Middle Palaeolithic point technology, with a focus on the site
1542 of Tor Faraj (Jordan, MIS 3). *Quatern. Int.* **350**, 205-226.
- 1543 103. Hovers, E. *The Lithic Assemblages of Qafzeh Cave* (Oxford University Press,
1544 2009).
- 1545 104. Marks, A. E. in *The Prehistory of Nubia, Vol. 1* (ed Wendorf, F.) 315-391
1546 (SMU Press, 1968).
- 1547 105. Goder-Goldberger, M. The Khormusan: Evidence for an MSA East African
1548 industry in Nubia. *Quatern. Int.* **300**, 182-194 (2013).
- 1549 106. Rose, J. I., Marks, A. E. "Out of Arabia" and the Middle-Upper Palaeolithic
1550 transition in the southern Levant. *Quartär* **61**, 49-85 (2014).
- 1551 107. Wendorf, F., Schild, R., Close, A. E., and associates. *Egypt During the Last*
1552 *Interglacial: The Middle Paleolithic of Bir Tarfawi and Bir Sahara East*. (Plenum,
1553 1993).
- 1554 108. Yellen, J. et al. The archaeology of Aduma Middle Stone Age sites in the
1555 Awash Valley, Ethiopia. *Paleoanthropology* **2005**, 25-100 (2005).

- 1556 109. Shea, J. J. 2008. The Middle Stone Age archaeology of the Lower Omo Valley
1557 Kibish Formation: Excavations, lithic assemblages, and inferred patterns of early
1558 *Homo sapiens* behaviour. *J. Hum. Evol.* **55**, 448-485 (2008)
- 1559 110. Groucutt, H. S. et al. Stone tool assemblages and models for the dispersal of
1560 *Homo sapiens* out of Africa. *Quatern. Int.* **382**, 8-30 (2015).
- 1561 111. Horwitz, L.K., Smith, P., Faerman, M., Boaretto, E., Segal, I. The application
1562 of biometry LA-ICP-MS to provenance isolated bones: a study of hominin remains
1563 from Oumm-Qatafa Cave, Judean Desert. *Archaeol. Anthropol. Sci.* **3**, 245-62 (2011).
- 1564 112. Walker, M. J., Ortega, J., López, M. V., Parmová, K. & Trinkaus, E.
1565 Neanderthal postcranial remains from the Sima de las Palomas del Cabezo Gordo,
1566 Murcia, Southeastern Spain. *Am. J. Phys. Anthropol.* **144**, 505-515 (2011).
- 1567 113. Lorenzo, C, Arsuaga, J, Carretero, J.M. Hand and foot remains from the Gran
1568 Dolina Early Pleistocene site (Sierra de Atapuerca, Spain). *J. Hum. Evol.* **37**, 501-522
1569 (1999).
- 1570 114. Larson, S.G. et al. Descriptions of the upper limb skeleton of *Homo*
1571 *floresiensis*. *J. Hum. Evol.* **57**, 555-570 (2009).
- 1572 115. Mersey, B., Jabbour, R.S., Brudvik, K., Defleur, A. Neandertal hand and foot
1573 remains from Moula-Guercy, Ardeche, France. *Am. J. Phys. Anthropol.* **152**, 516-529
1574 (2013).
- 1575 116. Semal, P., et al. New data on the late Neanderthals: direct dating of the
1576 Belgian Spy Fossils. *Am. J. Phys. Anthropol.* **138**, 421-428 (2009).
- 1577 117. Trinkaus, E. *The Shanidar Neanderthals*. (Academic Press, New York, 1983).
- 1578 118. Trinkaus E. *The Krapina Human Postcranial Remains: Morphology,*
1579 *Morphometrics and Paleopathology*. (University of Zagreb, Zagreb, 2016)

- 1580 119. Sládek, V, Trinkaus, E, Hillson, S.W., Holliday, T.W. The people of the
1581 Pavlovian. Skeletal catalogue and osteometrics of the Gravettian fossil hominids from
1582 Dolni Vestonice and Pavlov. *Dolni Vestonice Studies, Svazek 5* (2000).
- 1583 120. Trinkaus, E., Buzhilova, A.P., Mednikova, M.B., Dobrovolskaya, M.V. *The*
1584 *people of Sunghir: burials, bodies, and behavior in the earlier Upper Paleolithic.*
1585 (Oxford University Press, Oxford, 2014).
- 1586 121. Shang, H., Trinkaus, E. *The early modern human from Tianyuan Cave, China*
1587 (Texas A & M University Press, 2010)
- 1588 122. McCown, T.D., Keith, A. *The Stone Age of Mount Carmel: The Fossil*
1589 *Human Remains from the Levallois-Mousterian, Vol. II.* (Clarendon Press, Oxford,
1590 1939).
- 1591 123. Trinkaus, E., Svoboda, J.A., Wojtal, P., Nyvltova Fisakova, M., Wilczynski, J.
1592 Human remains from the Moravian Gravettian: morphology and taphonomy of
1593 additional elements from Dolni Vestonice II and Pavlov 1. *Int. J. Osteoarchaeol.* **20**,
1594 645-669 (2010).
- 1595 124. Trinkaus, E., Bailey, S.E., Zilhao, J. Upper Paleolithic human remains from
1596 the Gruta do Caldeirao, Tomar, Portugal. *Revista Portuguesa de Arquelologia* **4**, 5-17
1597 (2001).
- 1598
1599
1600
1601
1602
1603
1604

1605 **Supplementary Table 1.** Calliper measurements of AW-1 phalanx following measurement
 1606 scheme of Horwitz and colleagues¹¹¹, proximal radio-ulnar maximum breadth following¹¹².
 1607

Measurement	Measurement no. ¹¹¹	Value (mm)	Notes
Maximum length	1	32.25	
Inter-articular length	2	30.21	
Midshaft dorso-palmar breadth	3	6.25	Measured just distal to the pathology, which lies across midshaft (actual measurement location at <1mm distal to true midshaft).
Midshaft radio-ulnar breadth	4	8.53	
Proximal joint surface dorso-palmar height	5	8.03	Proximal joint surface damaged, estimate.
Proximal joint surface radio-ulnar breadth	6	11.92	
Proximal radio-ulnar maximum breadth	n/a	14.98	
Distal joint surface dorso-palmar height	7	5.25	
Distal joint surface radio-ulnar breadth	8	8.72	Distal joint surface incomplete, estimate.
Midshaft circumference	9	14	

1608

1609 **Supplementary Table 2. Comparative sample for linear metric analysis of Al Wusta-1 intermediate phalanx.**

Taxon	Specimen	IP ray	total sample	Source of data
<i>A. afarensis</i>	AL 333x-18	IP2-4	n=5	measured directly from fossils by TLK
	AL 333-32	IP2-4		
	AL 333-46	IP2-4		
	AL 333-88	IP2-4		
	AL 333-149	IP2-4		
<i>A. africanus</i>	StW 331	IP2-4	n=1	measured directly from fossils by TLK
<i>A. sediba</i>	MH2	IP3, IP4	n=2	measured directly from fossils by TLK
Swartkrans (<i>A. robustus</i> /early <i>Homo</i>)	SKX 13476	IP2-4	n=6	measured directly from fossils by TLK
	SKX 5019	IP2-4		
	SKX 5021	IP2-4		
	SKX 9449	IP2-4		
	SKX 36712	IP2-4		
	SKX 35439	IP2-4		
<i>H. antecessor</i>	ATD6-28	IP3-4	n=2	published values from Lorenzo et al. ¹¹²
	ATD6-53	IP3-4		
<i>H. naledi</i>	Hand 1	IP2, IP3, IP4	n=5	measured directly from fossils by TLK
	UW 101-1646	IP3		
	UW 101-1647	IP4		
<i>H. floresiensis</i>	LB6/9	IP?	n=2	published values from Larson et al. ¹¹³
	LB1/48	IP?		
<i>H. neanderthalensis</i>	Amud 1	IP2, IP3?	min. n=12 individuals n=27 IPs	measured directly from fossils by TLK
	Kebara 2	IP2, IP3, IP4		
	Tabun 1	IP2, IP4?		
	Moula Guercy M-G1-154	IP2-4		
	Spy 430a	IP3		
				published values from Mersey et al. ¹¹⁴
				published values from Semal et al. ¹¹⁵

	Spy 390a	IP3		
	Spy 484a	IP4		
	Shanidar 3	IP3, IP4		published values from Trinkaus ¹¹⁶
	Shanidar 4	IP2, IP3, IP4		
	Shanidar 5	IP3, IP4		
	Shanidar 6	IP3		
	Krapina 205.1	IP3-4		published values from Trinkaus ¹¹⁷
	Krapina 205.2	IP3-4		
	Krapina 205.3	IP3-4		
	Krapina 205.4	IP3-4		
	Krapina 205.5	IP3-4		
	Krapina 205.6	IP3-4		
	Krapina 205.7	IP3-4		
	Krapina 205.8	IP3-4		
	Krapina 205.10	IP2		
	Krapina 205.12	IP3-4		
	Krapina 205.13	IP3-4		
	Krapina 205.14	IP2		
	Krapina 205.15	IP2		
	Krapina 205.17	IP2		
	Krapina 205.18	IP2		
<hr/>				
early <i>H. sapiens</i>	Dolni Vestonice 3	IP2-3	n=17 individuals	published values from Sladek et al. ¹¹⁸
	Dolni Vestonice 13	IP2-3, IP4	n=33 IPs	
	Dolni Vestonice 14	IP3		
	Dolni Vestonice 15	IP2, IP3		
	Dolni Vestonice 16	IP2, IP3, IP4		
	Dolni Vestonice 34	IP2-3		
	Ohalo II H2	IP2, IP3, IP4		measured directly from fossils by TLK
	Qafzeh 9	IP2		measured directly from fossils by TLK
	Qafzeh 8	IP2, IP3, IP4		measured directly from fossils by TLK
	Barma Grande 2	IP3, IP4		measured directly from fossils by NBS

Arene Candide 2	IP2, IP3, IP4		measured directly from fossils by NBS
Sunguir 1	IP2, IP3, IP4, IP5		published values in Trinkaus et al. ¹¹⁹
Tianyuan 1	IP2?		published values in Shang and Trinkaus ¹²⁰
Skhul IV	IP3, IP4, IP5		published values in McCown and Keith ¹²¹
Pavlov 33	IP?		published values in Trinkaus et al. ¹²²
Caldeirao 9	IP2-4		published values in Trinkaus et al. ¹²³
Cueva Victoria CV-0*	IP2		published values in Martinez-Navarro et al. ¹
recent <i>H. sapiens</i>	IP2-4	n=22 individuals	measured directly from specimens by TLK
<i>Pan (P. troglodytes & P. paniscus)</i>	IP2-5	n=67 IPs	
		n=8 individuals	measured directly from specimens by TLK
		n=34 IPs	
<i>Gorilla (G. gorilla & G. beringei)</i>	IP2-5	n=8 individuals	measured directly from specimens by TLK
		n=34 IPs	
Cercopithecids	IP2-5	n=11 IPs	measured directly from specimens by TLK

1610

1611 *The taxonomic association of this specimen with *H. sapiens* is questionable^{1,2}

1612

1613

1614

1615

1616

1617

1618

1619

1620 **Supplementary Table 3. Results from Mann-Whitney U pairwise comparisons with Bonferroni correction ($\alpha = 0.003$) of all shape ratios**
 1621 **(i.e. divided by the total length of the phalanx).** All breadth measurements in are radio-ulnar dimensions and all height measurements are
 1622 dorsopalmar dimensions. All significant pairwise comparisons are in bold text.

			Cercopiths	Gorilla	Pan	Neandertal	early <i>H. sapiens</i>	<i>H. sapiens</i>
base breadth	above	Cercopiths	x	0.007	0.000	0.079	0.110	0.018
prox. articular breadth	below	Gorilla	0.001	x	0.000	0.000	0.133	0.869
		Pan	0.000	0.000	x	0.000	0.000	0.000
		Neandertal	0.196	0.000	0.000	x	0.000	0.000
		early <i>H. sapiens</i>	0.130	0.009	0.000	0.001	x	0.125
		<i>H. sapiens</i>	0.033	0.022	0.000	0.000	0.368	x
prox. shaft breadth	above	Cercopiths	x	0.001	0.000	0.000	0.000	0.000
midshaft breadth	below	Gorilla	0.526	x	0.000	0.180	0.000	0.481
		Pan	0.000	0.000	x	0.123	0.011	0.000
		Neandertal	0.886	0.418	0.000	x	0.011	0.404
		early <i>H. sapiens</i>	0.088	0.052	0.000	0.009	x	0.000
		<i>H. sapiens</i>	0.001	0.000	0.000	0.000	0.000	x
midshaft height	above	Cercopiths	x	0.000	0.000	0.866	0.014	0.000
distal shaft breadth	below	Gorilla	0.032	x	0.000	0.000	0.001	0.000
		Pan	0.000	0.000	x	0.000	0.000	0.000
		Neandertal	0.048	0.356	0.076	x	0.005	0.000
		early <i>H. sapiens</i>	0.000	0.000	0.002	0.003	x	0.359
		<i>H. sapiens</i>	0.005	0.625	0.000	0.481	0.000	x
distal shaft height	above	Cercopiths	x	0.000	0.000	0.004	0.000	0.020
prox. articular height	below	Gorilla	0.200	x	0.000	0.640	0.002	0.000
		Pan	0.000	0.000	x	0.087	0.010	0.000
		Neandertal	0.988	0.164	0.000	x	0.026	0.043
		early <i>H. sapiens</i>	0.318	0.885	0.000	0.120	x	0.000
		<i>H. sapiens</i>	0.217	0.674	0.000	0.083	0.876	x

1623

1624 **Supplementary Table 4. Landmarks used in geometric morphometric analyses of AI**

1625 **Wusta-1 phalanx and the comparative samples.**

Landmark	Description
1	Mid-point of distal articulation (distal view, dorsal up)
2	Furthest left point on distal head (dorsal view)
3	Furthest right point on distal head (dorsal view)
4	Furthest proximal point on midline of proximal articulation (proximal view, dorsal up)
5	Mid-point of ridge between two articulations on proximal face (proximal view, dorsal up)
6	Furthest left point on proximal base (dorsal view)
7	Furthest right point on proximal base (dorsal view)
8	Deepest point on left proximal articulation (proximal view, dorsal up)
9	Deepest point on right proximal articulation (proximal view, dorsal up)
10	Centre of trochlea
11	Place where triangular raised region merges with central ridge on proximal palmar surface (palmar view)
12	Most dorsal point on proximal base (dorsal view)
13	Most palmar point of left proximal articulation (proximal view, dorsal up)
14	Most palmar point of right proximal base (proximal view, dorsal up)
15	Furthest point left of the distal trochlea (palmar view)
16	Furthest left point of the proximal articular surface (proximal view, dorsal up)
17	Furthest right point of the proximal articular surface (proximal view, dorsal up)
18	Most palmar point at the mid-line of the proximal articular surface (proximal view, dorsal up)

1626

1627 **Supplementary Table 5. Sample used in comparative primate geometric morphometric**

1628 **analyses.**

1629

1630 Institutions: Duckworth: Duckworth Collection, University of Cambridge; NHM Vienna: Vienna Natural

1631 History Museum; Uni. of Florence: University of Florence; GAUG: Johann-Friedrich-Blumenbach-Institut für

1632 Zoologie und Anthropologie der Georg-August-Universität Göttingen; Uni. of Kent: University of Kent; Tel

1633 Aviv Uni.: Tel Aviv University; MPNBR: Museo Preistorico Nazionale dei Balzi Rossi, Italy; MAF: Museo

1634 Archeologico del Finale, Italy; NHM: Natural History Museum, London; MRAC: Musée Royal de l'Afrique

1635 Centrale, Tervuren; MPI-EVA: Max Planck Institute, Leipzig; Powell Cotton: Powell Cotton Collection.

1636

Group	Sample number	Institution
Al Wusta	1	
<i>Colobus badius preussi</i> total	7	Powell Cotton
<i>Gorilla gorilla</i> total	20	Powell Cotton
<i>Mandrillus leucophaeus</i>	4	Powell Cotton
<i>Mandrillus sphinx</i>	2	Powell Cotton
<i>Mandrillus</i> total	6	
<i>Pan paniscus</i>	4	MRAC Powell Cotton, MPI- EVA
<i>Pan troglodytes</i>	4	
<i>Pan</i> total	8	
<i>Papio anubis neumanni</i> total	4	
Krapina	17	NESPOS
Regourdou	3	NESPOS
Kebara 2	3	Tel Aviv Uni.
Tabun C1	2	NHM
Neanderthal total	25	
Qafzeh	4	Tel Aviv Uni.
Ohalo	3	Tel Aviv Uni.
Barma Grande	2	MPNBR
Arene Candide	3	MAF
Early <i>H. sapiens</i> total	12	
Australian	3	Duckworth
Inuit	1	Duckworth
Kerma	3	Duckworth
Maiden Castle	3	Duckworth
Egyptian Nubian	19	NHM Vienna
Fuegian	3	Uni. of Florence
Siracusian	5	Uni. of Florence
German	13	GAUG
Canterbury	11	Uni. of Kent
Holocene <i>H. sapiens</i> total	61	

1637

1638 **Supplementary Table 6. Procrustes distances from primate and hominin mean shapes**
1639 **to Al Wusta-1.**

1640

Mean Shape	Distance to AW-1
Holocene <i>H. sapiens</i>	0.080184
Early <i>H. sapiens</i>	0.084209
<i>Mandrillus</i>	0.093510
<i>Gorilla</i>	0.101452
<i>Papio</i>	0.106864
<i>H. neanderthalensis</i>	0.119294
<i>Pan</i>	0.119404
<i>Colobus</i>	0.150987

1641

1642

1643

1644

1645

1646

1647

1648

1649

1650

1651

1652

1653

1654 **Supplementary Table 7. Details of the comparative sample of intermediate phalanges**
 1655 **from Neanderthals and Pleistocene and Holocene *Homo sapiens* used for geometric**
 1656 **morphometric analyses of known side and digit, and cross sectional geometric analyses.**

1657 Institutions: Duckworth: Duckworth Collection, University of Cambridge; NHM Vienna: Vienna Natural
 1658 History Museum; Uni of Florence: University of Florence; GAUG: Johann-Friedrich-Blumenbach-Institut für
 1659 Zoologie und Anthropologie der Georg-August-Universität Göttingen; Uni of Kent: University of Kent; Tel
 1660 Aviv Uni: Tel Aviv University; MPNBR: Museo Preistorico Nazionale dei Balzi Rossi, Italy; MAF: Museo
 1661 Archeologico del Finale, Italy; NHM: Natural History Museum, London.

1662

Group	Specimen/Group	Institution	Lefts (n)			Rights (n)			Sample total
			2nd	3rd	4th	2nd	3rd	4th	
Holocene <i>H. sapiens</i>	Australian	Duckworth		1		1	1	2	5
Holocene <i>H. sapiens</i>	Kerma	Duckworth	1	1				1	3
Holocene <i>H. sapiens</i>	Inuit	Duckworth		1			1		2
Holocene <i>H. sapiens</i>	Maiden Castle	Duckworth		1		1		1	3
Holocene <i>H. sapiens</i>	Egyptian	NHM Vienna	2		2	5	6	4	19
	Nubian								
Holocene <i>H. sapiens</i>	Fuegian	Uni of Florence	1		1	1	1		4
Holocene <i>H. sapiens</i>	Siracusan	Uni of Florence	2	1	1	2	1	2	9
Holocene <i>H. sapiens</i>	German	GAUG	1	2	2	3	3	2	13
Holocene <i>H. sapiens</i>	Canterbury	Uni of Kent	1	1	2	2	3	2	11
Pleistocene <i>H. sapiens</i>	Ohalo 2	Tel Aviv Uni	1		1				2
Pleistocene <i>H. sapiens</i>	Qafzeh 8	Tel Aviv Uni	1	1	1	1	1	1	6
Pleistocene <i>H. sapiens</i>	Qafzeh 9	Tel Aviv Uni	1			1	1		3
Pleistocene <i>H. sapiens</i>	Barma Grande 2	MPNBR		1	1		1	1	4
Pleistocene <i>H. sapiens</i>	Arene Candide	MAF	1	1	1	1	1	1	6
	2								
Neanderthal	Kebara 2	Tel Aviv Uni	1	1	1	1		1	5
Neanderthal	Tabun C1	NHM	1		1				2
Total			14	12	14	19	20	18	91

1663

1664

1665 **Supplementary Table 8. Procrustes Distances between Al Wusta-1 and other hominin**
 1666 **groups with sides pooled.**

1667

	Holocene <i>H.</i>	Pleistocene <i>H.</i>	
	<i>sapiens</i>	<i>sapiens</i>	Neanderthal
AW-1	0.078	0.084	0.099

1668

1669

1670

1671

1672

1673 **Supplementary Table 9. Procrustes distances between Al Wusta-1 and its nearest**

1674 **neighbours with sides pooled. Specimen numbers refer to Figure 2.**

1675

Nearest neighbour	Side	Ray	Procrustes	
			Distance	
1) Maiden Castle EU.1.3.70_Sk20	Left	3 rd	0.084	
2) Egyptian NHMW K24_2	Right	3 rd	0.061	
3) Canterbury NGB_89_Sk15_1247	Left	3 rd	0.072	

1676

1677

1678

1679

1680

1681

1682 **Supplementary Table 10. Procrustes distances between Al Wusta-1 and comparative**
 1683 **groups and ray numbers across groups, analysing left and right hands separately.**

Phalanx side	Holocene <i>H.</i>	Pleistocene <i>H.</i>	
	<i>sapiens</i>	<i>sapiens</i>	Neanderthals
Right	0.080	0.090	0.119
Left	0.076	0.081	0.098
	2nd Ray	3rd Ray	4th Ray
Right	0.095	0.076	0.083
Left	0.092	0.068	0.084

1684

1685

1686

1687

1688

1689

1690 **Supplementary Table 11. Procrustes distances between Al Wusta-1 and its nearest**
 1691 **neighbours, analysing left and right hands separately.**

Nearest neighbour	Side	Ray	Procrustes
			Distance
Egyptian NHMW K24 3 HP3MR	Right	3 rd	0.061
Canterbury NGB 89 Sk15 1247 HP3ML	Left	3 rd	0.072

1692

1693

1694

1695

1696 **Supplementary Table 12. U-series results on Al Wusta-1.** All errors are 2- σ . Individual
 1697 results do not contain errors of standard measurement (correlated errors), mean values
 1698 incorporate errors of standard.
 1699

3675#1	U	Th	U/T	²³⁰ Th/ ²³⁸ U	²³⁰ Th/ ²³⁸ U	²³⁴ U/ ²³⁸ U	²³⁴ U/ ²³⁸ U	Age	Age error
	(ppm)	(ppb)	h	U	error	U	error	(ka)	(ka)
1	49.99	16	307	0.7293	0.0066	1.6887	0.0053	59.1	0.7
2	48.60	11	425	0.7310	0.0085	1.6817	0.0046	59.6	0.9
3	46.10	14	339	0.7537	0.0052	1.6798	0.0045	62.1	0.6
4	43.85	16	270	0.7724	0.0061	1.6899	0.0073	63.6	0.7
5	34.79	226	154	0.7744	0.0063	1.6801	0.0048	64.3	0.7
6	23.25	290	80	0.7950	0.0107	1.6829	0.0130	66.4	1.4
7	19.12	166	115	0.7851	0.0094	1.6861	0.0051	65.2	1.1
8	15.34	118	131	0.7791	0.0109	1.6895	0.0107	64.4	1.3
9	14.22	106	135	0.7522	0.0088	1.6807	0.0092	61.9	1.0
10	14.65	129	114	0.7574	0.0093	1.6882	0.0173	62.1	1.3
11	15.29	100	152	0.7622	0.0084	1.6794	0.0101	63.1	1.0
12	14.58	89	164	0.7559	0.0082	1.6895	0.0074	61.9	0.9
13	12.02	81	148	0.7474	0.0089	1.6828	0.0099	61.3	1.1
14	10.84	69	157	0.7516	0.0102	1.6798	0.0106	61.9	1.2
15	11.08	54	207	0.7598	0.0103	1.6808	0.0118	62.7	1.3
16	11.22	48	235	0.7585	0.0115	1.6772	0.0106	62.8	1.3
17	11.20	47	240	0.7558	0.0111	1.6871	0.0104	62.0	1.3
18	10.85	58	188	0.7606	0.0107	1.6933	0.0090	62.2	1.2
19	10.08	48	211	0.7558	0.0135	1.6884	0.0104	61.9	1.5
20	9.01	51	177	0.7572	0.0119	1.6952	0.0093	61.7	1.3
21	7.81	70	111	0.7489	0.0133	1.6825	0.0098	61.5	1.5
22	7.30	80	92	0.7311	0.0123	1.6858	0.0116	59.5	1.4
23	6.57	72	91	0.7275	0.0124	1.6769	0.0088	59.5	1.4
24	6.27	65	96	0.7251	0.0161	1.6833	0.0093	59.0	1.7
25	6.19	67	92	0.7361	0.0120	1.6666	0.0159	60.9	1.5
26	5.34	68	78	0.7338	0.0216	1.6691	0.0154	60.6	2.4
27	5.33	61	87	0.7405	0.0132	1.6833	0.0150	60.6	1.6
28	5.55	51	109	0.7351	0.0107	1.6971	0.0165	59.3	1.3
29	5.63	46	124	0.7527	0.0136	1.6880	0.0109	61.6	1.5
30	5.28	37	143	0.7333	0.0169	1.6821	0.0168	59.9	1.9
MEAN VALUES									
1-30				0.7547	0.0129	1.6843	0.0152	62.0	1.6

1700

3675#2	U	Th	U/Th	²³⁰ Th/ ²³⁸ U	²³⁰ Th/ ²³⁸ U	²³⁴ U/ ²³⁸ U	²³⁴ U/ ²³⁸ U	Age	Age error
	(ppm)	(ppb)	U/Th	U	error	U	error	(ka)	(ka)
1	57.79	16	3687	0.5955	0.0200	1.6802	0.0107	46.3	1.9
2	57.29	9	6263	0.6742	0.0066	1.6675	0.0068	54.5	0.7
3	53.84	7	8207	0.7077	0.0114	1.6700	0.0061	57.8	1.2
4	47.64	5	9152	0.7705	0.0068	1.6852	0.0127	63.7	1.0
5	45.61	5	9414	0.7969	0.0088	1.6784	0.0077	66.9	1.1
6	42.56	4	1079	0.7910	0.0122	1.6714	0.0172	66.6	1.7
7	40.59	3	1267	0.7948	0.0084	1.6845	0.0094	66.3	1.1
8	38.07	2	1570	0.7810	0.0075	1.6844	0.0088	64.8	0.9
9	37.47	2	1760	0.7814	0.0125	1.6748	0.0196	65.4	1.7
10	37.71	2	1541	0.7671	0.0079	1.6749	0.0174	63.8	1.2
11	33.73	2	1364	0.7640	0.0067	1.6755	0.0094	63.5	0.9
12	30.04	3	1166	0.7767	0.0112	1.6806	0.0097	64.6	1.3
13	30.55	3	1109	0.7883	0.0082	1.6952	0.0125	65.1	1.1
14	29.63	3	1097	0.7787	0.0085	1.6844	0.0086	64.6	1.0
15	23.02	22	1060	0.7867	0.0099	1.6800	0.0076	65.7	1.2
16	17.81	33	540	0.8032	0.0098	1.6839	0.0093	67.3	1.2
17	14.64	22	660	0.8113	0.0091	1.6941	0.0118	67.6	1.2
18	12.94	30	425	0.7987	0.0076	1.6783	0.0112	67.1	1.0
19	10.54	39	272	0.7877	0.0106	1.6873	0.0097	65.4	1.3
20	8.24	48	171	0.7746	0.0125	1.6877	0.0069	64.0	1.4
21	6.20	61	102	0.7546	0.0143	1.6917	0.0102	61.6	1.6
22	5.00	31	160	0.7692	0.0162	1.6939	0.0166	63.1	1.9

23	4.40	17	256	0.7668	0.0163	1.6926	0.0146	62.9	1.9
24	3.90	12	319	0.7495	0.0165	1.6929	0.0151	61.0	1.9
25	3.57	11	329	0.7547	0.0183	1.6891	0.0145	61.8	2.1
26	2.97	10	296	0.7577	0.0177	1.6826	0.0146	62.4	2.0
27	2.63	9	282	0.7240	0.0209	1.6951	0.0197	58.3	2.3
28	2.34	8	299	0.6894	0.0234	1.6955	0.0151	54.8	2.4
29	2.16	7	300	0.6274	0.0259	1.6883	0.0174	49.0	2.6
30	1.85	6	331	0.6463	0.0358	1.6758	0.0322	51.3	3.7
MEAN VALUES									
5-26				0.7837	0.0135	1.6814	0.0154	65.3	1.7

1701

3675#3	U	Th	U/Th	²³⁰ Th/ ²³⁸ U	²³⁰ Th/ ²³⁸ U	²³⁴ U/ ²³⁸ U	²³⁴ U/ ²³⁸ U	Age	Age error
	(ppm)	(ppb)		U	error	U	error	(ka)	(ka)
1	58.44	18	3325	0.6462	0.0124	1.6700	0.0073	51.6	1.3
2	56.93	8	7353	0.6569	0.0049	1.6696	0.0153	52.6	0.8
3	55.96	6	9673	0.6594	0.0066	1.6702	0.0096	52.9	0.8
4	47.14	5	9675	0.6976	0.0087	1.6696	0.0108	56.7	1.0
5	41.59	35	1201	0.7572	0.0132	1.6680	0.0139	63.1	1.6
6	37.40	11	3388	0.8065	0.0132	1.6908	0.0192	67.3	1.8
7	38.25	7	5596	0.7945	0.0094	1.6807	0.0074	66.5	1.1
8	38.32	5	7199	0.7931	0.0102	1.6773	0.0157	66.5	1.4
9	38.60	5	8198	0.8012	0.0106	1.6876	0.0156	66.9	1.4
10	37.61	2	1640	0.7850	0.0062	1.6900	0.0124	65.0	0.9
11	35.79	3	1383	0.7851	0.0086	1.6803	0.0087	65.5	1.0
12	35.59	2	1452	0.7800	0.0088	1.6783	0.0102	65.1	1.1
13	36.60	2	1522	0.7671	0.0057	1.6745	0.0088	63.8	0.8
14	32.65	2	1478	0.7566	0.0063	1.6792	0.0075	62.5	0.8
15	30.15	3	1155	0.7659	0.0103	1.6884	0.0125	63.0	1.3
16	27.97	3	1025	0.7703	0.0085	1.6835	0.0129	63.7	1.1
17	25.75	4	6415	0.7698	0.0120	1.6816	0.0171	63.8	1.6
18	24.69	3	8744	0.7781	0.0090	1.6691	0.0107	65.3	1.1
19	22.23	3	8589	0.7997	0.0127	1.6868	0.0087	66.8	1.5
20	19.33	3	6449	0.8015	0.0108	1.6820	0.0131	67.2	1.4
21	14.70	10	1482	0.7975	0.0083	1.6827	0.0059	66.7	1.0
22	8.99	19	471	0.7862	0.0162	1.6855	0.0115	65.3	1.9
23	5.23	11	497	0.7627	0.0172	1.6863	0.0158	62.8	2.0
24	5.05	6	827	0.7796	0.0105	1.7064	0.0110	63.5	1.2
25	5.18	8	667	0.7626	0.0118	1.6977	0.0141	62.2	1.4
26	5.43	8	653	0.7599	0.0196	1.6880	0.0132	62.4	2.2
27	5.14	5	1090	0.7318	0.0161	1.6956	0.0179	59.1	1.9
28	4.91	4	1297	0.7474	0.0144	1.6741	0.0193	61.7	1.8
29	4.70	3	1664	0.7497	0.0153	1.6738	0.0139	62.0	1.8
30	4.32	2	1859	0.7433	0.0144	1.6836	0.0160	60.8	1.7
MEAN VALUES									
5-30				0.7821	0.0135	1.6827	0.0154	65.0	1.7

1702

3675#4	U	Th	U/Th	²³⁰ Th/ ²³⁸ U	²³⁰ Th/ ²³⁸ U	²³⁴ U/ ²³⁸ U	²³⁴ U/ ²³⁸ U	Age	Age error
	(ppm)	(ppb)		U	error	U	error	(ka)	(ka)
1	59.50	39	1524	0.6319	0.0102	1.6640	0.0054	50.4	1.0
2	61.70	14	4513	0.6370	0.0064	1.6770	0.0311	50.4	1.3
3	55.83	9	6523	0.6833	0.0087	1.6684	0.0049	55.3	0.9
4	46.15	6	8275	0.7477	0.0088	1.6755	0.0096	61.7	1.1
5	40.88	6	6811	0.8026	0.0100	1.6834	0.0081	67.3	1.2
6	37.30	5	6899	0.8437	0.0085	1.6773	0.0067	72.3	1.1
7	35.26	3	1049	0.8453	0.0054	1.6879	0.0048	71.8	0.7
8	36.35	3	1420	0.8305	0.0077	1.6833	0.0067	70.4	1.0
9	35.68	3	1253	0.8276	0.0079	1.6798	0.0080	70.3	1.0
10	33.76	2	1598	0.8366	0.0057	1.6846	0.0066	71.0	0.8
11	33.52	2	1678	0.8263	0.0069	1.6815	0.0104	70.0	1.0
12	32.93	2	1780	0.8117	0.0072	1.6814	0.0039	68.4	0.8
13	32.85	2	2134	0.8043	0.0070	1.6824	0.0086	67.5	0.9
14	31.36	2	1722	0.7961	0.0074	1.6893	0.0078	66.2	0.9

15	29.38	2	1603	0.7894	0.0074	1.6852	0.0093	65.7	1.0
16	28.26	1	1957	0.7801	0.0083	1.6719	0.0087	65.4	1.0
17	26.76	2	1245	0.7734	0.0080	1.6847	0.0066	64.0	0.9
18	24.71	2	1468	0.7655	0.0083	1.6735	0.0099	63.7	1.0
19	23.88	2	1269	0.7582	0.0097	1.6864	0.0156	62.3	1.3
20	22.21	7	3326	0.7556	0.0095	1.6836	0.0122	62.1	1.2
21	12.10	13	896	0.7489	0.0105	1.6782	0.0087	61.7	1.2
22	8.43	8	1063	0.7651	0.0101	1.6788	0.0119	63.4	1.2
23	7.16	5	1313	0.7567	0.0115	1.6846	0.0139	62.2	1.4
24	6.07	7	897	0.7675	0.0137	1.6901	0.0140	63.1	1.6
25	4.01	7	563	0.7555	0.0175	1.6847	0.0138	62.1	2.0
26	3.58	4	845	0.7533	0.0170	1.6764	0.0173	62.3	2.0
27	3.27	4	821	0.7348	0.0249	1.6763	0.0192	60.3	2.8
28	2.97	3	1072	0.7227	0.0224	1.6744	0.0174	59.1	2.5
29	2.59	2	1655	0.7398	0.0209	1.6773	0.0148	60.8	2.3
30	2.21	2	1242	0.7129	0.0255	1.6696	0.0139	58.3	2.7
MEAN VALUES									
5-30				0.8017	0.0137	1.6820	0.0152	67.2	1.7

1703

3675#5	U	Th	U/Th	²³⁰ Th/ ²³⁸ U	²³⁰ Th/ ²³⁸ U	²³⁴ U/ ²³⁸ U	²³⁴ U/ ²³⁸ U	Age	Age error
	(ppm)	(ppb)		U	error	U	error	(ka)	(ka)
1	74.45	19	3962	0.5473	0.0042	1.6540	0.0049	42.7	0.4
2	68.19	8	8411	0.5574	0.0083	1.6487	0.0099	43.8	0.8
3	56.73	6	9114	0.6294	0.0134	1.6630	0.0063	50.2	1.3
4	47.30	6	7446	0.6985	0.0155	1.6621	0.0083	57.2	1.6
5	42.32	4	1050	0.7863	0.0120	1.6734	0.0149	66.0	1.6
6	38.37	3	1119	0.8324	0.0086	1.6852	0.0112	70.5	1.2
7	35.55	2	1465	0.8375	0.0101	1.6859	0.0067	71.0	1.2
8	33.52	2	1625	0.8548	0.0093	1.6904	0.0107	72.7	1.3
9	33.30	3	1090	0.8778	0.0072	1.6882	0.0107	75.5	1.1
10	32.28	2	1476	0.8746	0.0062	1.6817	0.0094	75.6	1.0
11	33.75	2	1990	0.8530	0.0068	1.6894	0.0165	72.6	1.3
12	32.58	2	2007	0.8570	0.0077	1.6872	0.0078	73.2	1.0
13	30.24	1	2053	0.8603	0.0106	1.6888	0.0099	73.5	1.4
14	27.27	2	1585	0.8684	0.0082	1.6860	0.0068	74.6	1.1
15	25.94	2	1567	0.8557	0.0082	1.6852	0.0112	73.2	1.2
16	24.93	1	2556	0.8451	0.0130	1.6847	0.0118	72.0	1.7
17	24.91	1	2502	0.8222	0.0100	1.6866	0.0063	69.3	1.2
18	23.05	1	3626	0.8358	0.0113	1.6888	0.0117	70.7	1.5
19	21.56	1	2173	0.8262	0.0080	1.6915	0.0091	69.4	1.0
20	20.31	1	1552	0.8322	0.0095	1.6917	0.0167	70.1	1.4
21	19.72	1	2411	0.8187	0.0146	1.7064	0.0278	67.7	2.2
22	19.69	1	2830	0.8080	0.0074	1.6861	0.0113	67.7	1.0
23	18.82	1	3367	0.8073	0.0079	1.6746	0.0132	68.3	1.2
24	18.26	1	1927	0.8028	0.0075	1.6792	0.0105	67.5	1.0
25	17.53	1	2329	0.8008	0.0102	1.6882	0.0064	66.8	1.2
26	16.43	1	1982	0.8079	0.0103	1.6917	0.0077	67.4	1.2
27	14.39	1	1501	0.8072	0.0094	1.6860	0.0132	67.6	1.3
28	10.81	1	8682	0.8119	0.0101	1.6874	0.0129	68.1	1.3
29	9.63	1	6644	0.8100	0.0107	1.6954	0.0113	67.4	1.3
30	9.14	1	8014	0.8081	0.0137	1.6825	0.0139	67.9	1.7
MEAN VALUES									
6-30				0.8392	0.0144	1.6874	0.0153	71.1	1.9

1704

3675#6	U	Th	U/Th	²³⁰ Th/ ²³⁸ U	²³⁰ Th/ ²³⁸ U	²³⁴ U/ ²³⁸ U	²³⁴ U/ ²³⁸ U	Age	Age error
	(ppm)	(ppb)		U	error	U	error	(ka)	(ka)
1	76.83	11	7262	0.4753	0.0142	1.6530	0.0051	36.2	1.3
2	67.12	6	1086	0.5164	0.0068	1.6578	0.0123	39.7	0.7
3	63.03	7	9262	0.5360	0.0068	1.6572	0.0039	41.5	0.6
4	53.40	6	9030	0.6315	0.0155	1.6663	0.0084	50.3	1.6
5	47.14	4	1266	0.7257	0.0141	1.6735	0.0110	59.5	1.6
6	42.65	3	1293	0.7690	0.0090	1.6757	0.0050	64.0	1.0

7	40.02	3	1340	0.8297	0.0122	1.6803	0.0178	70.5	1.7
8	38.80	2	1670	0.8562	0.0078	1.6840	0.0100	73.3	1.1
9	36.41	2	2159	0.8708	0.0134	1.6868	0.0158	74.8	1.9
10	35.03	2	1790	0.8810	0.0087	1.6841	0.0106	76.2	1.2
11	34.68	2	1756	0.8966	0.0128	1.6925	0.0148	77.5	1.8
12	33.32	2	1818	0.9060	0.0089	1.6809	0.0091	79.4	1.3
13	30.97	2	1775	0.9079	0.0085	1.6863	0.0109	79.3	1.3
14	28.12	2	1582	0.8927	0.0089	1.6786	0.0083	78.0	1.2
15	25.78	2	1359	0.8953	0.0098	1.6778	0.0098	78.3	1.4
16	23.78	1	1965	0.8768	0.0109	1.6750	0.0130	76.3	1.6
17	21.87	1	2389	0.8852	0.0132	1.6860	0.0115	76.6	1.7
18	20.16	1	2144	0.8767	0.0125	1.6867	0.0105	75.5	1.6
19	19.88	1	2676	0.8574	0.0109	1.6881	0.0119	73.2	1.5
20	18.92	1	2179	0.8605	0.0097	1.6928	0.0105	73.2	1.3
21	17.80	1	1407	0.8454	0.0062	1.6846	0.0087	72.0	0.9
22	16.52	1	1433	0.8354	0.0126	1.6931	0.0158	70.4	1.7
23	16.42	1	2041	0.8389	0.0125	1.6902	0.0100	70.9	1.5
24	13.49	1	1810	0.8522	0.0131	1.6874	0.0123	72.6	1.7
25	12.28	1	1640	0.8742	0.0148	1.6841	0.0112	75.4	1.9
26	12.87	1	1602	0.8535	0.0161	1.7026	0.0164	71.9	2.1
27	11.94	1	8285	0.8409	0.0082	1.6995	0.0103	70.6	1.1
28	9.69	2	5389	0.8488	0.0108	1.6870	0.0103	72.2	1.4
29	8.40	2	4912	0.8500	0.0137	1.6845	0.0140	72.5	1.8
30	7.84	1	7437	0.8594	0.0136	1.6788	0.0122	74.0	1.8
MEAN VALUES									
5-30				0.8739	0.0150	1.6859	0.0154	75.2	2.0

1705

3675#7	U	Th	U/Th	²³⁰ Th/ ²³⁸ U	²³⁰ Th/ ²³⁸ U	²³⁴ U/ ²³⁸ U	²³⁴ U/ ²³⁸ U	Age	Age error
	(ppm)	(ppb)		U	error	U	error	(ka)	(ka)
1	121.03	24	5024	0.3769	0.0033	1.6413	0.0025	28.0	0.3
2	115.97	15	7838	0.3748	0.0040	1.6423	0.0033	27.8	0.3
3	108.17	10	1073	0.4193	0.0081	1.6487	0.0030	31.4	0.7
4	86.57	9	9184	0.4735	0.0067	1.6484	0.0031	36.1	0.6
5	71.74	10	6855	0.5251	0.0146	1.6540	0.0038	40.6	1.3
6	57.44	13	4434	0.6336	0.0108	1.6660	0.0045	50.5	1.1
7	50.64	91	554	0.6722	0.0060	1.6690	0.0056	54.2	0.6
8	47.15	517	91	0.6413	0.0102	1.6627	0.0040	51.4	1.0
9	43.06	307	140	0.6922	0.0108	1.6750	0.0103	55.9	1.2
10	39.06	133	295	0.7215	0.0081	1.6787	0.0107	58.8	1.0
11	36.80	67	552	0.7133	0.0051	1.6666	0.0068	58.5	0.6
12	30.29	51	594	0.8452	0.0279	1.6882	0.0095	71.8	3.2
13	28.00	31	895	0.9252	0.0086	1.6917	0.0068	81.0	1.2
14	26.21	23	1162	0.9647	0.0104	1.7002	0.0094	85.3	1.5
15	23.79	17	1392	0.9813	0.0111	1.6944	0.0076	87.9	1.6
16	22.45	19	1199	0.9855	0.0112	1.6979	0.0067	88.1	1.5
17	21.92	22	982	0.9827	0.0079	1.6945	0.0066	88.0	1.2
18	21.01	17	1246	0.9752	0.0084	1.6878	0.0098	87.6	1.3
19	19.25	22	866	0.9940	0.0088	1.6967	0.0067	89.3	1.3
20	18.50	43	426	0.9641	0.0113	1.6841	0.0127	86.5	1.8
21	17.60	22	801	0.9799	0.0115	1.6883	0.0095	88.2	1.7
22	17.30	30	573	0.9743	0.0093	1.6958	0.0069	86.9	1.3
23	17.07	23	738	0.9737	0.0103	1.6907	0.0068	87.2	1.4
24	16.51	22	765	0.9703	0.0129	1.6869	0.0082	87.0	1.8
25	15.15	14	1054	0.9627	0.0098	1.6961	0.0058	85.4	1.3
26	13.61	8	1714	0.9810	0.0110	1.6945	0.0084	87.8	1.6
27	12.93	10	1267	0.9869	0.0123	1.6882	0.0095	89.1	1.8
28	11.39	19	614	0.9928	0.0109	1.6940	0.0073	89.4	1.5
29	7.08	76	93	0.9768	0.0133	1.6930	0.0112	87.4	1.9
30	5.92	53	112	0.9350	0.0144	1.6934	0.0148	82.1	2.1
MEAN VALUES									
15-30				0.9778	0.0168	1.6923	0.0153	87.6	2.5

1706

1707

1708 **Supplementary Table 13. U-series results on sample WU1601.** All errors are 2- σ .

3672	U (ppm)	Th (ppb)	U/Th	²³⁰ Th/ ²³⁸ U	²³⁰ Th/ ²³⁸ U error	²³⁴ U/ ²³⁸ U	²³⁴ U/ ²³⁸ U error	Age (ka)	Age error (ka)
MEAN VALUES									
Enamel	0.83±0.28			0.8346	0.0533	1.5042	0.0329	83.5	8.1
Dentine	109±6			0.7295	0.0173	1.5742	0.0124	65.0	2.1

1709

1710

1711

1712

1713 **Supplementary Table 14. Combined US-ESR age results obtained for sample WU1601.**

1714 See Methods and Supplementary Information 2 for discussion.

1715

Internal dose rate (μ Gy/a)	Beta dose rate (dentine) (μ Gy/a)	Beta dose rate (sediment) (μ Gy/a)	Gamma dose rate (μ Gy/a)	Cosmic dose rate (μ Gy/a)	Total dose rate (μ Gy/a)	Enamel thickness (μ m)	Removed surface layer (μ m) on each side	D_E (Gy)	p-parameter	US-ESR age (ka)	
241±75	260±48	4±0	180±10	254±25	939±93	3244±100	Ext.: 176±50; Int.:181±50	97.1±1.9	-0.83	-0.53	103±10/-9

1716

1717

1718

1719

1720

1721

1722

1723

1724

1725 **Supplementary Table 15. The number of single grains which were measured, rejected**
 1726 **after application of the criteria outlined in Supplementary section 3.2, and accepted for**
 1727 **inclusion in the calculation of D_e .** Samples indicated (DR) represent dose recovery data.

Sample	PD15 (DR)	PD17 (DR)	PD15	PD17	PD40	PD41
Total number of grains measured						
	2500	2500	3600	3400	2800	3100
Grains rejected for the following reasons						
T_n signal	2358	2363	3373	3223	2606	2951
<3*background						
Poor recycling ratio	11	25	34	21	16	30
Depletion by IR	51	48	79	50	73	55
Recuperation	36	29	58	53	28	17
Oversaturation	3	1	0	5	12	7
$D_e < 2\sigma$ above 0 Gy	0	0	6	6	2	5
Sum of rejected grains						
	2459	2466	3550	3358	2737	3065
Acceptable individual D_e values						
	41	34	50	42	63	35

1728

1729

1730

1731

1732

1733

1734

1735

1736 **Supplementary Table 16. Sample depths, water content and dose rate for Al Wusta**
 1737 **samples.**

Sample	Depth (m)	Moisture (%)	Dose rate (Gy/ka)			Total dose rate, (Gy/ka)
			Beta	Gamma	Cosmic	
PD15	0.95±0.10	5±2.5	0.15±0.01	0.27±0.02	0.209±0.021	0.62±0.03
PD17	0.70±0.10	5±2.5	0.16±0.01	0.24±0.01	0.222±0.022	0.62±0.03
PD40	0.65±0.10	5±2.5	0.10±0.01	0.18±0.01	0.219±0.022	0.50±0.03
PD41	1.20±0.10	5±2.5	0.10±0.01	0.25±0.01	0.198±0.020	0.54±0.03

1738

1739

1740

1741

1742

1743 **Supplementary Table 17. OSL Summary dating results and ages.** Uncertainties in the age
 1744 estimates are based on the propagation, in quadrature, of errors associated with individual
 1745 errors for all measured quantities. In addition to uncertainties calculated from counting
 1746 statistics, errors due to (1) beta source calibration (3 %); (2) single-grain instrument
 1747 reproducibility (1.5 %); (3) dose rate conversion factors (3 %) and attenuation factors (3 %)
 1748 have been included.

1749

Sample	D_b calculation method (n)	D_b (Gy)	OD (%)	Total dose rate, D_r (Gy/ka)	Age (ka)
PD15	CAM (50)	57.4±3.0	22±4	0.62±0.03	92.0±6.3
PD17	CAM (42)	53.0±2.5	16±3	0.62±0.03	85.3±5.6
PD40	CAM (63)	49.6±2.5	26±3	0.50±0.03	98.6±7.0
PD41	CAM (35)	50.2±2.8	20±4	0.54±0.03	92.2±6.8

1750

1751

1752

1753

1754

1755 **Supplementary Table 18. Quantification of bulk mineralogy from XRD data.** Note that
 1756 in all cases calcite makes up at least 85% of the crystalline mineral fraction. Gypsum and
 1757 halite are below the detection limit of the instrumentation except in PD15-30. The absence of
 1758 any saline tolerant diatom species at this level makes it unlikely that halite was precipitating
 1759 in this system and it is more likely that this reflects aeolian dust blown onto the exposure.
 1760 There is no evidence for Halite in any of the thin sections.
 1761

Sample ID	Calcite %	Quartz %	Gypsum %	Halite %
PD15_10	93.9	3.5	1.6	1
PD15_30	92.4	2	0.8	4.7
PD15_40	96.7	1.7	0.7	0.9
PD15_50	97.4	1.8	0.7	0.2
PD16_30	95.9	2.2	1.5	0.3
PD16_40	96.6	1.7	1.4	0.3
PD16_80	97.3	1.4	1.1	0.2
PD17_20	93.8	3.3	1.3	1.6
PD17_30	96.7	1.8	0.9	0.6
PD17_40	87.3	11	0.7	1

1762
 1763
 1764
 1765
 1766
 1767
 1768
 1769

1770 **Supplementary Table 19. Taxonomy of Al Wusta vertebrate fossils.**

1771

Class	Order	Family	Taxon	Common name
Reptilia	Squamata	Varanidae	<i>Varanus</i>	Monitor lizard
Aves			Aves gen. et sp. indet. (small)	Small bird
			Aves gen et sp. indet (medium)	Medium bird
	Struthioniformes	Struthionidae	<i>Struthio</i> sp.	Ostrich
Mammalia	Primates	Hominidae	<i>Homo sapiens</i>	Human
	Rodentia		Myomorpha gen. et sp. indet.	Rodent
Artiodactyla	Hippopotamidae		<i>Hippopotamus</i> sp.	Hippopotamus
		Bovidae	cf. <i>Pelorovis</i>	Pelorovis
			cf. <i>Kobus</i> sp.	Kobus
			Large bovid gen. et sp. indet.	Large bovid
			Medium bovid gen. et sp. indet.	Medium bovid
			Small bovid gen. et sp. indet.	Small bovid

1772

1773

1774

1775

1776

1777

1778

1779

1780

1781

1782

1783 **Supplementary Table 20. Number of Identified Specimens for small, medium and large-**
 1784 **sized fossil vertebrates from Al Wusta.**

1785

Element	Small	Medium	Large
Horn core	2	1	-
Crania	2	-	-
Mandible	2	4	-
Isolated teeth	5	10	2
Vertebrate	2	7	4
Ribs	7	12	4
Scapula	-	1	-
Pelvis	-	2	1
Humerus	2	3	2
Femur	-	-	-
Radius	-	2	-
Tibia	2	-	-
Carpals/Tarsals	2	4	1
Metapodials	1	-	2
Phalanges	1	2	3
Long bone shaft	11	46	7

1786

1787

1788

1789

1790

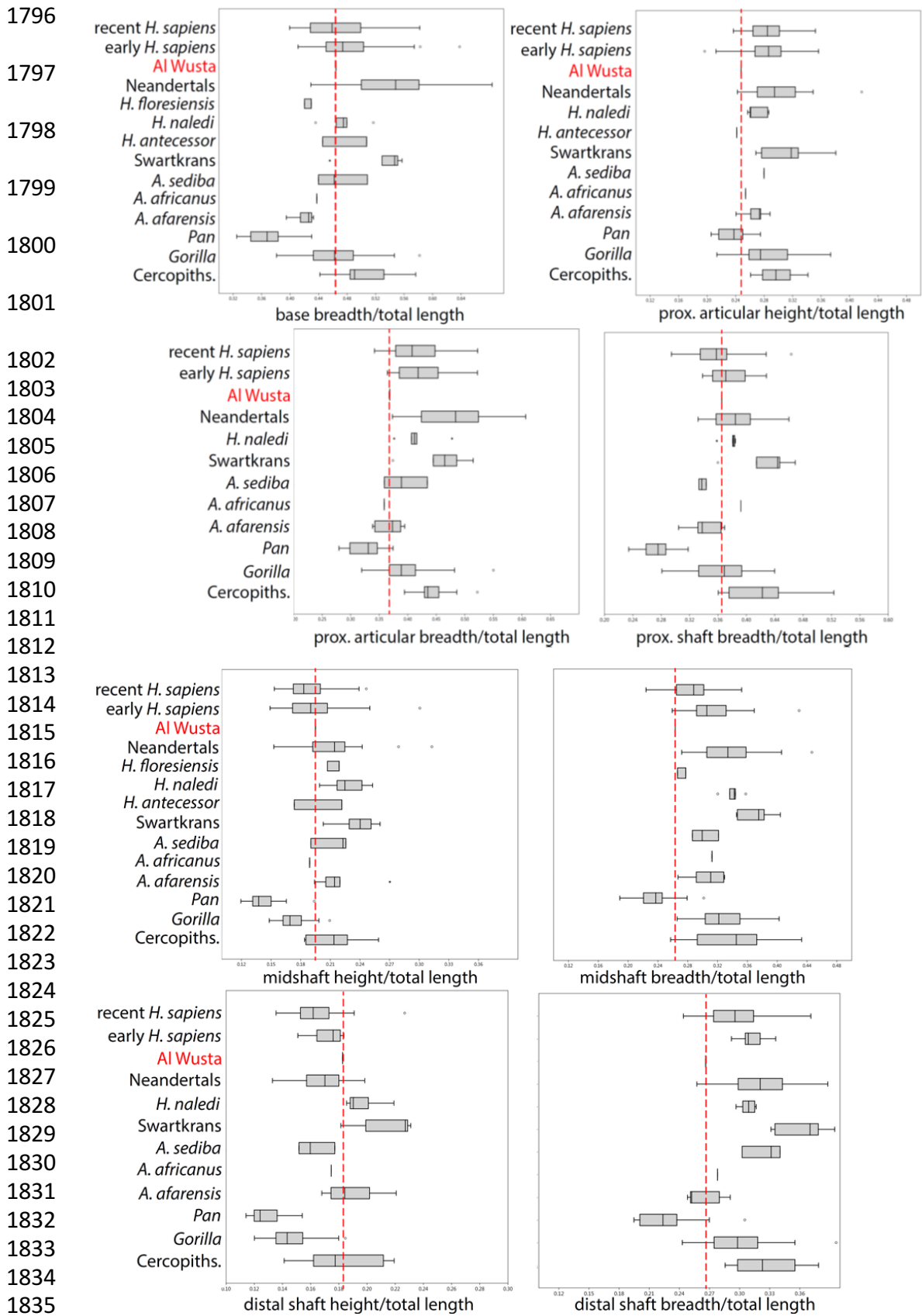
1791 **Supplementary Table 21. Carnivore pit major and minor axes (mm) on fossil bones**
 1792 **from Al Wusta.**

Specimen ID	Major Axis (mm)	Minor Axis (mm)
200	7.7	6.3
94	5.8	4.4
300	3.0	3.0
254	3.2	3.1
288	4.2	3.0
273	6.5	4.5
	3.3	2.7
	4.0	2.9
	1.7	1.7
263	1.7	1.2
291	7.1	3.4
330	4.4	3.4
293	4.5	3.0
309	9.0	6.4
253	9.0	8.0
503	4.0	2.0
516	6.0	6.0
520	1.9	1.6
534	2.2	1.6

1793

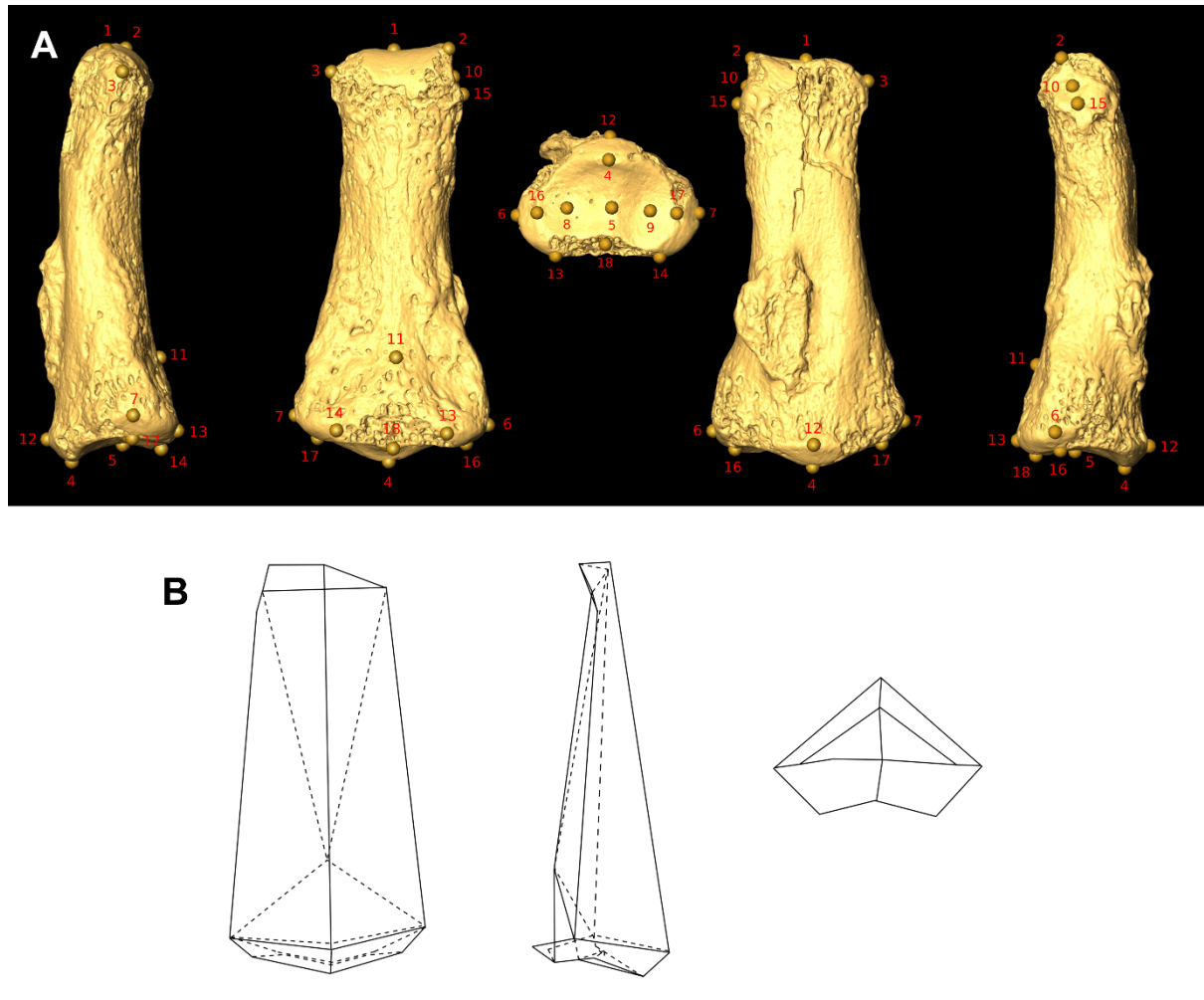
1794

1795



1837 **Supplementary Figure 1. Box-and-whisker plots of intermediate phalanx shape ratios of**
 1838 **AI Wusta 1 and a sample of primates, including hominins. AI Wusta-1 is highlighted in**
 1839 **red.**

1840



1841

1842

1843

1844

Supplementary Figure 2. Landmarks and wireframes used in geomorphometric

1845 **analyses.** A: Landmarks used to analyse phalanx shape using GMM. Landmarks numbered

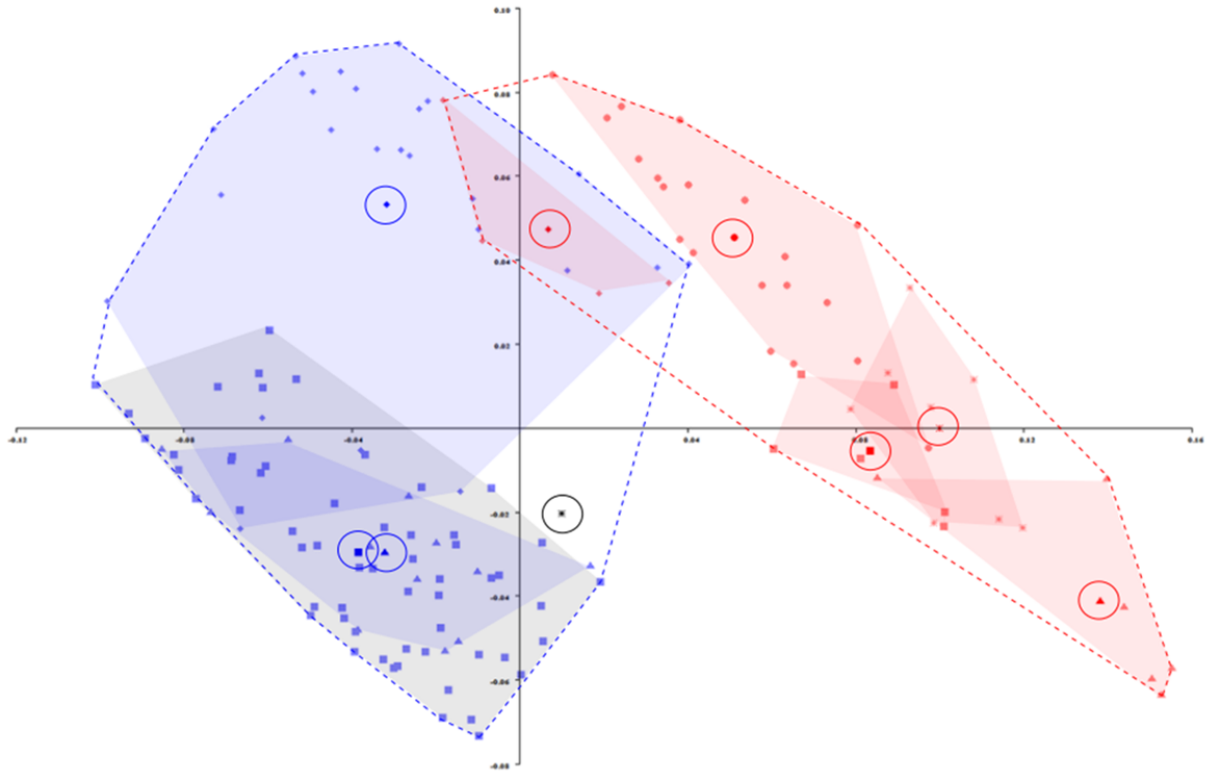
1846 as in Supplementary Table 4 (AW-1 shown); B: Wireframes composed of straight lines

1847 connecting landmarks shown in A. Dorsal (left), lateral (middle) and proximal (right) views.

1848 Dotted lines connect landmarks not visible when bone is present, some lines omitted in

1849 proximal view for ease of visualisation.

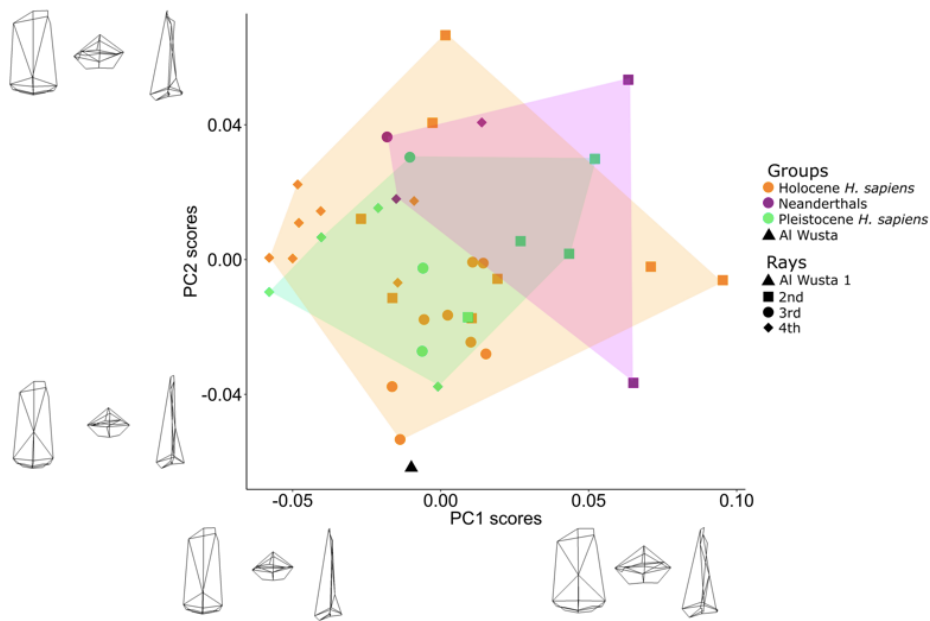
1850



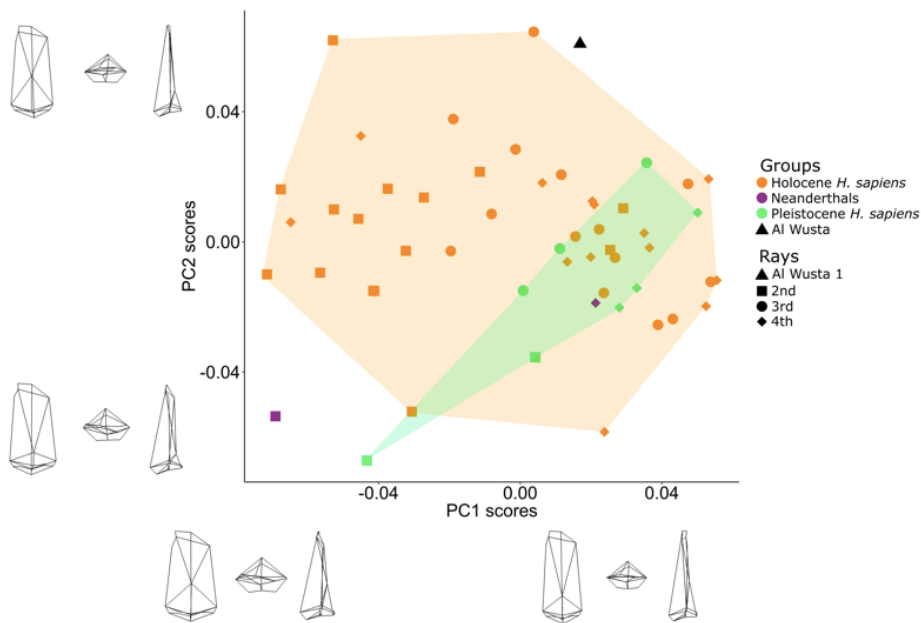
1851
1852

1853 **Supplementary Figure 3. Scatterplot of the first two principal component (PC) scores of**
 1854 **the geometric morphometric analysis of the Al Wusta-1 phalanx and a sample of**
 1855 **primates, including hominins.** Non-human primates in red; *Colobus*: triangles, *Pan*: stars,
 1856 *Mandrillus*: squares, *Gorilla*: circles, *Papio*: diamonds. Hominins in blue; Neanderthals:
 1857 diamonds, Holocene *H. sapiens*: squares, early *H. sapiens*: triangles. AW-1 in black. Data
 1858 presented are the same as Figure 3, but filled convex hulls (for visualisation of data spread
 1859 only) show hominins (blue) and non-human primates (red) generic groups of non-human
 1860 primates and different groups of hominins. Circled shapes show means for groups (see
 1861 Supplementary Table 6).

1862

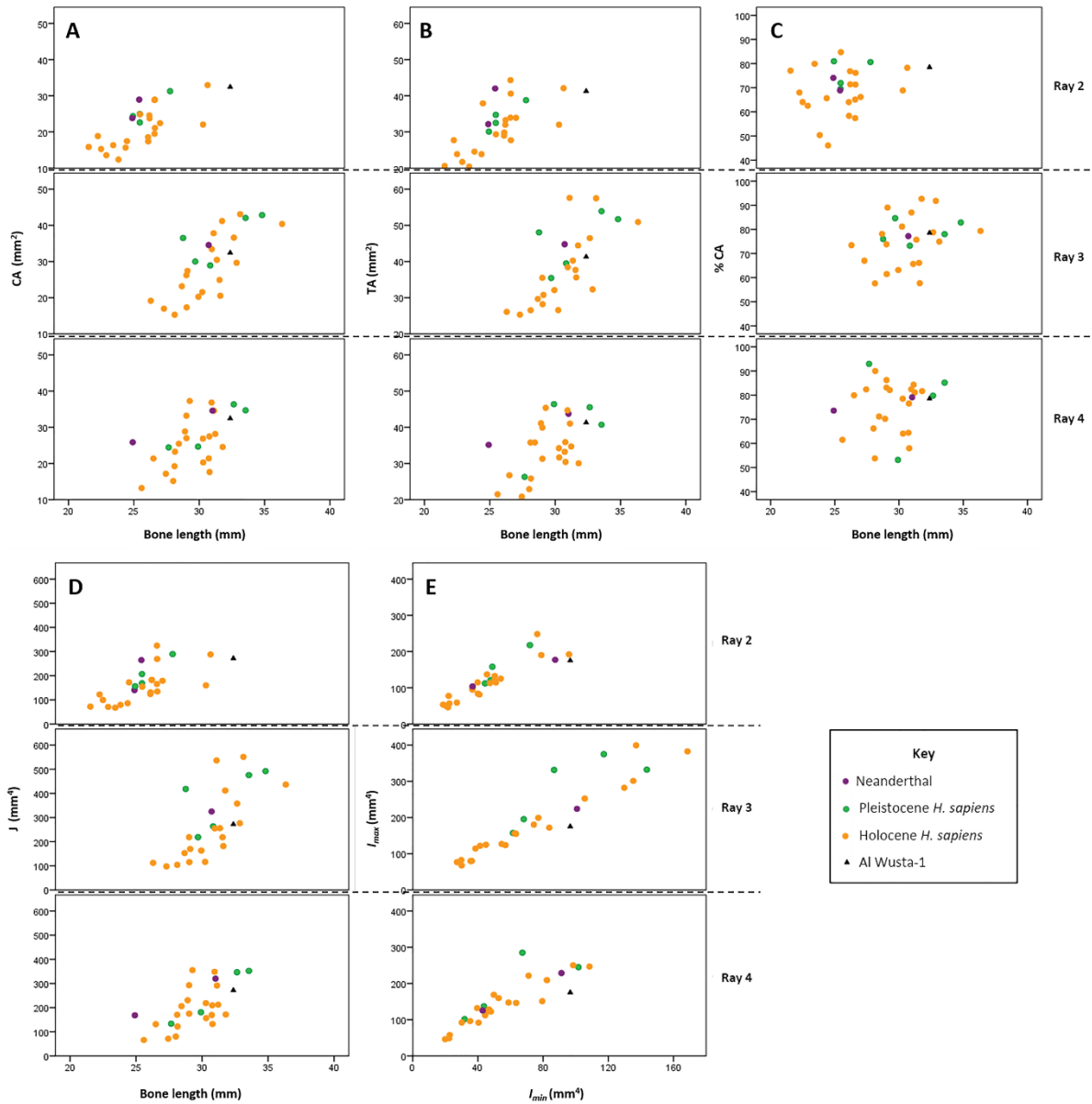


1863



1864

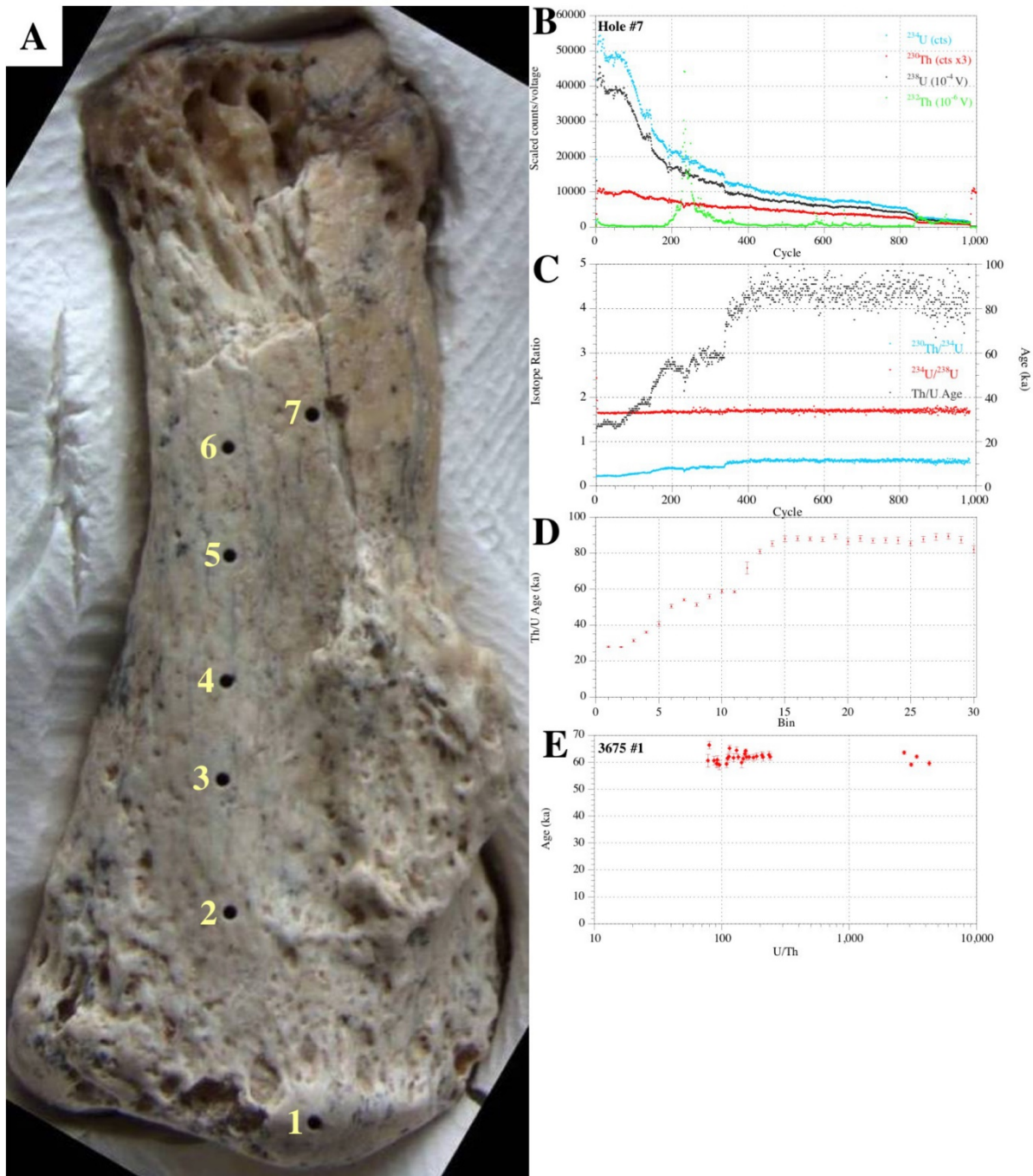
1865 **Supplementary Figure 4. Scatterplots of PC1 and PC2 scores from GMM analyses of**
 1866 **left (top) and right (bottom) intermediate phalanges from a sample of Neanderthals and**
 1867 **modern humans, and Al Wusta-1.** Wireframes (see Supplementary Figure 2) show
 1868 configurations at extremes of PC axes in dorsal (left), proximal (middle) and sagittal (right)
 1869 views. Convex hulls added post-hoc for ease of visualisation.



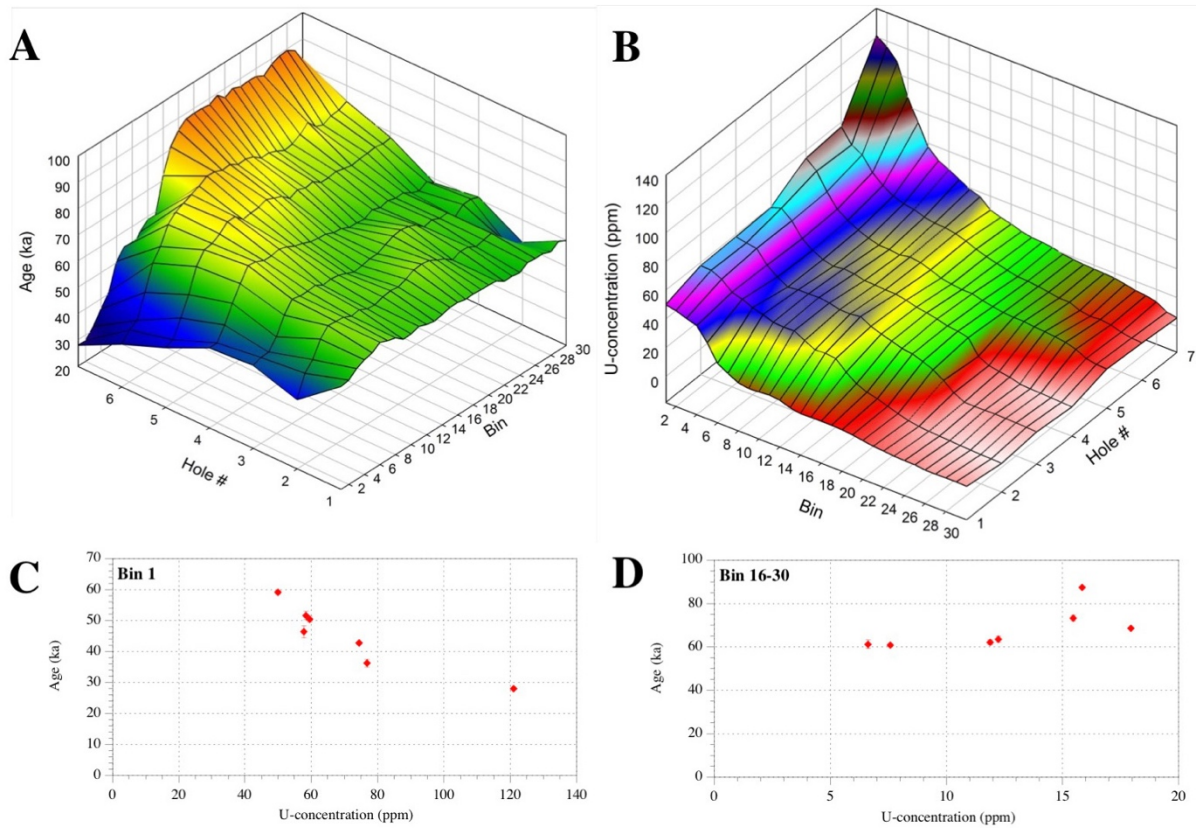
1870
1871

1872 **Supplementary Figure 5. Scatterplots of cross-sectional geometric properties of Al**
 1873 **Wusta-1 and comparative modern human and Neanderthal intermediate manual**
 1874 **phalanges from rays 2-4. Plots against bone length: A = cortical area; B = total area; C =**
 1875 **percent cortical area; D = J . Plot against I_{min} ; E = I_{max} .**

1876

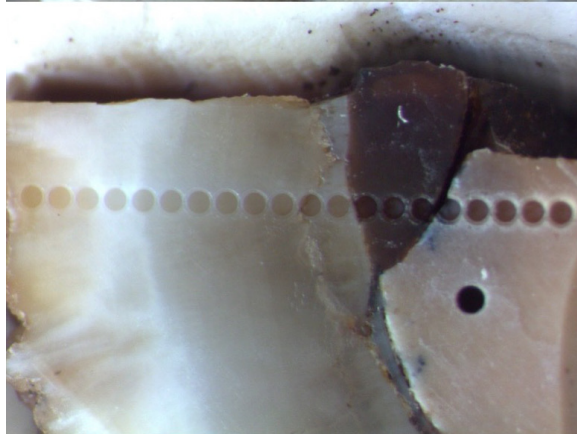
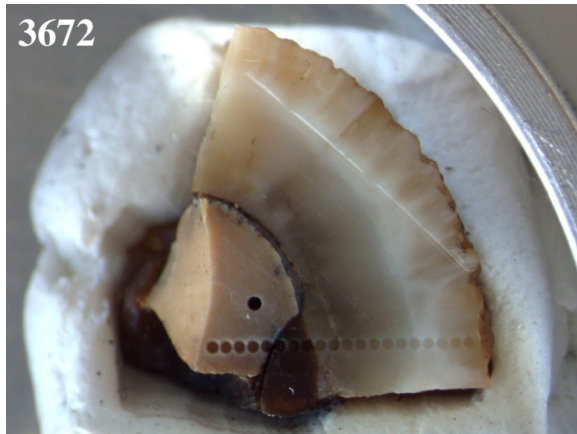


1877
 1878
 1879
 1880
 1881
 1882
 1883
 1884
 1885
 1886
 1887
 1888
 1889



1890
 1891
 1892
 1893
 1894
 1895
 1896
 1897

Supplementary Figure 7. Uranium concentrations and age estimates. A: Plot of all average age estimates; B: U-concentrations (these are not corrected for diminishing U-yields from deeper domains in the hole). Note the different aspect compared to A; C: Age vs U-concentration for outside (bin 1); D: Age vs U-concentration for the age plateaux (bins 16-30).



1898

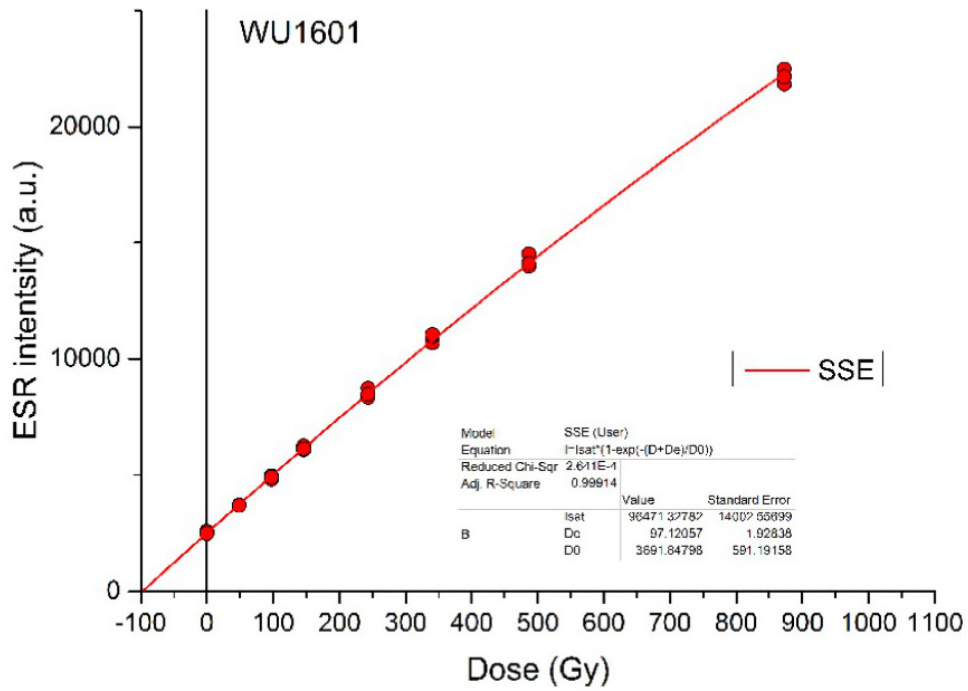
1899 **Supplementary Figure 8. Image of sample WU1601 with location of the laser ablation**
1900 **analysis holes.**

1901

1902

1903

1904



1905

1906 **Supplementary Figure 9. ESR Dose response curve (DRC) obtained for WU1601.** Final

1907 D_E values were calculated for each sample by pooling all the ESR intensities derived from the

1908 three repeated measurements in a single DRC. Fitting was performed with a SSE function

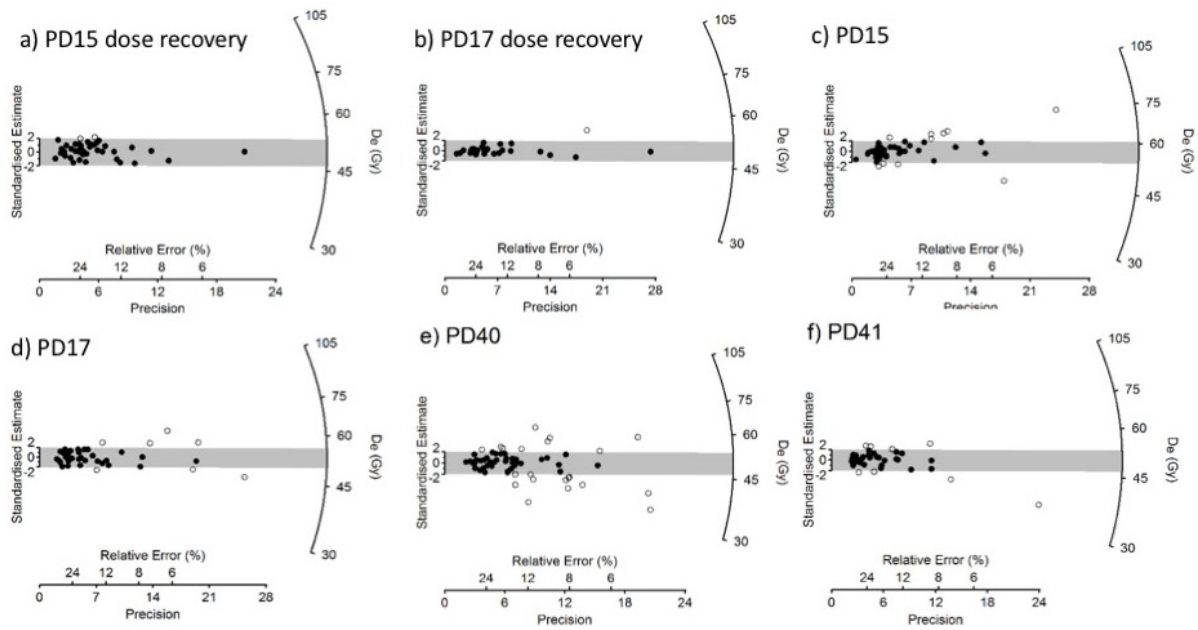
1909 and data weighting by $1/I^2$.

1910

1911

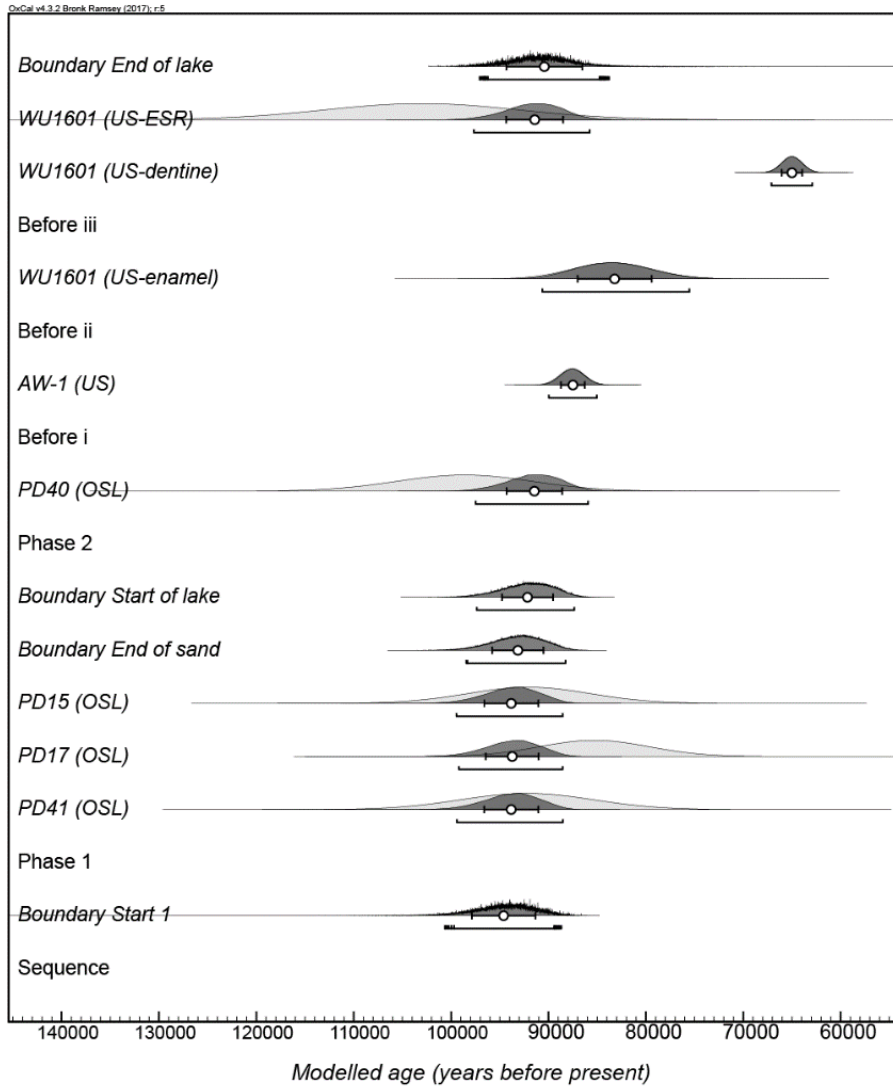
1912

1913



1914
 1915
 1916
 1917
 1918
 1919
 1920
 1921
 1922

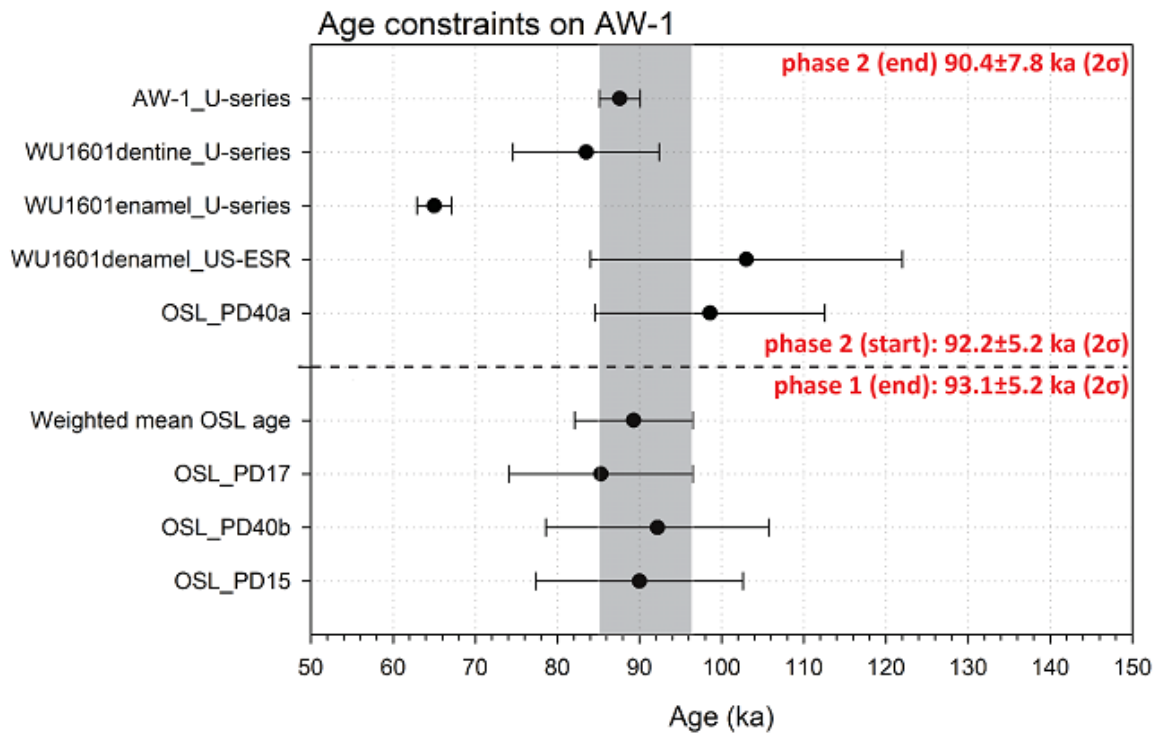
Supplementary Figure 10. OSL radial plots. Radial plots of the single-grain dose distributions for Al Wusta samples. For panels a and b the grey band is centred on the dose administered (49.8 Gy) in the dose recovery experiment. In panels c to f, the grey bar is centered on D_b determined with the Central Age Model. All points that lie within the grey band are consistent (at 2 standard errors) with either the administered dose (a,b) or D_b (c-f), and are shown as closed symbols. Open symbols denote equivalent doses which are greater than 2 standard errors from the administered dose (a,b) or D_b (c-f).



1923
 1924
 1925
 1926
 1927
 1928
 1929
 1930
 1931
 1932
 1933
 1934

Supplementary Figure 11. Modelled ages for stratigraphic Units 1 (aeolian sand underlying the site) and 3 (waterlain sands and associated fossils overlying lacustrine marls). Two sequential phases were defined. Sample codes end with the age determination method in parentheses. The ages WU1601 (US-dentine), WU1601 (US-enamel) and AW-1 (US) are minimum age estimates, and the age model accounts for the fact that U-series ages are conventionally reported with 2 s uncertainties whereas OSL and ESR ages are reported with 1 s uncertainties. *A posteriori* densities are shown in darker shade while the likelihoods are shown in a lighter shade. Open circles underneath the *a posteriori* densities represent the mean age estimate, with 1σ uncertainty bars, while the lower bar represents the 95.4 % range.

1935



1936

1937

1938

Supplementary Figure 12. Overview of the available age constraints for AW-1. In red, the modelled ages of the phase boundaries

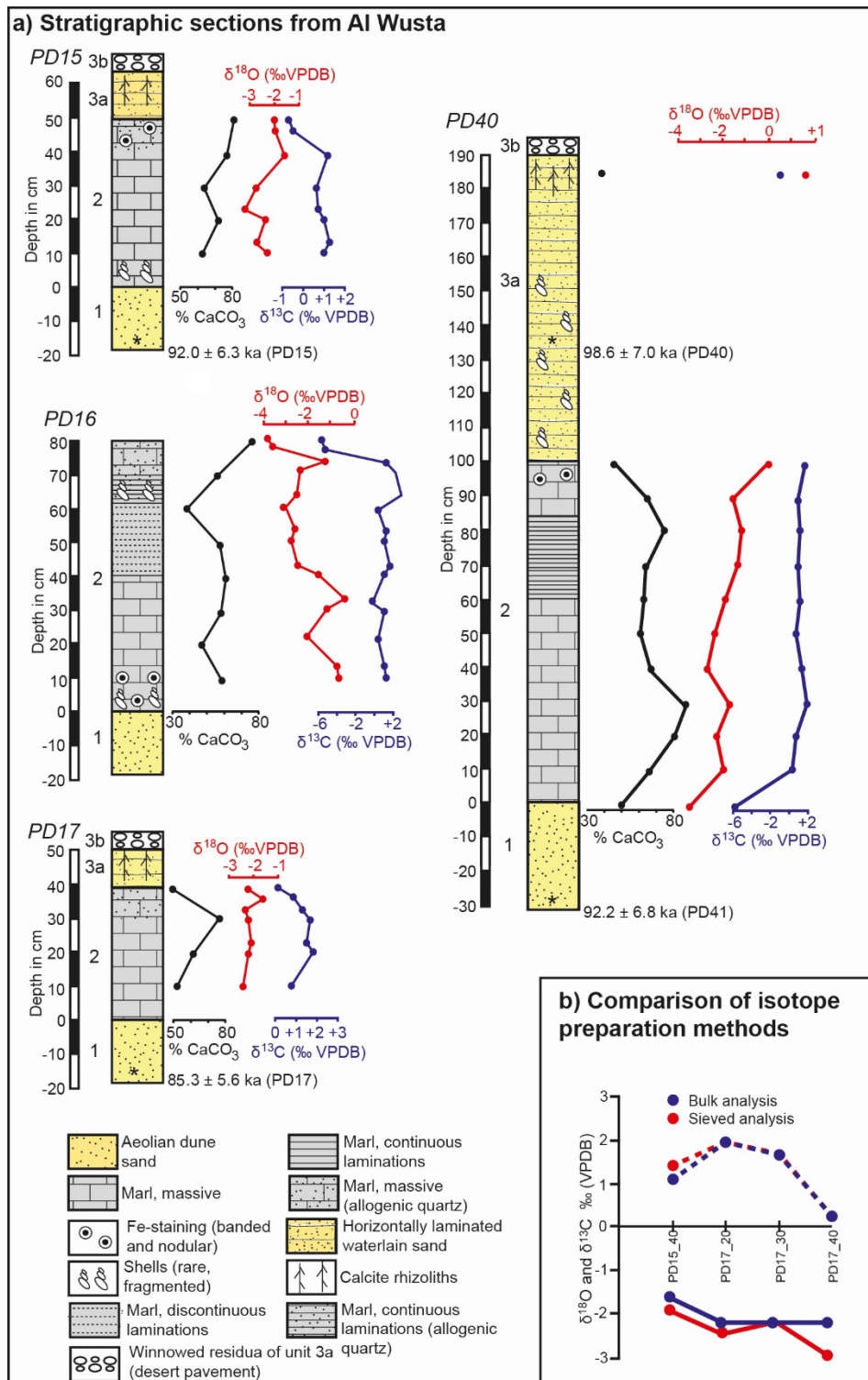
1939

1940

1941

1942

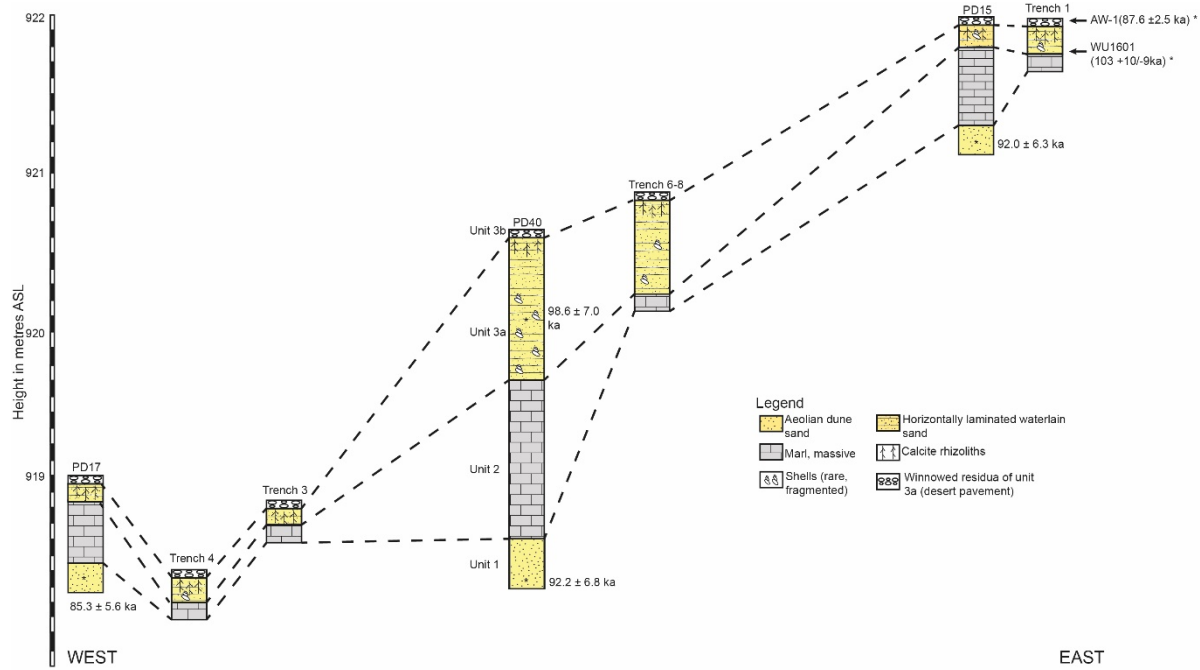
1943



1944
1945
1946
1947
1948
1949
1950
1951
1952
1953

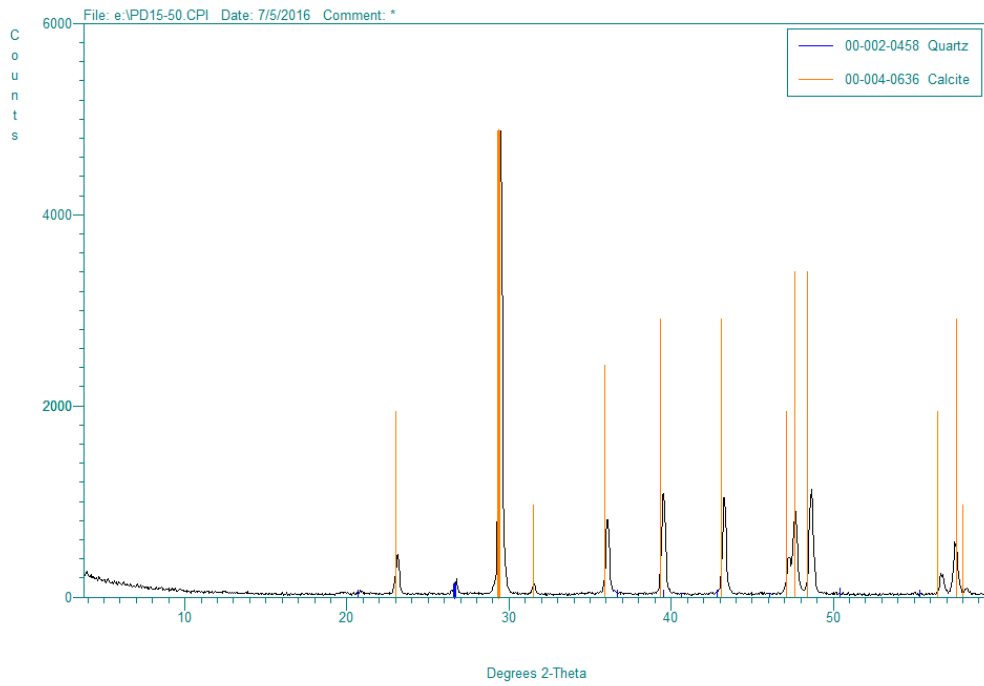
Supplementary Figure 13. Stratigraphic sections from Al Wusta. A: stratigraphic logs of lacustrine marl deposits showing the main sedimentary units and stratigraphic variations in O and C isotopes and % CaCO₃. To avoid wasted space at the base of each stratigraphic section, OSL ages are not presented at their true depth below the sand-marl interface. B: Diagram summarising the difference in isotope values derived from aliquots of the same sample using different preparation techniques (dashed line = carbon isotope values, solid line = oxygen isotope values), although sieving of samples is often desirable the indurated nature of many samples makes such an approach impractical.

1954
1955
1956

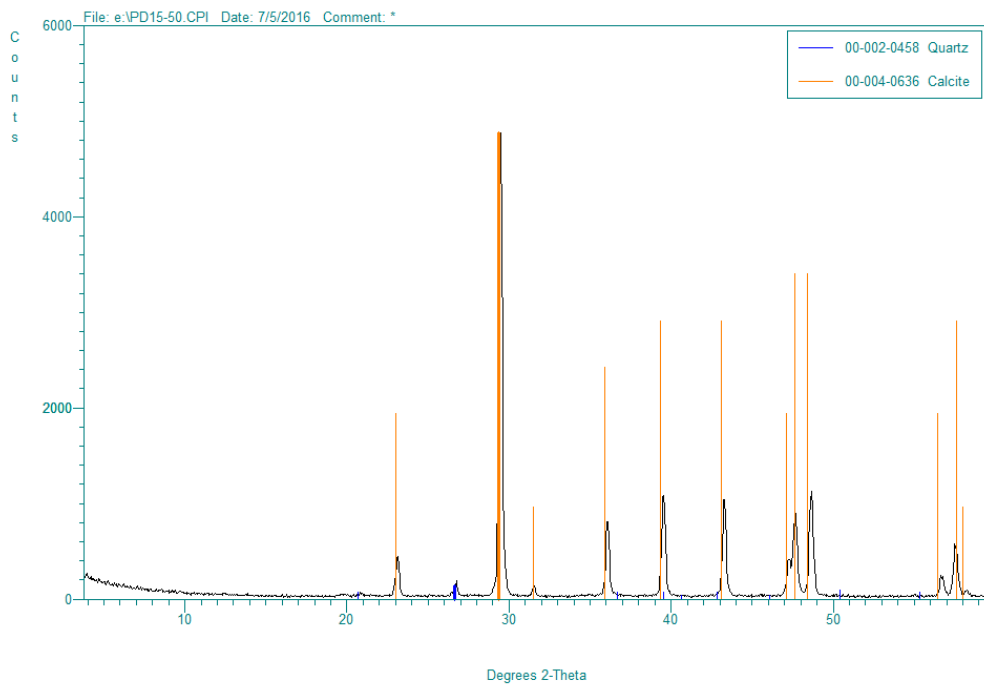


1957
1958
1959
1960

Supplementary Figure 14. Composite stratigraphic diagram showing the relationship between different sections across the site.



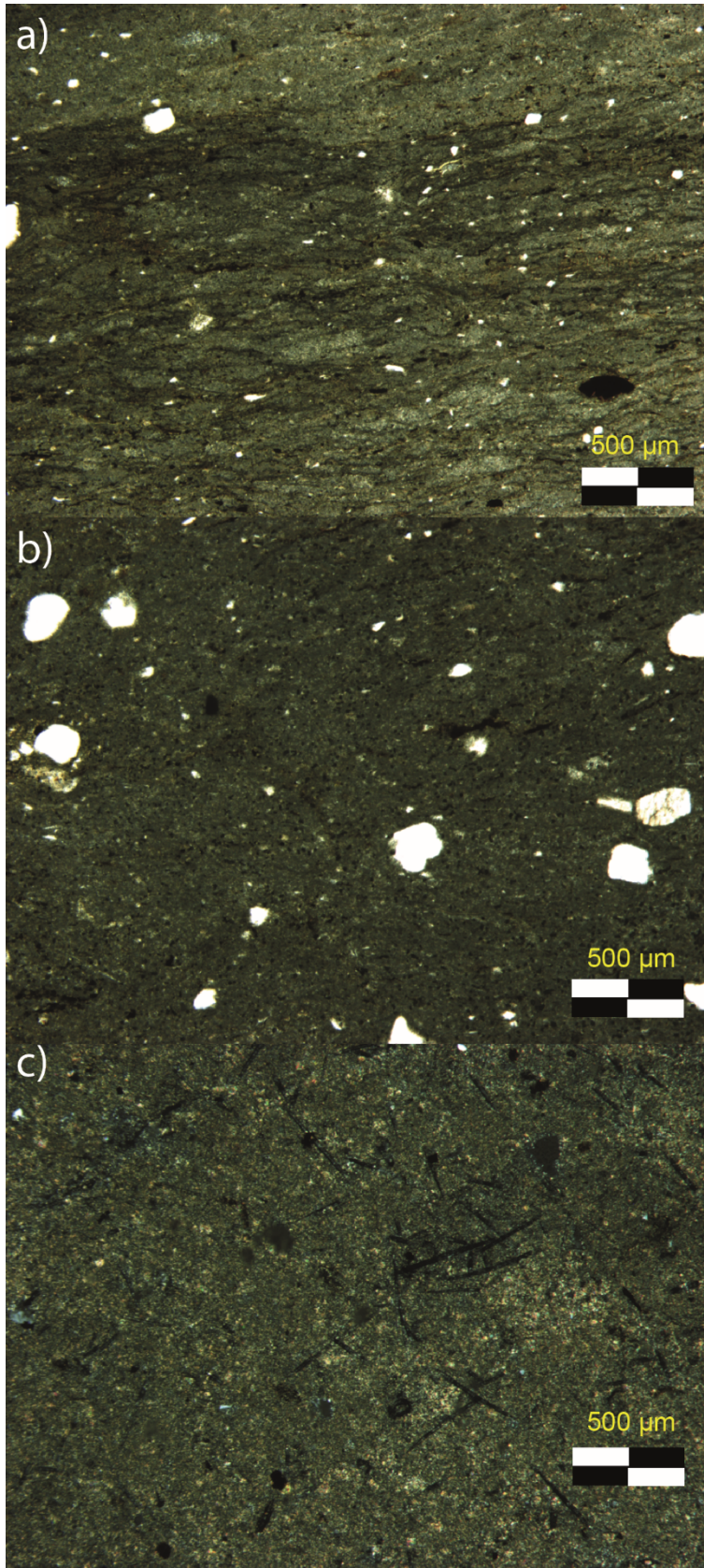
1961



1962

1963 **Supplementary Figure 15. XRD traces from PD15-50 (top) and PD17-40 (bottom).**

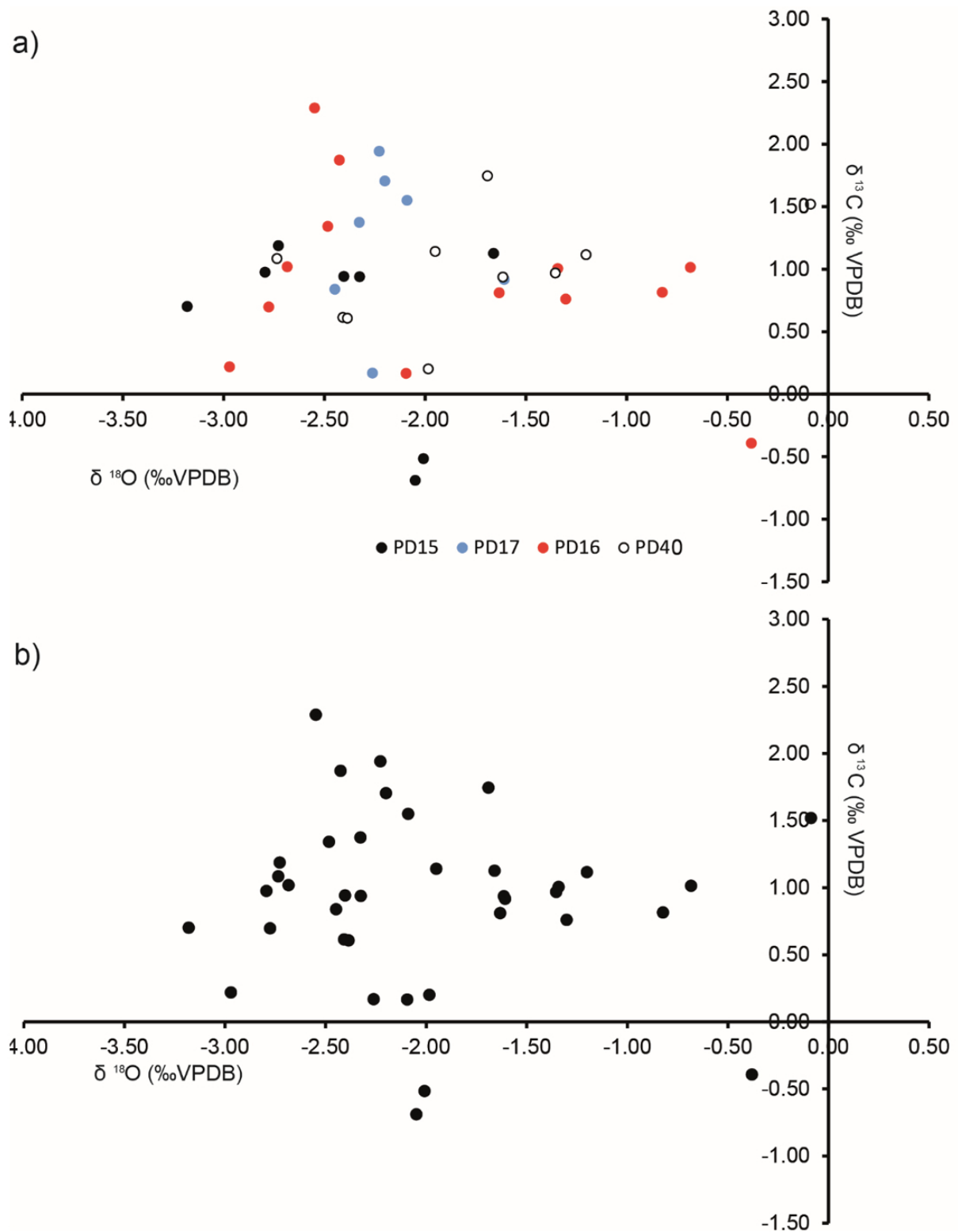
1964 Calcite peaks (orange) dominate with secondary quartz peaks (blue).



1965

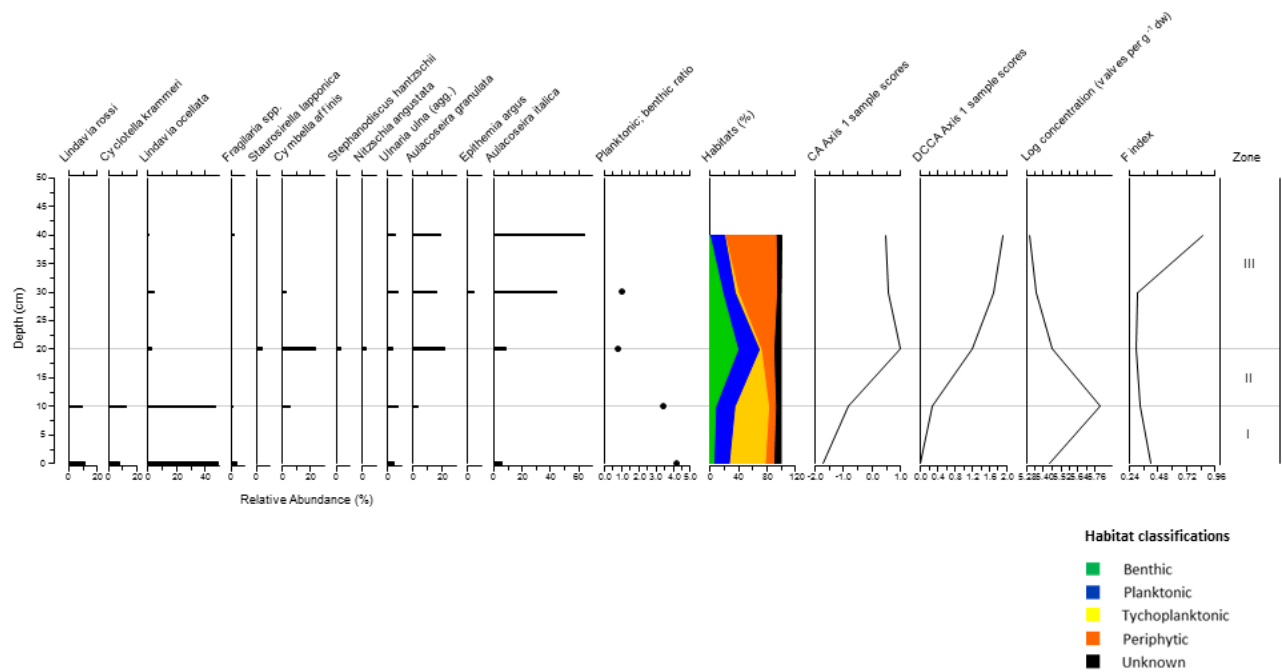
1966 **Supplementary Figure 16. Representative photo-micrographs of Al Wusta lake**
1967 **sediments.** A) Finely laminated microsparite with silt-sized quartz grains (Allogenic). B)
1968 Massive microsparite with sand sized quartz grains (allogenic). C) freshwater sponge spicules
1969 in a microsparite/sparite massive matrix.

1970
1971



1972

1973 **Supplementary Figure 17. Al Wusta carbonate isotopic data shown by sampling**
1974 **location (a) and as a single dataset (b).** The overall r^2 value is 0.0521, while for each site
1975 the value is PD15 = 0.121, PD17 = 0.001, PD16 = 0.132, PD40 = 0.072. The three outlying
1976 samples are not shown but are included in the r^2 calculation.



1977

1978 **Supplementary Figure 18. Summary diagram of Al Wusta Pit 1 PD 15 diatomite diatom**

1979 **assemblage.** All taxa with relative abundances of $\geq 3\%$. The diatoms are ordered according to

1980 their weighted averaging distribution and divided up into assemblage zones derived from the

1981 optimal-sum-of squares partitioning using the program ZONE⁵². The statistically significant

1982 zones were deduced by comparison with the Broken-stick model using the program BSTICK

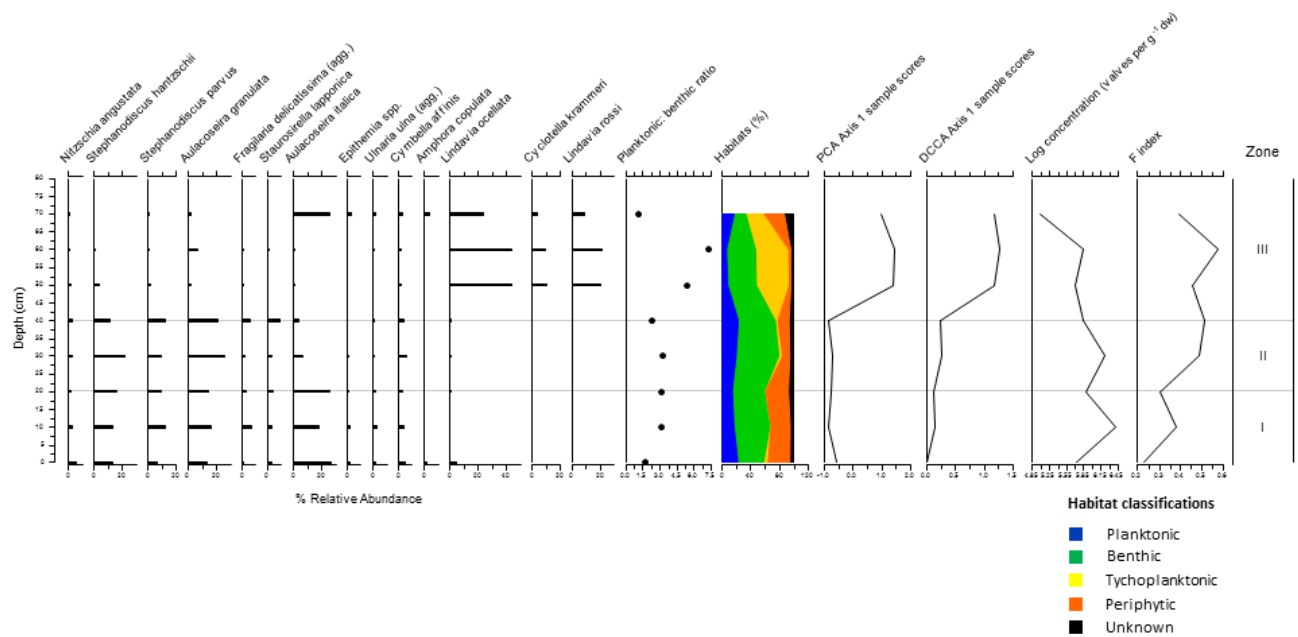
1983 version 1⁵². The planktonic: benthic ratio is shown with the habitat summary, Correspondence

1984 Analysis and Detrended Canonical Correspondence Analyses axis 1 sample scores

1985 (abbreviated to CA and DCCA respectively), log concentration, F-index which ranges from 0

1986 (most dissolved) to 1 (most pristine).

1987



1988

1989 **Supplementary Figure 19. Summary diagram of Al Wusta Pit 2 PD 16 diatomite diatom**

1990 **assemblage.** All taxa with relative abundances of $\geq 3\%$. The diatoms are ordered according to

1991 their weighted averaging distribution and divided up into assemblages zones derived from the

1992 optimal-sum-of squares partitioning using the program ZONE⁵². The statistically significant

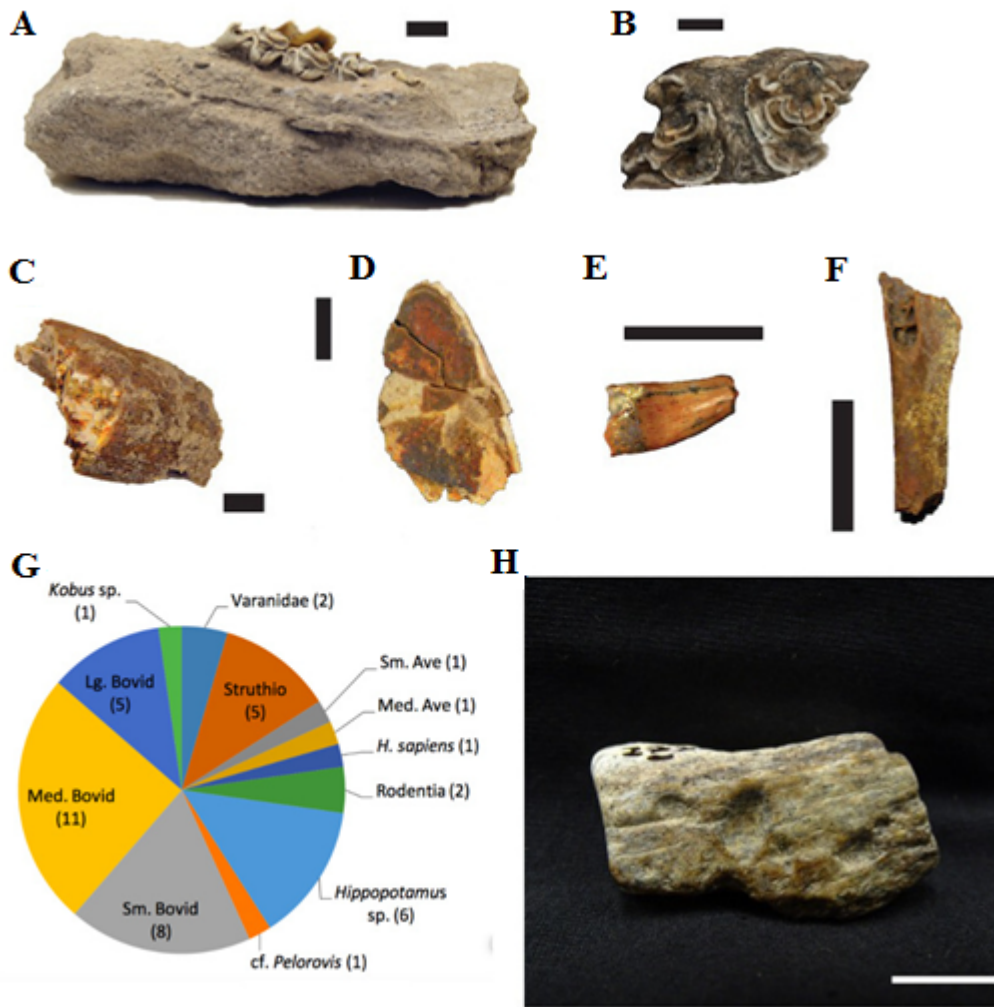
1993 zones were deduced by comparison with the Broken-stick model using the program BSTICK

1994 version 1⁵². The planktonic: benthic ratio is shown with the habitat summary, Principal

1995 Component Analysis and Detrended Canonical Correspondence Analyses axis 1 sample

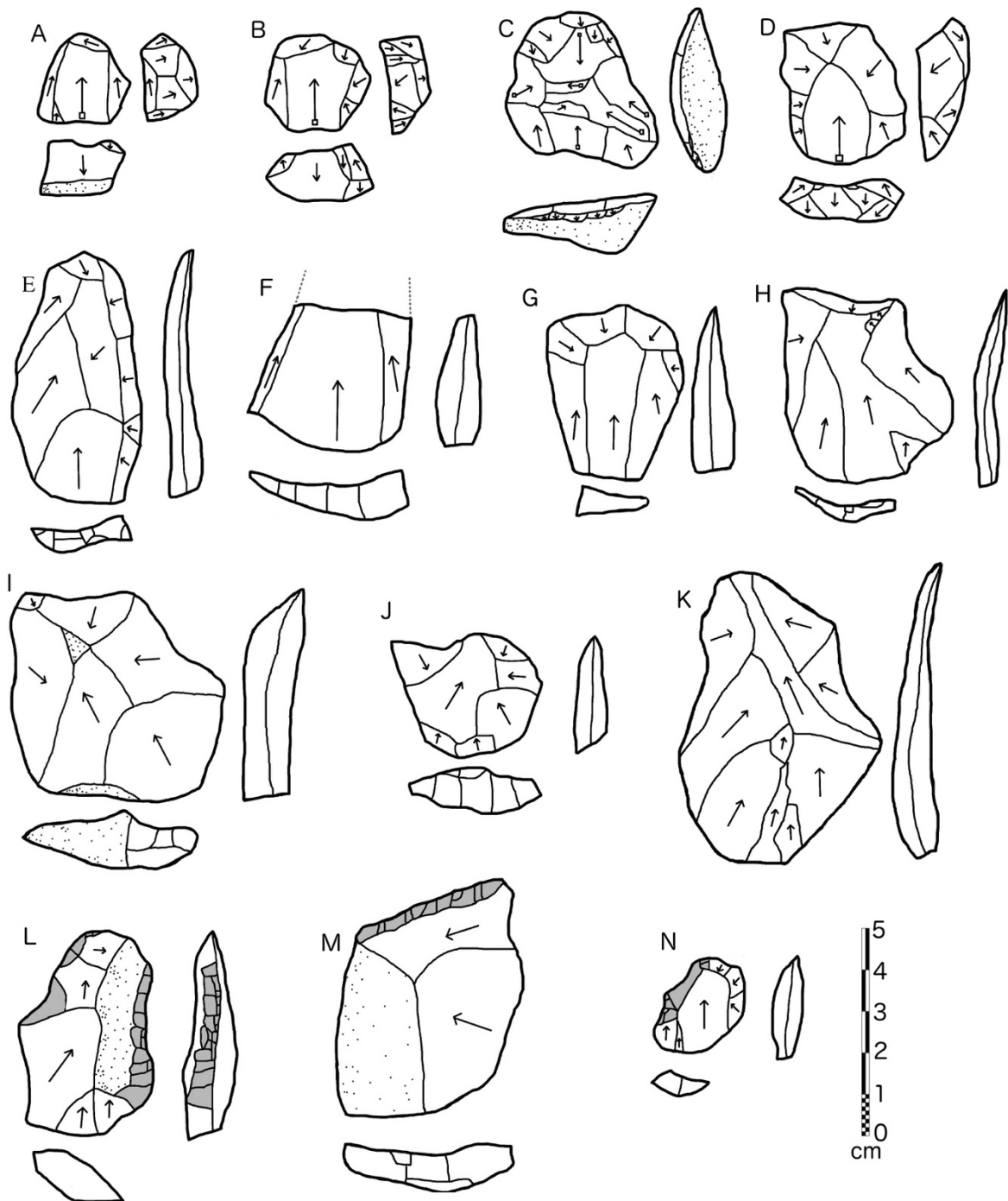
1996 scores (abbreviated to PCA and DCCA respectively), log concentration, F-index which

1997 ranges from 0 (most dissolved) to 1 (most pristine).



1998
 1999
 2000
 2001
 2002
 2003
 2004
 2005
 2006
 2007
 2008
 2009
 2010
 2011
 2012
 2013
 2014
 2015
 2016
 2017
 2018
 2019
 2020

Supplementary Figure 20. Al Wusta vertebrate palaeontology. A: cf. *Kobus* sp. lower right M2-3; B: *Pelorovis* sp. mandibular fragment; C: *Hippopotamus* sp. ?upper canine fragment; D: *Hippopotamus* sp. medial upper incisor; E: *Varanus* sp. isolated tooth; F: Aves gen. et sp. indet. coracoid fragment; G: NISP for identified taxa. NISP is reported in parentheses; H: Evidence of carnivore gnawing on a bone fragment. Black scale bar = 10mm. White scale bar = 15mm.



2021
 2022
 2023
 2024
 2025
 2026
 2027

Supplementary Figure 21. Selected Al Wusta lithic artefacts. A,B,D: Preferential Levallois cores with centripetal preparation, C: recurrent centripetal Levallois core, E,G-K: Levallois flakes, F: broken Levallois point, L: double side retouched flake, M: end retouched flake, N: side retouched flake.

2028

2029